

Development of a
Joule-class Yb:YAG amplifier
and its implementation in a
CPA system generating 1 TW pulses

Christoph Wandt

Dissertation
an der Fakultät für Physik
der Ludwig-Maximilians-Universität
München

vorgelegt von

Christoph Wandt
aus Erfurt

München, den 22.5.2014

Erstgutachter: Prof. Dr. Stefan Karsch
Zweitgutachter: Prof. Dr. Ulrich Schramm
Tag der mündlichen Prüfung: 9.7.2014

ZUSAMMENFASSUNG

Die optische parametrische Verstärkung von zeitlich gestreckten Laserpulsen (OPCPA) [1] ist die Methode der Wahl, um die Energie ultrakurzer Laserpulse zu erhöhen. In Kombination mit modernen CPA-Systemen [2] als Pumplaser lassen sich so Pulsdauern von wenigen Femtosekunden mit Pulsenergien im Joule-Bereich erzeugen. Solche OPCPA-Systeme sind die Voraussetzung um neue physikalische Phänomene, wie z.B die Erzeugung von einzelnen Attosekundenpulsen auf Festkörperoberflächen [3, 4] oder die Elektronenbeschleunigung in lasergenerierten Plasmen [5, 6], untersuchen zu können. Heutzutage lassen sich in vergleichbaren OPCPA-Systemen bereits Pulsspitzenleistungen von einigen Terawatt [7] erzeugen.

Das Max-Planck-Institut für Quantenoptik (MPQ) in Garching entwickelt mit dem Petawatt Field Synthesizer (PFS) [8] ein solches, neuartiges OPCPA-System. Ziel des PFS-Projektes ist es, erstmalig Pulse mit einer Energie von 5 J bei einer Pulsdauer von 5 fs zu erzeugen. Dazu benötigt man einerseits extrem breitbandige (700 - 1400 nm) Eingangspulse und andererseits einen ultra-intensiven, hoch-energetischen Pumplaser. Zur Realisierung des PFS-Projektes wird ein CPA-Pumplaser benötigt, der 4x12.5 J Pulsenergie bei einer Pulsdauer von 1 ps liefert. Da ein solches System nicht kommerziell erhältlich ist, muß es am MPQ selbst entwickelt werden.

Die vorliegende Dissertation wurden im Rahmen der Entwicklung und des Aufbaus eines solchen Pumplasers, basierend auf CPA in dioden-gepumpten, Yb-dotierten Materialien, erstellt. In Zusammenarbeit mit *S.Klingebliel* wurden der Strecker- und Kompressor Aufbau und erste Verstärkerstufen implementiert [9]. Zu Beginn der Doktorarbeit wurde ein 8-Pass Yb:YAG Verstärker entwickelt, durch den die Pulsenergie der gestreckten 4ns-Pulse auf 300 mJ, bei einer Wiederholfrequenz von 10 Hz, verstärkt werden konnte. Die dabei erreichte spektrale Bandbreite von 3.8 nm erlaubte es, die Pulse auf <1 ps zu komprimieren [10]. Zum damaligen Zeitpunkt waren dies einzigartige Resultate für die Verstärkung in Yb:YAG. Allerdings konnte aufgrund der starken thermischen Linse im Laserkristall diese Verstärkerarchitektur nicht für die zusätzlich benötigten Verstärkerstufen übernommen werden.

Hauptziel dieser Arbeit war es also, eine neue Verstärkerarchitektur zur Erzeugung von ≥ 1 J-Pulsen zu entwickeln und aufzubauen. Dabei sollte die thermische Belastung der Yb:YAG Kristalle durch die Verwendung des "active-mirror"-Konzepts [11] reduziert und die Extraktionseffizienz sowie das Strahlprofil durch einen abbildenden Aufbau optimiert werden. Mit Hilfe von CAD- und Ray-Tracing-Programmen wurde ein solcher abbildender 20-Pass Verstärker Aufbau realisiert. Desweiteren war es nötig, eine eigene Methode zum Aufkleben der Laserkristalle auf Wärmesenken zu entwickeln, da keine kommerzielle Lösung existierte.

In einer ersten Messkampagne wurden verschiedene Yb:YAG Kristalle, welche sich in Dotierung, Dicke und Größe unterscheiden, hinsichtlich ihrer Verstärkung bei geringen Eingangsenergien untersucht. Es wurde festgestellt, dass unter Berücksichtigung der gewählten Pumpparameter, ab einer Dotierung von 2% parasitäre Effekte die Verstärkung drastisch reduzieren. Da die Verstärkung im 2%-dotierten, 6mm x 40x40mm² großen Yb:YAG Kristall am höchsten war und Pulsenergien ≥ 1 J erlaubte wurde dieser Kristall für die zweite Messkampagne ausgewählt. Dabei konnten durch die schrittweise Erhöhung der Eingangsenergie Ausgangsenergien von 1 J, bei 1 Hz und bei 2 Hz Wiederholrate, erzeugt werden. Desweiteren wurde nahezu die gesamte spektrale Bandbreite während der Verstärkung beibehalten und die Pulse schlußendlich auf ihr *Fourier*-Limit von 740 fs komprimiert. Unter Berücksichtigung der zeitlichen Pulsstruktur und der Kompressorverluste ergibt sich somit eine erzeugte Pulsspitzenleistung von 1 TW.

Nach unserem Wissensstand wurden solche Parameter bisher noch nicht in der Literatur beschrieben und wir sind somit die Ersten, die 1 TW Pulse in einem Yb:YAG CPA-System erzeugt haben.

ABSTRACT

Optical parametric chirped pulse amplification (OPCPA) [1] is a promising technique for amplifying few-cycle laser pulses. By utilizing high-energy pump pulses provided by laser systems based on chirped pulse amplification (CPA) [2], OPCPA systems are able to deliver Joule-level pulse energies with few-femtosecond pulse durations. Such light sources are a prerequisite for exploring physics driven by single attosecond extreme ultraviolet (XUV) pulses generated via surface harmonics [3, 4] and for studying plasma physics and electron acceleration at ultrafast time scales [5, 6]. So far, peak powers in the TW-range have been demonstrated [7].

The Max-Planck-Institute of Quantum Optics (MPQ) is pursuing OPCPA with the development of the Petawatt Field Synthesizer (PFS) [8]. The final parameters of the PFS are a pulse energy of 5 J at a pulse duration of 5 fs. To achieve these goals one needs, on the one hand, a nearly octave-spanning seed spectrum and amplification bandwidth, in our case ranging from 700nm-1400 nm and on the other hand, a state-of-the-art ultra-intense, high-energy pump laser which has to deliver an initial pump energy of 4×12.5 J at a pulse duration of 1 ps. Such a system is not commercially available and therefore has to be developed at the MPQ in its own right.

The present dissertation was performed in the framework of the development and implementation of such a pump source which will be based on CPA in diode-pumped Yb-doped materials. The work includes the implementation of a stretcher-compressor setup and first amplification stages. Both parts were done in close collaboration with *S.Klingebiel* [9]. At the beginning of this thesis work, an Yb:YAG 8-pass amplifier was built, increasing the energy of the stretched 4ns-pulses to 300 mJ at 10 Hz repetition rate while maintaining a spectral bandwidth of 3.8 nm. Furthermore, compression to pulse durations < 1 ps was shown [10]. At that time, these were unmatched parameters for a Yb:YAG CPA system. However, this main amplifier proved to be a one-off prototype due to the strong thermal lensing in the Yb:YAG crystal and thus this scheme could not serve as a model for upscaling.

Thus, the main goal of this thesis is the implementation of a new multi-pass amplifier scheme to generate a pulse energy ≥ 1 J. The scheme features an Yb:YAG active-mirror architecture [11] to reduce the thermal load of the crystals and a relay-imaging configuration to improve the extraction efficiency and the beam profile. By utilizing optical design software a 20-pass relay-imaging amplifier was designed and set up. Furthermore, since no commercial solution was available, a own glueing process for bonding large crystals to special heat sinks was developed.

The finished amplifier was subjected to a number of trial campaigns in order to map its performance envelope. In the "low-energy" measurement campaign, several Yb:YAG crystals differing in doping concentration, thickness and size were analysed according to their amplification performance at different heat sink temperatures and repetition rates. It was found that parasitic effects strongly decrease the overall gain if the doping concentration exceeds 2% in the given pump geometry. Since the gain in the 2%-doped $6\text{mm} \times 40 \times 40\text{mm}^2$ Yb:YAG crystal was the highest, allowing to finally reach pulse energies ≥ 1 J, this crystal it was chosen for the the "high-energy" measurement campaign where the seed energy was increased stepwise. 1 J pulses with a pulse-to-pulse stability of $\sigma \leq 1.5\%$ were generated at 1 Hz and 2 Hz repetition rate. Furthermore, the full spectral bandwidth was maintained during amplification and the compression to a *Fourier*-limited pulse duration of 740 fs was realized. Under consideration of the pulse shape and the compressor losses, the peak power of the pulse is calculated to 1 TW.

To the best of our knowledge, comparable pulse parameters are not reported in the literature so far and thus we showed for the first time the generation of 1 TW pulses in a diode-pumped Yb:YAG CPA-system.

CONTENTS

1	Introduction	1
1.1	Motivation	1
1.2	Thesis outline	3
i	Theory	5
2	Laser pulse amplification	7
2.1	The general idea of the laser	7
2.2	Multiple-level systems	9
2.3	Creation of a population inversion	10
2.4	Laser pulse amplification	11
2.5	Amplified spontaneous emission	12
2.6	Summary	14
3	Gain material	15
3.1	General considerations	15
3.2	Yb-doped laser materials	16
3.3	Spectroscopic properties of Yb:YAG	19
3.4	Summary	21
4	Chirped pulse amplification	23
4.1	Generation and description of ultrashort optical pulses	23
4.1.1	Generation of ultrashort optical pulses	23
4.1.2	Description of ultrashort optical pulses	24
4.2	Sources of dispersion	25
4.2.1	Dispersion introduced by a transparent medium	25
4.2.2	Dispersion introduced by grating arrangements	26
ii	Modelling	27
5	Modelling laser pulse amplification	29
5.1	Description of the model	29
5.2	Selected simulation topics	30
5.2.1	Multi-pass pumping	30
5.2.2	Gain narrowing	31
5.2.3	Case study of a >1J-amplifier	32
5.3	Discussion of the model	34
iii	The PFS pump laser	35
6	The PFS pump laser	37
6.1	Frontend and pre-amplifiers	38
6.2	The stretcher	39
6.3	The regenerative amplifier	40
6.4	The 8-pass booster amplifier	41
6.5	The grating compressor	43
6.6	Summarized key parameters	44
iv	Concept of the 1 J-amplifier	45
7	Concept of the 1 J-amplifier	47
7.1	Pump module for the 1 J-amplifier	47
7.2	Active-mirror Yb:YAG crystal assemblies	49
7.3	Relay-imaging multi-pass amplifier setup	53
7.3.1	Relay-imaging amplifier concepts	53
7.3.2	Ray-tracing analysis of the 3D 20-pass relay-imaging amplifier	58
7.3.3	Mechanical design of the 20-pass relay-imaging amplifier	60

v	Experiments	63
8	Low-energy experiments	65
8.1	Input parameters of the "low-energy" campaign	65
8.2	Regression analysis procedure	66
8.3	Amplification performance	68
8.3.1	2% \times 6 \times 20 Au1 vs. 2% \times 6 \times 40 Au1	69
8.3.2	6% \times 3 \times 20 Au1 vs. 6% \times 3 \times 20 Ni 2	70
8.3.3	8% \times 2 \times 20 Au1 vs. 8% \times 2 \times 20 Ni 3	71
8.4	Comparison of the amplification performance	72
8.5	Comparison of the output beam profiles and wavefronts	74
8.6	Conclusions of the "low-energy" campaign	76
9	High-energy experiments	77
9.1	Preparatory measurements for the high-energy campaign	77
9.2	High-energy amplification performance	79
9.2.1	Amplified pulse energy and spectra	79
9.2.2	Compression and FROG-evaluation of the amplified pulses	80
9.2.3	Amplified beam profile and wavefront	81
9.3	Summary of the "high-energy" campaign	82
vi	Future amplifiers	83
10	Concept for a ≥ 10 J-amplifier	85
10.1	Pump modules for the 10 J-amplifier	85
10.2	Amplifier design for a 10 J-stage	87
10.3	Yb:YAG design considerations	88
10.3.1	Single-disk design	89
10.3.2	Double-disk design	90
10.3.3	Multi-slab design	91
vii	Summary and Outlook	93
11	Summary & Outlook	95
11.1	Summary	95
11.2	Outlook	97
viii	Appendix	99
a	Verification of the constant M_{ASE} approach	101
	Bibliography	103
	Publications by the author	111
	Acknowledgements	113
	Data archiving	115
	Colophon	117

LIST OF FIGURES

Figure 2.1	Scheme of 2-level system and the possible transitions	7
Figure 2.2	Scheme of a three-level and a four-level system	9
Figure 2.3	Impact of M_{ASE} and pump intensity on the upper-state population	13
Figure 2.4	Critical product of doping concentration and pump spot diameter	14
Figure 3.1	Comparison of different laser materials regarding energy storage and extraction plus their ability of short pulse generation	16
Figure 3.2	Absorption cross sections of different Yb-doped materials	17
Figure 3.3	Thermal shock parameter R_S in dependence of the thermal conductivity k for different laser materials	17
Figure 3.4	Absorption and emission cross section of Yb:YAG for different temperatures	19
Figure 3.5	Contour plots of the absorption and emission cross sections of Yb:YAG for different temperatures	20
Figure 3.6	Peak absorption and emission cross section of Yb:YAG for different temperatures and the according FWHM	20
Figure 3.7	FWHM of the emission cross section and the corresponding pulse duration for different temperatures of Yb:YAG	21
Figure 4.1	Scheme of the CPA principle	23
Figure 4.2	Scheme of a stretcher-compressor arrangement	26
Figure 5.1	Scheme of the simulation of the upper-state population	29
Figure 5.2	Illustration of single-pass vs. multi-pass pumping	30
Figure 5.3	Effects of multi-pass pumping	30
Figure 5.4	Comparison of the amplification of a spectrally unshaped input spectrum vs. a spectrally shaped input spectrum	31
Figure 5.5	Results of a full simulation of the 1J-amplifier	33
Figure 6.1	Layout of the PFS pump laser	37
Figure 6.2	Input and output spectrum of the PCF	38
Figure 6.3	Measured autocorrelation trace and spectrum after the second fiber amplifier	38
Figure 6.4	Beam path through the stretcher	39
Figure 6.5	Detailed layout of the regenerative amplifier	40
Figure 6.6	Comparison between spectrally shaped and unshaped seeding of the regenerative amplifier	40
Figure 6.7	Detailed layout of the multi-pass amplifier	41
Figure 6.8	Photograph of the 4 kW pump setup and the generated pump beam profile in the crystal	41
Figure 6.9	Performance of the 8-pass amplifier and the according spectra	42
Figure 6.10	Input and output beam profile of the 8-pass amplifier	42
Figure 6.11	Technical drawing of the compressor	43
Figure 6.12	FROG evaluation of a compressed 200 mJ pulse	43
Figure 6.13	Detailed layout of the PFS pump laser including results	44
Figure 7.1	Examples of 4 horizontally-stacked, fast-axis collimated laser-diode bars and the arrangement of 16 such stacks in the pump module	47
Figure 7.2	Scheme of the homogenizing setup and pump beam profile of the 13 kW pump module	48
Figure 7.3	Pump power of the 13 kW module in dependence of the drive current and pump spectrum of the 13 kW module	48
Figure 7.4	Scheme of the thick-disk/active-mirror concept	49
Figure 7.5	Example of an Yb:YAG crystal glued on a heat sink	50

Figure 7.6	Photographs of the 8% \times 2 \times 20 Au1 crystal setup and of a 2% \times 6 \times 40 Ni1 crystal setup	51
Figure 7.7	Setup of a double-pass relay-imaging amplifier in 4 <i>f</i> -configuration	53
Figure 7.8	Extension of a double-pass to 4 and 8 passes in a planar geometry	54
Figure 7.9	Concept of a 3D 4-pass relay-imaging amplifier	55
Figure 7.10	Concept of the 3D 20-pass relay-imaging amplifier	57
Figure 7.11	Results of a wavefront analysis of the relay-imaging amplifier	58
Figure 7.12	Analysis of the influence of a thermal lens to the 20-pass relay-imaging amplifier	59
Figure 7.13	Counteracting a thermal lens with the 3D 20-pass relay-imaging amplifier setup	59
Figure 7.14	Mechanical design of the pump chamber	60
Figure 7.15	Mechanical design of the 3D 20-pass relay-imaging amplifier	61
Figure 7.16	Early version of the pump chamber	62
Figure 7.17	Carrier ring with a set of concave mirrors	62
Figure 7.18	Impressions of the tube inner arrangement I	62
Figure 7.19	Impressions of the tube inner arrangement II	62
Figure 7.20	Front part of the tube with pump module	62
Figure 7.21	The final vacuum arrangement	62
Figure 8.1	Typical input beam profile and seed spectrum for the low-energy campaign	65
Figure 8.2	Illustration of the regression analysis procedure	67
Figure 8.3	Example of the two-step procedure for determining the amplification performance	68
Figure 8.4	Results of the 2% \times 6 \times 20 Au1 crystal setup	69
Figure 8.5	Results of the 2% \times 6 \times 40 Au1 crystal setup	69
Figure 8.6	Results of the 6% \times 3 \times 20 Au1 crystal setup	70
Figure 8.7	Results of the 6% \times 3 \times 20 Ni 2 crystal setup	70
Figure 8.8	Results of the 8% \times 2 \times 20 Au1 crystal setup	71
Figure 8.9	Results of the 8% \times 2 \times 20 Ni 3 crystal setup	71
Figure 8.10	Low-energy seed spectrum and amplified spectrum	74
Figure 8.11	Comparison of the input beam profile and transmitted beam profile	74
Figure 8.12	Output beam profiles and wavefronts for different repetition rates	75
Figure 8.13	Extrapolated output energy	76
Figure 9.1	Beam profile in dependence of the repetition rate and position	77
Figure 9.2	Near-field beam profiles depending of the input/output energy at 1 Hz	78
Figure 9.3	High-energy amplification performance of the 2% \times 6 \times 40 crystal setup at 1 Hz and 2 Hz repetition rate	79
Figure 9.4	FROG evaluation of a compressed 1 J-pulse	80
Figure 9.5	Beam profile and wavefront at 1 J output energy for 1 Hz and 2 Hz repetition rate	81
Figure 10.1	Pump engine for the 10 J-amplifier	85
Figure 10.2	Multi-pass pumping setup with parabolic mirrors	86
Figure 10.3	Multi-pass pumping setup with a big lens	86
Figure 10.4	Design sketch for a 10 J-amplifier	87
Figure 10.5	Simulation results for a 10 J+ single-disk amplifier	89
Figure 10.6	Simulation results for a 10 J+ double-disk amplifier	90
Figure 10.7	Simulation results for a 10 J+ multi-slab amplifier	91
Figure A.1	Comparison of the numerical and analytical solution for the calculation of the upper-state population including ASE	101

LIST OF TABLES

Table 5.1	Fixed simulation parameters	32
Table 6.1	Key parameters of the PFS CPA pump laser system	44
Table 7.1	Overview of the crystals setups and their abbreviation	51
Table 8.1	Common parameters of the "low energy" campaign	66
Table 8.2	Summarized results of the low energy campaign	72

ACRONYMS

MPQ	Max-Planck-Institute for Quantum Optics
PFS	Petawatt Field Synthesizer
CPA	chirped pulse amplification
OPCPA	optical parametric chirped pulse amplification
OPA	optical parametric amplification
HEC-DPSSL	high-energy class, diode-pumped solid state laser
PCF	photonic crystal fiber
FWHM	full width at half maximum
LIDT	laser induced damage threshold
AOI	angle of incidence
TFP	thin-film polarizer
QWP	quarter-wave plate
ROC	radius of curvature
ASE	amplified spontaneous emission
PO	parasitic oscillations
CEO	carrier-envelope phase
GD	group delay
GDD	group delay dispersion
TOD	third-order dispersion
FOD	fourth-order dispersion
T_{eff}	effective crystal temperature
M_{ASE}	M_{ASE}
T_{hs}	heat sink temperature
f_{rep}	repetition rate
τ_{pump}	pump pulse duration

INTRODUCTION

1.1 Motivation

The demonstration of optical chirped pulse amplification (CPA) by *D.Strickland* and *G.Mourou* in 1985 [2] paved the way for the development of ultra-intense, high-energy laser systems. The basic idea of this principle is the reduction of the pulse intensity during the amplification process by extension of the pulse duration through a frequency-dependent delay called chirp. Doing so, much higher pulse energies can be achieved during amplification before reaching the critical intensities for the onset of non-linear effects or for damaging of the optics. After amplification, the introduced chirp is removed, restoring the ultra-short pulse duration. Nowadays, ultra-intense, high-energy CPA laser systems based on Ti:sapphire are commercially available and capable of delivering peak-powers >1 PW (>40 J, ≥ 25 fs) [12].

However, the compressed pulse duration of such systems is limited by the finite amplification bandwidth of the gain medium.

A solution for creating even shorter pulse durations is optical parametric amplification (OPA) [1] which is an amplification technique utilizing three-wave mixing, an optical phenomenon based on the χ^2 nonlinearities of a medium. The amplification is achieved via an energy transfer from monochromatic pump waves to the signal waves. Simultaneously, an idler wave under a certain angle is generated assuring energy and momentum conservation. One key prerequisite for efficient OPA is phase-matching between all the three waves which can be achieved in a birefringent crystal. However, for a broadband seed spectrum optimal phase-matching can only be achieved over a certain crystal length. Thus, thinnest crystals are necessary to support amplified bandwidths which are broader compared to high-energy CPA laser systems and allow for the generation of few-cycle pulses ≤ 10 fs.

For amplifying such few-cycle pulses to high energy with OPA one again has to utilize the CPA technique. This combination, dubbed optical parametric chirped pulse amplification (OPCPA) is capable of generating ultra high pulse powers in the TW to PW-range [7, 13].

The Max-Planck-Institute for Quantum Optics (MPQ) is pursuing OPCPA with the implementation of the Petawatt Field Synthesizer (PFS). The parameters of the PFS are a pulse energy of 5 J at a pulse duration of 5 fs and 10 Hz repetition rate. To achieve these goals one needs, on the one hand, a nearly octave-spanning seed spectrum and amplification bandwidth and on the other hand, a state-of-the-art ultra-intense, high-energy pump laser.

The typical efficiency of OPCPA is in the order of 20%. Possible pump lasers work in the near infrared spectrum and since the pump photons have to have a higher energy than the seed photons, frequency doubling of the initial pump pulses, at a typical efficiency of 50%, is necessary. So, in order to reach 5 J in the OPCPA beam, an initial pump energy of 50 J has to be provided. As mentioned before, the nonlinear crystals have to be very thin to support a broad amplified bandwidth, demanding high pump intensities to achieve sufficient single-pass gain. Thus, the required pump laser does not only have to deliver 50 J of pump energy but this also at 1 ps pulse duration, pushing the limits of rep-rated CPA systems.

In principle, a commercially available PW Ti:Sa-Laser could be used as a pump laser for such an OPCPA system but the major drawback of such systems is their poor wall-plug efficiency below 0.1%. The very short life time of the upper laser level in Ti:Sa ($\approx 3\mu\text{s}$) demands frequency-doubled, flash-lamp pumped, Q-switched Nd:YAG lasers as a primary pump source whose intrinsically low efficiency is the main reason for these poor figures.

As an alternative, PFS is pursuing a pump laser based on diode-pumped Yb:YAG since the developments in the last two decades made high-power laser-diode pump modules affordable. They allow for direct-pumping of Yb:YAG which, in addition to their long upper state life time, makes these lasers much more efficient. Furthermore, the thermal properties of Yb:YAG are also favourable, allowing for repetition rates beyond 10 Hz. An excellent example for the capabilities of diode-pumped Yb:YAG lasers are thin-disk lasers [14] which have been developed for 20 years and nowadays govern the market of industrial laser welding.

However, high-energy, diode-pumped Yb-doped CPA lasers are not commercially available yet. Therefore, the pump laser for PFS system is a new development.

The potential of high-energy, diode-pumped Yb-doped lasers is appreciated by several institutes and workgroups worldwide. Their research interests are ranging from the direct generation of fs-pulses in Yb-doped CPA laser systems to ns-systems delivering output energies of several kJ as drivers for inertial fusion energy (IFE). These developments founded the community of high-energy class, diode-pumped solid state lasers (HEC-DPSSLs). A compilation of state-of-the-art HEC-DPSSLs, mostly still under construction, is presented in the following listing.

- **Mercury - Lawrence Livermore National Laboratory, US**

Mercury was world's first HEC-DPSSL system, completed in 2007. Its unique design, based on multiple thin Yb:S-FAP slabs cooled in a He-gas flow, allowed for a still unmatched pulse energy of 55 J ($\tau_{\text{pulse}} = 14 \text{ ns}$, not CPA) at 10 Hz repetition rate [15].

- **POLARIS - Institut für Optik und Quantenelektronik, FSU Jena, DE**

POLARIS is a diode-pumped CPA laser system based on Yb:FP15 glass with the aim of generating 150 fs pulses with pulse energy of 150 J. So far, pulse energies up to 4 J with 164 fs pulse duration at a repetition rate of 1/40 Hz were realized [16, 17].

- **PEneLOPE - Institute for Radiation Physics, HZDR, Dresden, DE**

PEneLOPE - currently under development and construction - is a comparable system to POLARIS and also aiming for 150 J pulse energy. The main difference is the use of Yb:CaF₂ as gain material, allowing for pulse durations of 120 fs at an increased repetition rate of 1 Hz [18].

- **MBI Disk Laser - Max Born Institut, Berlin, DE**

The MBI develops a CPA laser system based on Yb:YAG thin-disk technology. So far, a maximum pulse energy of 320 mJ at 100 Hz repetition rate is reported [19].

- **GENBU - Institute of Laser Engineering, Osaka University, JP**

The GENBU CPA system aims at generating 1 kJ pulse energy at a repetition rate of 100 Hz. It is based on cryogenic-cooled total-reflection active-mirror (TRAM) Yb:YAG crystals, limiting the final pulse duration to 10-100 ps [20, 21].

- **Lucia - Laboratoire LULI, Ecole Polytechnique, Palaiseau, FR**

The LUCIA system is based on active-mirror Yb:YAG disks. Currently, 8 ns pulses (not CPA) are amplified in 3 stages up to 14 J pulse energy at 2 Hz repetition rate [22].

- **DiPOLE - Central Laser Facility, STFC Rutherford Appleton Laboratory, UK**

The DiPOLE project, aims on generating kJ pulses at 10 Hz repetition rate and is based on the MERCURY multi-slab concept. In a scaled-down prototype, a pulse energy of 10(6.4) J at 1(10) Hz repetition rate was demonstrated [23, 24].

Except the *Mercury* laser, all listed results were obtained while this thesis was carried out.

Again, the goals of the PFS CPA pump laser system are a pulse energy of 50 J, delivered in 4 pump beams, at a compressed pulse duration of 1 ps at 10 Hz repetition rate. The system will fully rely on diode-pumped Yb-doped materials, amplifying 4 ns-pulses in several amplification stages.

The main goal of the present thesis is the development of a new diode-pumped Yb:YAG amplifier module for the PFS CPA pump laser system, capable of delivering >1 J output energy.

1.2 Thesis outline

The theoretical foundation of the thesis is presented in Part i which contains a detailed description of laser pulse amplification (Chapter 2), the properties of Yb-doped laser materials (Chapter 3), with a special focus on the spectroscopic properties of Yb:YAG, and the introduction of the CPA concept (Chapter 4).

Based on the theory derived in Chapter 2, a simulation of laser pulse amplification in Yb:YAG has been developed which is presented in Part ii. The simulation is used to investigate certain features of the amplification in detail, such as multi-pass pumping and gain-narrowing, and to perform a full case study of a >1 J amplification stage.

The 1 J-amplifier is an upgrade to the previously implemented stages of the PFS CPA pump laser system which in the following will be designated as "pump frontend". In Part iii each functional unit of this pump frontend is described and characterized in detail, beginning from the seed-pulse generation and pre-amplification, over the stretcher and compressor setup and the two existing CPA amplification stages.

The 4th part (Part iv) is dedicated to the concept of the 1 J amplification stage. At first, the laser-diode pump module available for this amplifier is characterized in detail. Secondly, the individual Yb:YAG crystal assemblies, meaning Yb:YAG crystals bonded on certain heat sinks, are introduced. The main focus of this part is the development of a 20-pass relay-imaging amplifier. After outlining its concept, 3-D modelling and ray-tracing studies are presented in order to illustrate the feasibility and the benefits of this approach. Another important point addressed is the mechanical realisation of the 20-pass in the laboratory, as a lot of constraints have to be considered.

The experiments performed with the 20-pass relay-imaging amplifier are presented in Part v. Two measurement campaigns compare the amplification performance of the different Yb:YAG crystal setups at different repetition rates and heat sink temperatures, up to a maximum output energy of 400 mJ - both constituting the "low-energy" campaign (Chapter 8). Furthermore, the results of this campaign are used to perform a regression analysis with the simulation code introduced in Part ii. These evaluation results also help to identify the most promising crystal setup for the "high-energy" campaign presented in Chapter 9. Here, the - according to the low energy data - most promising crystal setup is characterized with regard to the maximum possible output energy at different repetition rates. Furthermore, the compression of these high-energy pulses is investigated.

Based on the results of the experiments and experiences with the 1 J-stage, concepts for an additional 10 J-amplifier are developed and presented in (Chapter 10). Finally the results of the thesis are summarized and an outlook is given (Chapter 11).

Part I

THEORY

In this chapter, the theory necessary for this thesis is introduced briefly. For further theoretical background the following standard works are recommended:

- Laser in general
 - *A.E. Siegman: "Lasers"* [25]
 - *O.Svelto: "Principles of Lasers"* [26]
 - *F.Träger: "Handbook of Lasers and Optics"* [27]
- Solid-state lasers
 - *W.Koechner: "Solid-State Laser Engineering"* [28]
- Description and measurement of ultra short laser pulses
 - *R.Trebino: "FROG: The Measurement of Ultrashort Laser Pulses"* [29]
- Literature in German
 - *J.Eichler, H.J.Eichler: "Laser: Bauformen, Strahlführung, Anwendungen"* [30]
- Online Encyclopedia
 - RP Photonics Encyclopedia, also available as a print version [14]

LASER PULSE AMPLIFICATION

This chapter is based on the ideas given in W.Koechner's "Solid-State Laser Engineering" [28].

2.1 The general idea of the laser

The fundamental principle of a *laser* - light amplification by stimulated emission of radiation - is stimulated emission. The idea of stimulated emission was introduced by A.Einstein in his publication from 1917 about the quantum theory of radiation [31]. Einstein described stimulated emission as the counterpart of the absorption and introduced the so-called *Einstein coefficient* B_{21} which describes the probability of this process in the presence of an electromagnetic field.

If one considers a hypothetical 2-level system consisting of two non-degenerated energy levels E_1 and E_2 with an energy separation of $\Delta E = h\nu_{21}$, an incident electromagnetic wave with the same frequency ν_{21} can excite e.g. atoms from the lower to the higher energy level. This process is called absorption. Its magnitude is proportional to the population density N_1 [1/cm³] of the lower state and the incident radiation density $\varrho(\nu_{21})$ [J/cm³]. The constant of proportionality is the *Einstein coefficient* B_{12} [cm³/Js]. The thus generated population of E_2 can then either decay spontaneously under the emission of photons with the frequency ν_{21} or, as Einstein proposed, the emission can be stimulated by an incident field. The photon emitted by stimulated emission has the same properties (frequency, polarization, phase) as the incident one. A scheme of a 2-level system and the possible transitions are depicted in the left of Figure 2.1. The formulae describing these transitions are shown on the right.

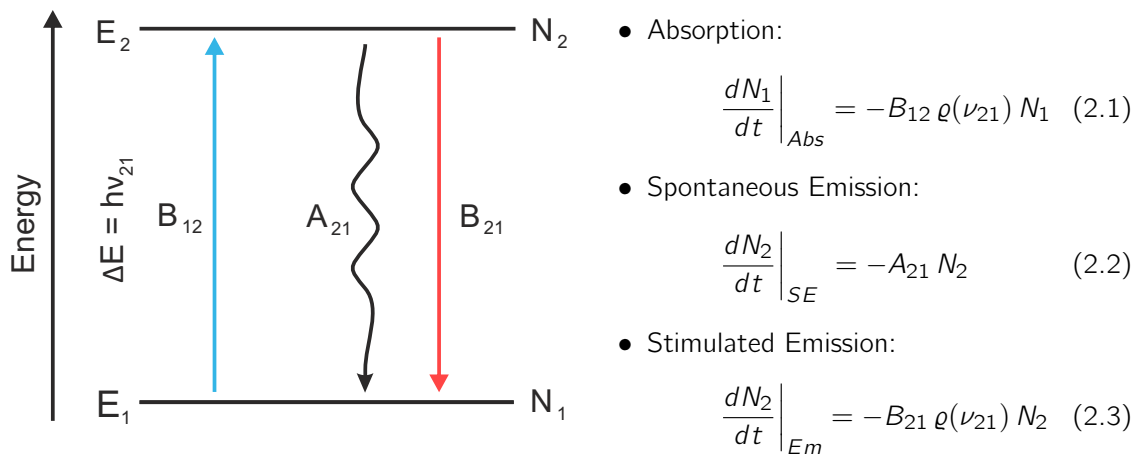


Figure 2.1: Scheme of 2-level system and the possible transitions. B_{12} indicates absorption, A_{21} spontaneous emission and B_{21} stimulated emission. The formulae describing these transitions are shown on the right. A_{21} and $B_{12/21}$ are called *Einstein coefficients*.

The solution of Equation 2.2 is:

$$N_2(t) = N_2(0) \exp\left(\frac{-t}{\tau_{21}}\right) \quad (2.4)$$

τ_{21} is the reciprocal of the *Einstein coefficient* A_{21} . It is denoted as the lifetime for spontaneous decay of level E_2 . In general, τ_{21} is called fluorescence life time τ_f .

Under the assumption of thermal equilibrium, the relative population density of the two energy levels is given by the *Boltzmann equation* (cf. [28]). Furthermore the net number of transitions between the two levels is zero. In comparison with *Planck's law* (cf. [28]) one can show [28] that:

$$\frac{A_{21}}{B_{21}} = \frac{8 \pi h \nu_{21}^3}{c^3} \quad (2.5)$$

$$B_{12} = B_{21} \quad (2.6)$$

The *Einstein coefficient* B_{21} can be reformulated by introducing a measurable cross section σ_{21} [cm^2] for the transition [28]:

$$B_{21} = \frac{c}{h\nu_{21}} \sigma_{21} \quad (2.7)$$

Now, we can rewrite e.g. Equation 2.1 in terms of the photon density $\phi = \rho_{21}/h\nu_{21}$ [$1/\text{cm}^3$]:

$$\frac{dN_1}{dt} = -\sigma_{21} c \phi N_1 \quad (2.8)$$

The number of transitions equals the change in the photon density:

$$\frac{dN_1}{dt} = \frac{d\phi}{dt} \quad (2.9)$$

This relation can be reformulated using $c = dx/dt$ and thus:

$$\frac{d\phi}{dx} = \frac{1}{c} \frac{dN_1}{dt} = -\sigma_{21} \phi N_1 \quad (2.10)$$

Using a more practical quantity - the Intensity $I = c h\nu_{21} \phi$ [J/s cm^2], Equation 2.10 resembles the *Beer-Lambert law* of absorption:

$$\frac{dI}{dx} = -\sigma_{21} N_1 I \quad (2.11)$$

Equation 2.3, which describes the spontaneous emission, can be reformulated in an analog way. Combining of Equation 2.3ff and Equation 2.11 and solving leads to:

$$\frac{I}{I_0} = \exp(\sigma_{21} (N_2 - N_1) d) \quad (2.12)$$

One clearly sees that if one could prepare such a 2-level system in a way that $N_2 > N_1$, the so-called population inversion, the incident radiation would be amplified along the distance d . This is the fundamental principle of the laser.

Without incident radiation the population of the the two energy levels is given by the *Boltzmann equation* (cf. [28]) and thus $N_2 < N_1$. In this case, any incident radiation ν_{21} is absorbed and results in a higher population of N_2 . At the point when $N_2 = N_1$ the number of emissions equals the number of absorptions due to the same transition probabilities, i.e. the same cross sections, for both transitions. A population inversion can not be achieved in such a hypothetical 2-level system.

Fortunately, "real" systems e.g. solid-state media or molecules usually have more than two energy levels. This feature can be used to create the necessary population inversion.

2.2 Multiple-level systems

Three-level system

The first idea to create a population inversion is to utilize a third energy level as sketched in a simplified manner in Figure 2.2 a). The incident pump radiation ν_P induces transitions from the ground-state $|1\rangle$ to the pump level $|3\rangle$. This state decays within τ_{32} into the upper laser level $|2\rangle$. If $\tau_{32} \ll \tau_{21}$, the number of excited states N_3 is very small compared to N_1 and N_2 and one can assume that $N = N_1 + N_2$. Thus, requiring $N_2 > N/2$ for the amplification of incident radiation in a three-level system.

The most prominent 3-level laser medium is ruby ($\text{Cr}^{3+}:\text{Al}_2\text{O}_3$), which was used by T.Maiman to experimentally show stimulated emission in the visible range for the first time [32].

Four-level system

Although amplification is possible in a three-level system, high pump rates are necessary to achieve $N_2 > N/2$. One can circumvent this problem by utilizing a fourth energy level, the lower laser level (denoted $2\rangle$ in this case). A scheme of a four-level system is shown in Figure 2.2 b). If $\tau_{21} \ll \tau_{32}$, the lower level is practically empty at all times and thus any population of the upper laser level N_3 will lead to amplification of the incident radiation.

A widely used four-level laser material is Nd:YAG ($\text{Nd}^{3+}:\text{Y}_3\text{Al}_5\text{O}_{12}$).

Quasi three-level system

As mentioned before, the thermal population of the energy-levels is governed by the *Boltzmann distribution*. So, if the energy spread between the ground state and lower laser level in a four-level system is on the order of $\approx kT$ the lower laser level will be populated at room temperature. Such a system is called quasi-three-level system and its amplification behaviour is strongly influenced by the temperature.

Yb:YAG ($\text{Yb}^{3+}:\text{Y}_3\text{Al}_5\text{O}_{12}$) at room temperature is a typical quasi-three-level system.

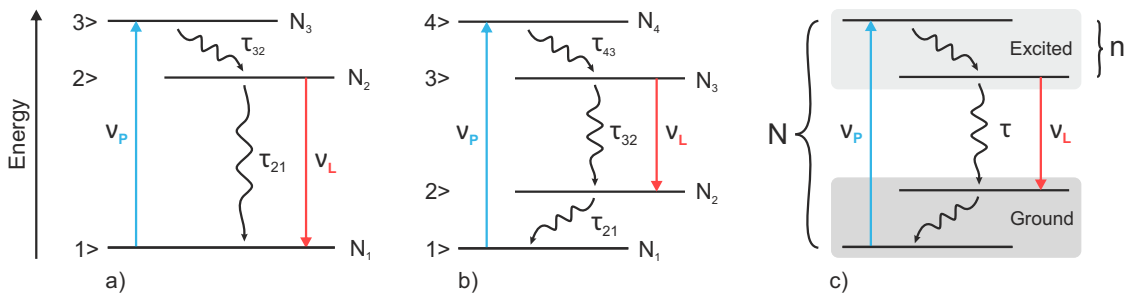


Figure 2.2: Scheme of a three-level a) and a four-level b) system. Both systems can be treated simplified as two level system, shown in c), if the lifetime of the upper laser level is very large compared to the lifetime of the upper pump level and, in case of the four-level system, compared to the lower laser level.

In reality, the pump and lasing transitions ν_P and ν_L are not "sharp" as explained and shown in Figure 2.2. Usually, a certain bandwidth $\Delta\nu_P$ can be absorbed and $\Delta\nu_L$ amplified. Under the assumption of a very short lifetime of the upper pump level compared to the lifetime of the upper laser level, and additionally a short lifetime of the lower laser level in case of a four-level system, these systems can simply be treated theoretically as a two-level system. In the following, the total number of states per volume is denoted N and the number of excited states per volume is n , see Figure 2.2 c).

2.3 Creation of a population inversion

A population inversion can be created by pumping a laser medium at a suitable pump wavelength λ_P with an intensity I_P . In the case of pulsed amplification, as in the present thesis, the laser medium is usually pumped for a certain pump pulse duration t_P . During pumping, the population inversion is not depleted via stimulated emission and therefore pumping and amplification can be treated independently. However, spontaneous emission occurs while pumping leading to a depletion of the inversion.

With the formulae and quantities introduced in Section 2.1 and the 2-level assumption introduced in Section 2.2 the time-dependent population of the upper level can be expressed as follows:

$$\frac{dn}{dt} = W_P (N - n) - \frac{n}{\tau_f} \quad (2.13)$$

Here W_P is the pump rate, the number of transitions per second, which can be expressed as:

$$W_P = \frac{\sigma_P \lambda_P}{h c} I_P \quad (2.14)$$

The differential equation 2.13 can be solved analytically and yields:

$$n(t) = \frac{\tau_f W_P}{\tau_f W_P + 1} N \left(1 - e^{-t \left(W_P + \frac{1}{\tau_f} \right)} \right) \quad (2.15)$$

In comparison, the solution for the pure absorption is:

$$n(t)_{Abs} = N \left(1 - e^{-t W_P} \right) \quad (2.16)$$

For $t_P \gg \tau_f$ (W_P const.), the ratio between excited and absorbed states, i.e the ratio between energy available for amplification and absorbed energy, is:

$$\frac{n(t)}{n(t)_{Abs}} = \frac{\tau_f W_P}{\tau_f W_P + 1} \quad (2.17)$$

One defines:

$$\tau_f W_P = \frac{\tau_f \sigma_P \lambda_P}{h c} I_P = \frac{I_P}{I_{Sat}} \quad (2.18)$$

$$I_{Sat} = \frac{h c}{\tau_f \sigma_P \lambda_P} \quad (2.19)$$

I_{Sat} is the saturation intensity - a laser material specific constant - which corresponds to the pump intensity necessary to achieve a upper state population of $N/2$ for $t_P \gg \tau_f$.

2.4 Laser pulse amplification

As mentioned before, the generation of the inversion and the amplification can be treated separately. Pumping with an intensity I_P for t_P leads to n excited states per volume at the end of the pump pulse duration. In the case of pulsed amplification, the pulse duration t_p of the laser pulse is assumed to be much shorter compared to the pumping time t_P and the fluorescence lifetime τ_f . Therefore, both terms can be neglected when calculating the amplification. The depletion of the upper laser level then just occurs via stimulated emission.

This interaction of the laser pulse with the inversion in the laser medium is characterized by the nonlinear, time-dependent photon-transport equation [28], describing the change of the photon density in a small volume as:

$$\frac{\partial \phi}{\partial t} = c \sigma_L \phi n - \frac{\partial \phi}{\partial x} c \quad (2.20)$$

with $\left(\frac{\partial \phi}{\partial x} c\right)$ characterizing the photon flux exiting the considered region and

$$\frac{\partial n}{\partial t} = -c \sigma_L \phi n \quad (2.21)$$

describing the population inversion.

To calculate the amplification of the incident pulse, the coupled differential equations 2.20 and 2.21 have to be solved. A solution was first presented by *Frantz and Nodvik* [33] who calculated the amplified photon density to:

$$\phi(x, t) = \left\{ 1 - [1 - \exp(-\sigma_L n x)] \exp\left[-\sigma_L \phi_0 c \left(t - \frac{x}{c}\right)\right] \right\}^{-1} \phi_0 \quad (2.22)$$

Assuming a rectangular pulse shape with a pulse duration t_p and an initial photon density ϕ_0 , the gain in a laser medium with the length l and n excited states can be calculated to [33]:

$$G = \frac{1}{c \sigma_L \phi_0 t_p} \ln\{1 + [\exp(\sigma_L \phi_0 t_p c) - 1] \exp(\sigma_L n l)\} \quad (2.23)$$

One can reformulate this equation using directly measurable laser parameters:

$$G = \frac{F_{Sat}}{F_{in}} \ln \left\{ 1 + \left[\exp\left(\frac{F_{in}}{F_{Sat}}\right) - 1 \right] \exp(\sigma_L n l) \right\} \quad (2.24)$$

Here F_{in} is the input fluence [J/cm^2] of the laser pulse and F_{sat} the saturation fluence, a combination of characteristic values of the laser material which is defined as:

$$F_{Sat} = \frac{hc}{\sigma_L \lambda_L} \quad (2.25)$$

The limits of gain G in case of low and high input fluence are given by:

$$F_{in} \ll F_{Sat} \Rightarrow G \approx \exp(\sigma_L n l) = \exp(g_0 l) \quad (2.26)$$

$$F_{in} \gg F_{Sat} \Rightarrow G \approx 1 + \left(\frac{F_{Sat}}{F_{in}}\right) g_0 l \quad (2.27)$$

So, for small input signals the amplification of the incident laser pulse is exponential with length of the laser medium. $G_0 = \exp(g_0 l)$ is commonly denoted the "small signal gain".

For strong input signals, the gain tends to be linear with the length of the amplifier. According to [28] this implies "that every excited state contributes its stimulated emission to the beam. Such a condition obviously represents the most efficient conversion of stored energy to beam energy".

2.5 Amplified spontaneous emission

In the previous section, the amplification of an incident pulse was described and in general this radiation is the main source for the depopulation of the upper laser level. However, also the spontaneously emitted photons described in Section 2.3 are amplified in the same way. This effect is called amplified spontaneous emission (ASE).

The emission of a spontaneously emitted photon can occur at every point in the pumped volume in all solid angles during the whole pumping time. These photons will experience a gain, see Equation 2.27, $G_{ASE} = \exp(\sigma_{ASE} n L_{char})$, where σ_{ASE} is the mean emission cross section for spontaneous emission and L_{char} the characteristic length of the system. So, ASE becomes relevant either if the population density is high, typically in high-gain amplifiers, or if the characteristic length is large.

Normally, one would assume that L_{char} is the longest extent of the pumped volume. But spontaneously emitted photons which leave the pumped volume can also be back-reflected into it, which increases L_{char} . One source for back-reflections are the optics which are used to set up several amplification passes for the pulse to be amplified. Another source are internal (total) reflections in the laser medium, e.g. at the edges of a laser crystal. In the latter case even stable oscillations, i.e. whispering gallery modes, can occur if the total gain - amplification in the pumped area and reflection losses at the edges - per round-trip exceeds 1. In this case a much larger L_{char} has to be assumed. These oscillations are named parasitic oscillations or parasitic effects, where ASE mostly denotes effects which are recognizable in the direction of the laser pulse.

So, both effects can depopulate the upper level and thus reduce the gain and the output energy which can be interpreted qualitatively as an effective shortening of the fluorescence time. As mentioned this problem mainly occurs in high gain amplifiers and in amplifiers for high energies, since they have large apertures and therefore large transverse sizes to prevent laser induced damage.

A proper theoretical description of the ASE is given in the publication of *Barnes and Walsh* [34]. They deduce a correction term for the creation of the population inversion, cp. Equation 2.13, which then reads:

$$\frac{dn}{dt} = W_P (N - n) - \frac{n}{\tau_f} \exp(\sigma_{ASE} n L_{char}) \quad (2.28)$$

The correction term $\exp(\sigma_{ASE} n L_{char})$ exactly reflects the qualitative description - the effective fluorescence life time is reduced. The higher the population density n and/or the longer the characteristic length L_{char} the shorter the effective upper state lifetime.

Equation 2.28 has to be solved numerically. Alternatively, one can approximate $\exp(\sigma_{ASE} n L_{char})$ by a constant factor called M_{ASE} and so the equation can be solved analytically to:

$$n(t) = \frac{\tau_f W_P}{\tau_f W_P + M_{ASE}} N \left(1 - e^{-t \left(W_P + \frac{M_{ASE}}{\tau_f} \right)} \right) \quad (2.29)$$

However, the correctness of this approximation has to be verified. A comparison of the time-dependent behaviour of Equation 2.28 and Equation 2.29 can be found Appendix A. It was found that for pumping times in the order of τ_f and larger the constant M_{ASE} approach reproduces Equation 2.28 perfectly.

(2.30)

The long-term solution of Equation 2.29 reads to:

$$\frac{n(t)}{n(t)_{Abs}} = \frac{\tau_f W_P}{\tau_f W_P + M_{ASE}} = \frac{I_{pump}/I_{sat}}{I_{pump}/I_{sat} + M_{ASE}} \quad (2.31)$$

So, $M_{ASE} = 1$ equals the absence of parasitic effects or ASE - only spontaneous emission depletes the upper laser level. At $M_{ASE} = 0$ also the spontaneous emission is neglected during calculation, hence Equation 2.29 then describes the absorption of the pump light. Figure 2.3 illustrates the impact of the M_{ASE} and the pump intensity on the upper state population. The effect of M_{ASE} at $I_{pump} = I_{sat}$ is shown in subfigure a) and b) illustrates the time-dependent upper state population for different pump intensities. One can clearly see that the larger M_{ASE} the lower the maximum achievable upper-state population and hence the amplification.

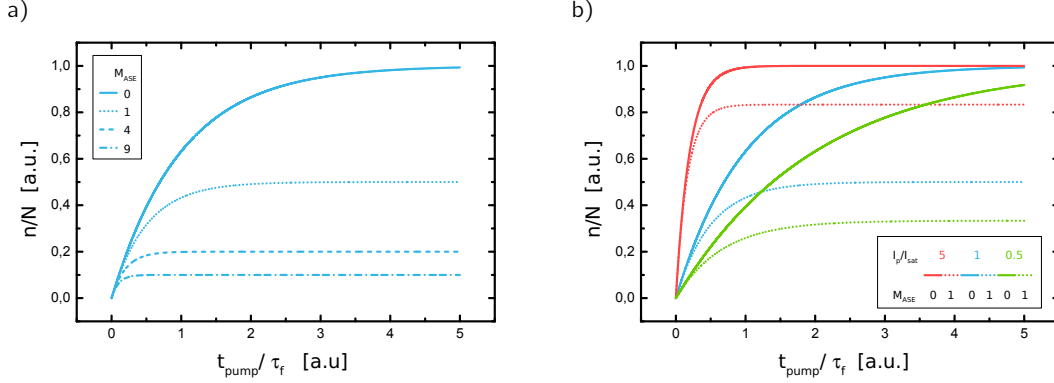


Figure 2.3: Impact of M_{ASE} and pump intensity on the upper-state population. Subfigure a) illustrates the effect of the M_{ASE} at $I_{pump} = I_{sat}$. The time-dependent upper state population in dependence of the pump intensity is shown in b). $M_{ASE}=0$ corresponds to the amount of absorbed states while $M_{ASE} = 1$ reflects the upper state population regarding spontaneous emission which is the maximal achievable population density. One can clearly see that the larger M_{ASE} the lower the maximum achievable upper state population and hence the amplification.

Barnes and Walsh described how ASE reduces the effective upper state population. As described before, these emitted photons can, if somehow back-reflected to the pumped volume, lead to parasitic oscillations. Under the simple assumption - a more detailed description can be found in [35] - that a spontaneously emitted photon from the center of the laser medium is back-reflected once from the edge of the laser medium with a reflectivity R , the total gain, neglecting absorption in unpumped area, is:

$$G_{ASE} = R e^{g_0 D} \quad (2.32)$$

D is a characteristic length, e.g. the pump diameter, and R a characteristic reflectivity, i.e. $R = 0.086$ for an air/YAG interface. For $G_{ASE} > 1$ parasitic oscillations are possible. As described before, Yb:YAG exhibits a significant amount of reabsorption of laser radiation depending on the crystal temperature. Also the reabsorption of the ASE in unpumped areas of the crystals has to be taken into account as well as the pump intensity and the pump pulse duration. One can derive for $G = 1$:

$$\ln R = \underbrace{K(1-E)N_{yt}c_{dop}\sigma_{em}D}_{\text{Amplification}} - \underbrace{K E N_{yt}c_{dop}\sigma_{abs}D}_{\text{Absorption}} - \underbrace{N_{yt}c_{dop}\sigma_{abs}D_{unp}}_{\text{Reabsorption}} \quad (2.33)$$

$$\text{with: } K = \frac{I_P}{I_{sat} + M_{ASE}} \quad \text{and} \quad E = \exp\left(\frac{-t_P}{\tau_f} \left(\frac{I_P}{I_{sat}} + M_{ASE}\right)\right)$$

N_{yt} [1/cm³] denotes the nuclear density of Yttrium ions in YAG, c_{dop} [at. %] the Ytterbium doping concentration, σ_{em} [cm²] and σ_{abs} [cm²] the emission and absorption cross section at 1030 nm, D [cm] the amplification length and D_{unp} [cm] the length of the unpumped region.

Reformulating Equation 2.33 leads to a critical product of $D \times c_{dop}$. Figure 2.4 illustrates this product for Yb:YAG at room temperature taking a reflectivity of $R = 0.086$, $R = 0.018$ resp. and an absorption length $D_{unp} = 1$ cm into account. $R = 0.018$ corresponds to the commonly used threshold for the onset of parasitic oscillations of $g_0 D = 4$. For the of calculation of the critical product M_{ASE} is set to 0.

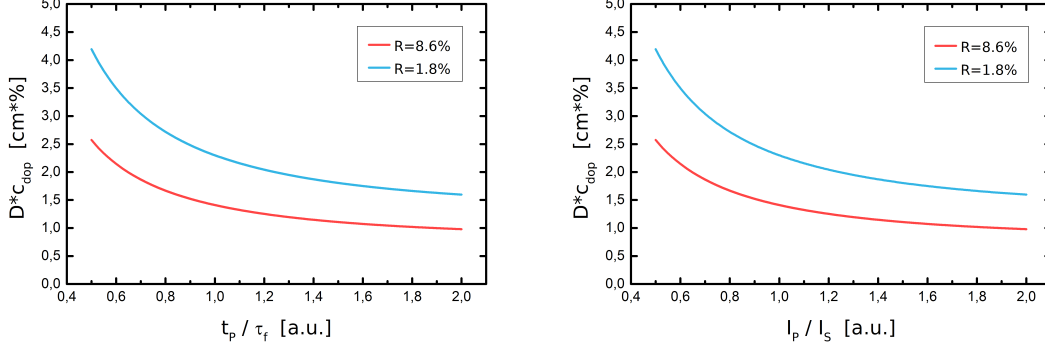


Figure 2.4: Critical product of doping concentration and pump spot diameter for Yb:YAG at room temperature assuming $R = 0.086$, $R = 0.018$ resp. and $D_{unp} = 1$ cm. In subfigure a) the pump intensity is kept constant ($I_p = I_{sat}$) and the pump pulse duration is varied while in subfigure b) the pump pulse duration is kept constant. Assuming a pump diameter and absorbing length of each 1 cm and pumping with I_{sat} and τ_f the critical doping concentration c_{dop} for the onset of parasitic oscillations is $\approx 1.4\%$ for $R = 0.086$ and $\approx 2.3\%$ assuming $R = 0.018$. For the of calculation of the critical product M_{ASE} is set to 0.

The calculation shown in Figure 2.4 reveals a critical doping concentration c_{dop} for the onset of parasitic oscillations of $\approx 1.4\%$ for $R = 0.086$ and $\approx 2.3\%$ in the case of $R = 0.018$ at an assumed pump diameter and absorbing length of each 1 cm and pumping with I_{sat} and τ_f . At a higher doping concentration, parasitic oscillations are in principle possible. However, the real influence of these parasitic effects on the inversion, meaning the maximum stored energy, can only be calculated with a proper 3D ray-tracing amplification simulation.

2.6 Summary

In this chapter the requirements for laser amplification and the amplification process itself were presented and the corresponding equations were derived. In the pulsed-amplification scheme, pumping of the laser material and the amplification of the laser pulse can be treated independently. However, parasitic effects and ASE can occur while pumping the gain material and lead to a severe depopulation of the upper laser level and hence a reduced stored energy. The equation describing the pumping of the gain material was extended by an factor M_{ASE} , cp. Equation 2.29, to account for these losses. Furthermore, a threshold criterion for the onset of parasitic effects was derived. All presented equations only regard the monochromatic case. Nevertheless, the derived formulae for pumping and amplification are the foundation for a polychromatic simulation of the laser pulse amplification which is extensively described in Chapter 5.

GAIN MATERIAL

This chapter follows the ideas given by W. Krupke [36] and M. Siebold [37] and measurements conducted by J.Körner et al. [38, 39, 40].

3.1 General considerations

The invention of laser diodes in 1962 and their fast evolution starting from the late 1980s lead to new possibilities of optical laser pumping. In comparison to the established flash-lamps, for pumping high-energy laser systems, laser diodes exhibit an increased spectral brightness. The emitted pump radiation is confined in a much narrower spectral bandwidth, typically a few nm compared to several hundred nm for flash-lamps. The resulting main advantages of laser-diodes are their higher wall-plug efficiency, meaning the fraction of electrical energy actually transferred into usable pump radiation, which is important for high-repetition rate systems, and the resulting lower amount of pump energy transferred into heat in the laser material. A drawback is the small output power of a single laser diode. Typically several emitters are combined in a so-called bar, leading to a state-of-the-art output power of ≈ 300 W per bar. Several of these bars are assembled to stacks which then are optically combined to get the desired output power. The large number of necessary emitters leads to high investment costs per kW of installed pump power. Increasing interest in diode-pumping over the last decade and new developments lead to decreasing prices. Additionally the running costs of laser-diode modules are much lower compared to flash-lamps. Thus, laser-diode modules may replace flash-lamp pumping in the future.

Nowadays, the established way of generating short laser pulses in the range of <1 ps with high pulse energies in the range of >100 J is utilizing the CPA principle, as explained in Chapter 4, in combination with flash-lamp pumped Nd:glass as amplifier medium. Thus, output powers in the range of 1 PW were demonstrated [41, 42]. The main drawback of such laser systems is the limited shot period of ≈ 1 -6 shots per hour due to the low thermal conductivity of glass in combination with the large amount of heat introduced by flash-lamp pumping. This problem can be alleviated by using diodes as a pump source. However, even with diode pumping, the low thermal conductivity of glass permits repetition rates above 1 shot per minute which is too slow for our application. An alternative to glass is YAG ($\text{Y}_3\text{Al}_5\text{O}_{12}$) which has a ≈ 10 times higher thermal conductivity than glass. Unfortunately, the change of the host material comes along with a change of the spectral properties. The absorption bandwidth is reduced to <1 nm requiring stabilized laser-diodes for pumping which have even higher investment costs compared to standard laser-diodes ($\Delta\lambda \approx 6$ nm) and furthermore the amplification bandwidth of Nd:YAG limits the pulse duration to >10 ps. Thus, Nd:YAG is not suitable as laser material for diode-pumped, high-energy CPA pump systems generating pulse durations <1 ps.

In the course of developing such systems Ytterbium-doped materials became of special interest since they exhibit broader absorption and emission bandwidths compared to Nd-doped materials. Furthermore, the long fluorescence time of Yb-doped materials, e.g. ≈ 1 ms for Yb:YAG [43, 44], allows for cost-efficient optical pumping.

A comparison of Yb-doped materials and a detailed description of Yb:YAG as laser material is presented on the next pages.

3.2 Yb-doped laser materials

Several host materials were investigated during the last decade regarding their properties when doped with Ytterbium. A good comparison between Yb-doped and other laser materials can be found in the publication of *M. Siebold et al.* [37].

As explained before, a broad emission bandwidth is necessary for short pulse generation. Furthermore, a long fluorescence lifetime enables cost-efficient optical pumping because lower pump intensities can be used to deposit the same amount of energy, see Section 2.3. An additional criterion for the choice of a suitable laser material is its saturation fluence F_{Sat} - the fluence which is needed to efficiently extract energy, see Section 2.4. However, a too low F_{Sat} also enables high energy extraction through ASE. At a too high F_{Sat} on the other hand, the LIDT is reached before efficient extraction can be achieved. Figure 3.1 a) illustrates the suitability of different laser materials regarding energy extraction (lower F_{Sat} are preferable) and energy storage (longer fluorescence time is preferable). The ability of short pulse generation in combination with the fluorescence time is depicted in subfigure b).

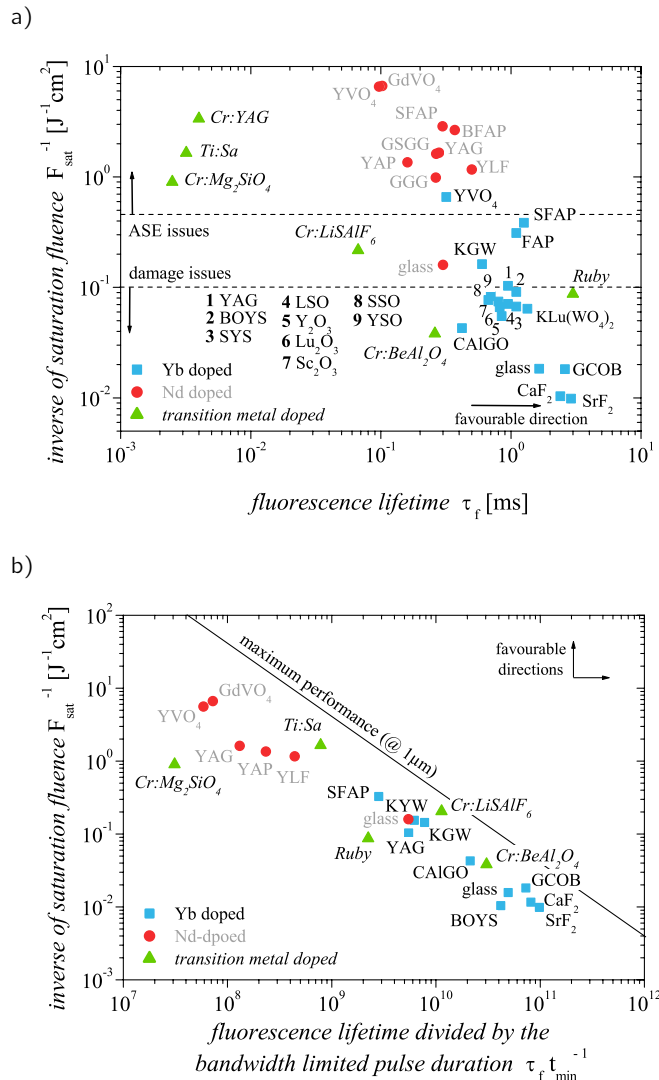


Figure 3.1: Comparison of different laser materials regarding fluorescence time τ_f and saturation fluence F_{Sat} a) plus their ability for short pulse generation b) according to [37], with kind permission from Springer Science and Business Media. A low saturation fluence F_{Sat} ensures efficient energy extraction. A too low F_{Sat} on the other hand enables high energy extraction through ASE. For larger F_{Sat} the LIDT limits efficient extraction. Long fluorescence times τ_f are favourable for diode pumping because lower pump intensities can be used to deposit the same amount of energy in this case. The suitability for the generation of short pulses is determined by the bandwidth of the emission cross section.

Yb-doped materials show broadband absorption in a range from 900 nm to 1040 nm. Again, the characteristic of the cross section strongly depends on the atomic structure of the host material. All materials shown a distinct peak between 970 nm and 980 nm. Although the bandwidth of these peaks may be broad enough for standard-diode pumping the emission cross sections, see Figure 3.4, are in the same order and therefore prevent high inversion levels. The more suited spectral range for pumping Yb-doped materials is around 940 nm, especially in the case of Yb:YAG which exhibits a broad peak with a spectral bandwidth of ≈ 10 nm and absorption cross sections comparable to the main peak. A collection of absorption spectra of different Yb-doped materials is shown in Figure 3.2. These cross sections were measured by *J.Körner et al.* [38, 39].

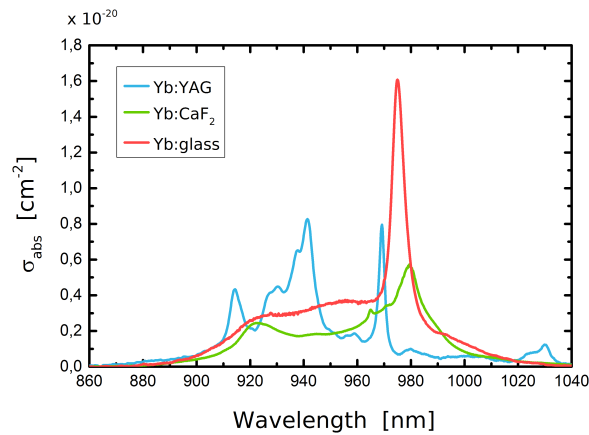


Figure 3.2: Absorption cross sections of different Yb-doped materials, according to *J.Körner et al.* [38, 39]

For high repetition rate operation of the laser system the thermal properties of the laser material also play a very important role. Materials with a high thermal shock parameter and a high thermal conductivity a preferable. In his dissertation *D.Albach* [45] collected these properties for some widely used host materials. Figure 3.3 shows his findings.

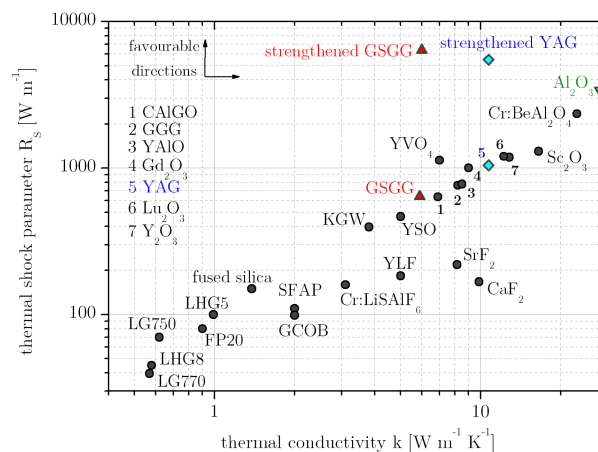


Figure 3.3: Thermal shock parameter R_S in dependence of the thermal conductivity k for different host materials. Materials with a high thermal shock parameter and a high thermal conductivity a preferable. Taken from [45] with kind permission from *D.Albach*.

In addition to the mentioned physical criteria also practical aspects limit the range of possible laser materials for ultra-high peak-power lasers. An important limiting factor is the laser induced damage threshold (LIDT). In good approximation the LIDT of the mentioned materials is in the range of 5 J/cm^2 for 10 ns pulse duration. This leads to necessary laser material diameters easily exceeding 1 cm for pulse energies larger than 10 J. Furthermore, in the context of laser development, these large samples have to be available from a reliable supplier with mature manufacturing processes on a short time scale with flexible doping concentration and at moderate prices.

Taking all the mentioned physical and practical/technical criteria into account, the most promising Yb-doped materials for high repetition rate, ultra-high peak-power lasers are Yb:YAG and Yb:CaF₂. While the latter is predestined for the generation and amplification of ultra-short pulses in the range of 200 fs the spectral bandwidth of Yb:YAG is sufficient for the generation and amplification of few-ps pulses which is our aim. Furthermore, its lower saturation fluence allows for a higher efficiency. Due to its similarity to Nd:YAG which has been used for flash-lamp pumped lasers for decades the market for Yb:YAG crystals is very competitive. However, traditional Yb:YAG crystals are limited in sample size and doping concentration due to the growing process. This problems can be overcome by using ceramic Yb:YAG which became accessible in the last years.

3.3 Spectroscopic properties of Yb:YAG

Following the criteria given in the previous section, Yb:YAG is the most promising laser material for our purpose. In this section, the spectroscopic properties of Yb:YAG will be presented in detail. As explained in Section 2.2, Yb:YAG is a quasi 3-level system, meaning that the population of the lower laser level is temperature-dependent. Hence the spectroscopic properties strongly depend on the crystal temperature. The most comprehensive studies of this topic so far have been carried out by *J.Körner et al.* [38, 39, 40]. They investigated the temperature dependence of the absorption and emission cross section for several Yb-doped materials, including Yb:YAG.

The figures presented in the following section are based on the results of their measurements which they generously provided.

Figure 3.4 illustrates the absorption a) and emission b) cross sections of Yb:YAG between 900 nm and 1100 nm for different temperatures. The two major absorption peaks are located at 969 nm and 940 nm and thus predestined for diode-pumping. The latter is favourable since it exhibits a broader bandwidth and so the requirements for the pump diodes are less stringent. A zoomed-in view of this absorption peak is shown in c). The main emission peak is centred around 1030 nm, zoomed-in shown in d). The temperature-dependence is clearly evident.

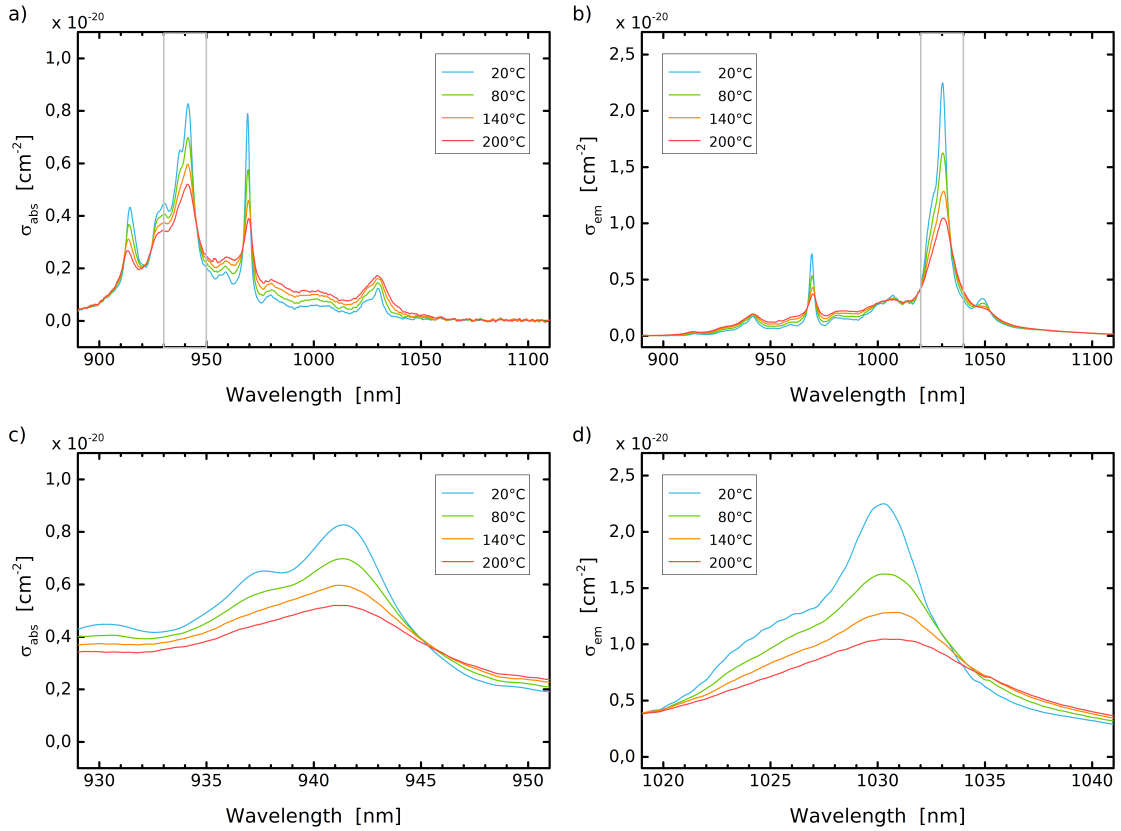


Figure 3.4: Absorption a) and emission b) cross sections of Yb:YAG for different temperatures and enlarged illustrations of the main peaks of absorption c) and emission d). The data are plotted according to [39].

The data presented in Figure 3.4, based on [39], only contains cross sections measured at room-temperature and higher. The latest measurements of *J.Körner et al.* aimed on measuring the cross sections for temperatures below room-temperature [40]. The data from this campaign and the data from [39] were merged and interpolated to get a complete overview of the cross sections for temperatures between 80 K and 470 K. Figure 3.5 illustrates contour plots of the absorption a) and emission b) cross sections.

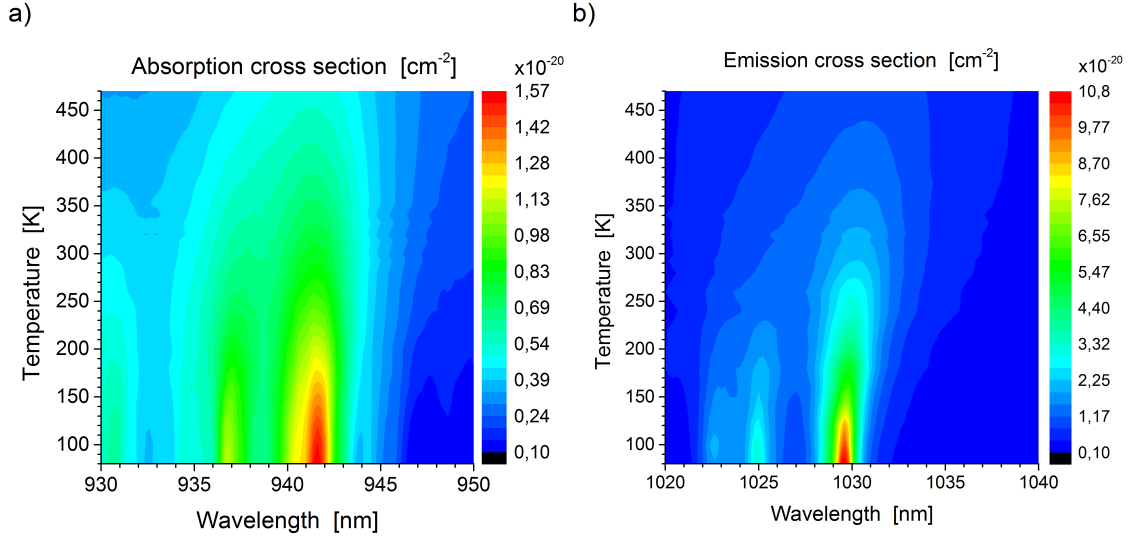


Figure 3.5: Contour plots of the absorption a) and emission b) cross sections of Yb:YAG for different temperatures. Based on data provided by *J.Körner et al.* [39, 40]. *The plots have individual colorbars.*

The peak absorption cross section around 940 nm increases by a factor of ≈ 3 when cooling down from 470 K to 80 K. At the same time the peak emission cross section is enhanced by a factor of ≈ 11 . The according slopes are depicted in red in Figure 3.6. While the peak cross sections show an increase with lower temperatures the according FWHM of the absorption and emission bandwidth is decreased. Additionally, the double peak structure of the bandwidths gets more pronounced. Again, this effect is more severe for the emission cross section which show a decrease of the FWHM by a factor of ≈ 15 while the change in the FWHM of the absorption is a factor of ≈ 3 . The change of the bandwidths is illustrated in blue in Figure 3.6.

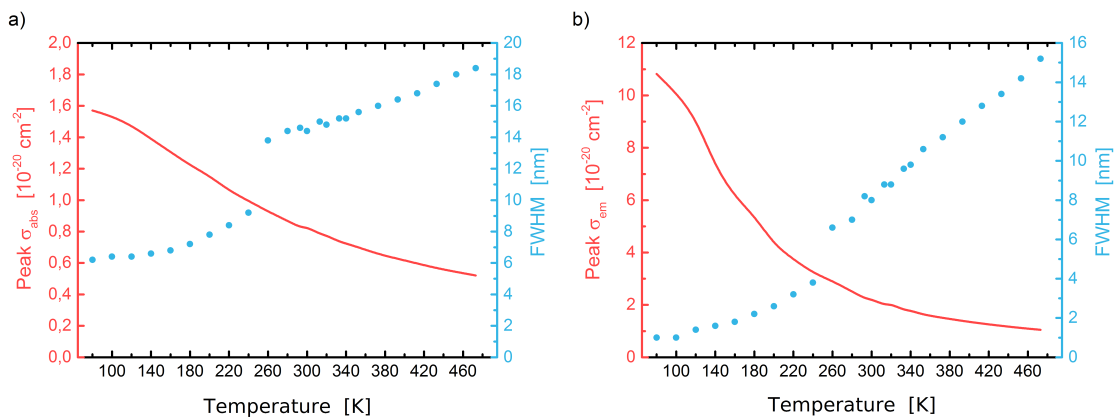


Figure 3.6: Peak absorption (a, red) and emission (b, red) cross section of Yb:YAG for different temperatures. The according FWHM is plotted in blue. The discontinuity of the FWHM slope originates from to the double peak structure of the cross sections. Based on data measured by *J.Körner et al.* [39, 40]

Consequently, by cooling Yb:YAG down to cryogenic temperatures the emission cross section and hence the amplification performance can be raised drastically. At the same time the amplified bandwidth will drop leading to longer *Fourier*-limited pulse durations. This effect is illustrated in Figure 3.7. The pulse duration is calculated under assumption of Gaussian shaped spectrum with the same FWHM as the emission cross section. However, the plotted pulse duration is the lower limit and does not necessarily represent the pulse duration after amplification.

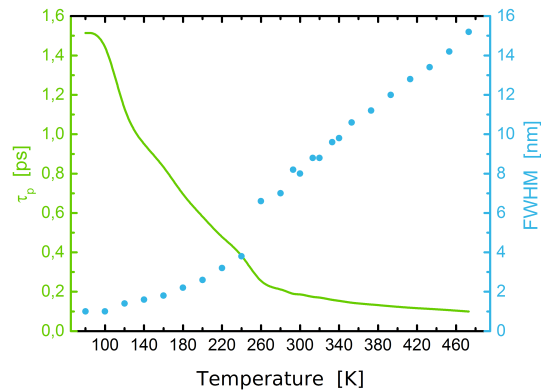


Figure 3.7: FWHM of the emission cross section (blue) and the corresponding pulse duration (green) for different temperatures of Yb:YAG. The pulse duration is calculated under assumption of Gaussian shaped spectrum with the same FWHM as the emission cross section. However, the plotted pulse duration is the lower limit and does not necessarily represent the pulse duration after amplification.

3.4 Summary

In summary, the spectral properties of Yb:YAG allow for efficient pumping at the absorption peak around 940 nm with conventional, not wavelength-stabilized diodes and to amplify a bandwidth necessary for the generation of <1 ps pulses. The amplification performance can be improved by cooling down the laser crystal at the expense of longer pulse durations. According to Figure 3.6 and Figure 3.7, a temperature of 260 K seems to be a suitable working point. However, this would demand elaborate cooling strategies. Therefore, the first amplification experiments will be performed at room temperature.

CHIRPED PULSE AMPLIFICATION

As mentioned in the introduction, the demonstration of chirped-pulse amplification for optical pulses by *D.Strickland* and *G.Mourou* in 1985 [2] was the breakthrough in order to generate final pulse powers normally exceeding the damage threshold of the optics and laser material. The basic idea of this principle is the extension of the pulse duration by introducing a frequency-dependent delay (called chirp) and hence reducing the pulse intensity of the stretched pulse. The pulse can then be amplified, as explained in Chapter 2, to the critical intensity again and subsequently the introduced chirp is removed. A scheme of the CPA principle is shown in Figure 4.1.

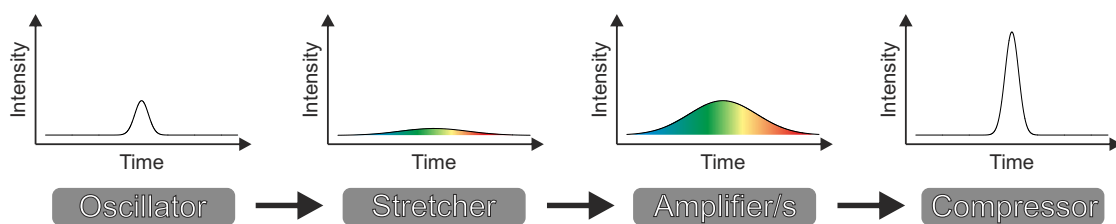


Figure 4.1: Scheme of the CPA principle. The short pulse generated in the oscillator is temporally stretched by introducing a frequency-dependent delay (called chirp) when traversing the stretcher device. Thus, the pulse intensity is lowered and the pulse can be amplified to the critical intensity again. At the end, the chirp of the pulse is removed with a compressor.

In the following, the generation of ultrashort pulses and their description as well as typical sources of dispersion utilized in CPA chains are discussed.

4.1 Generation and description of ultrashort optical pulses

4.1.1 Generation of ultrashort optical pulses

Ultrashort optical pulses are generated in a laser oscillator using mode-locking technology [27].

In a laser-cavity consisting of an active medium between two mirrors with a distance L , q stable longitudinal modes ν_q can arise:

$$\nu_q = q \frac{c}{2L} \quad (4.1)$$

The resulting electric field at a certain point in space can be described as the superposition of the individual monochromatic waves [30] using $\omega_q = 2\pi\nu_q$:

$$E(t) = \sum_{q=0}^{Q-1} E_A(\omega_q) \cos(\omega_q t + \varphi(\omega_q)) \quad (4.2)$$

Q is the total number of oscillating modes, $E_A(\omega_q)$ the amplitude and $\varphi(\omega_q)$ the phase offset of the q th mode. Normally, $\varphi(\omega_q)$ is random, but if one is able to fix the phase offset such that $\varphi(\omega_q) = \text{const.} \forall q$, all oscillations will interfere constructively at a certain instant in time.

The technique to fix the phase offset is called mode-locking and can be realized with different approaches [14]. Nowadays, the shortest pulses out of a laser oscillator are generated utilizing Ti:sapphire as laser medium. Pulse duration below 10 fs are state of the art [46].

4.1.2 Description of ultrashort optical pulses [47]

As mentioned above, short pulses can be described as a superposition of individual monochromatic waves. Mathematically more precise, the infinite sum, i.e. the integral, describes a single pulse. Using the complex representation of the cosine one derives:

$$\tilde{E}(t) = \frac{1}{\sqrt{2\pi}} \int_{-\infty}^{+\infty} E_A(\omega) e^{-i(\omega t + \varphi(\omega))} d\omega \quad (4.3)$$

This corresponds to a *Fourier* transformation:

$$\tilde{E}(t) = \mathcal{FT}[\tilde{E}(\omega)] \text{ with } \tilde{E}(\omega) = E_A(\omega) e^{-i\varphi(\omega)} \quad (4.4)$$

To obtain the real part of the temporal electric field one has to add its complex conjugate:

$$E(t) = \frac{1}{2} [\tilde{E}(t) \cdot e^{i\omega t} + \tilde{E}^*(t) \cdot e^{-i\omega t}] \quad (4.5)$$

From Equation 4.3 one can obtain that the pulse duration changes if $E_A(\omega)$ or/and $\varphi(\omega)$ are altered. $E_A(\omega) = \sqrt{I(\omega)}$ and therefore can be derived from the measurable spectrum $I(\omega)$. $\varphi(\omega)$ can be expressed using the dispersion relation:

$$\varphi(\omega) = k(\omega) \cdot z = \frac{\omega}{c} \cdot n(\omega) \cdot z \quad (4.6)$$

So, if an ultrashort pulse transverses a medium which either influences $E_A(\omega)$, e.g. by absorption or amplification, or if the medium exhibits an not constant $n(\omega)$ within the spectral bandwidth of the pulse, the pulse duration is changed. Furthermore, the pulse duration can be changed by optical setups which introduce a frequency-dependent optical path $z(\omega)$.

To compare the influence of different optical setups on the pulse duration its is beneficial to rewrite the spectral phase $\varphi(\omega)$ in a *Taylor expansion* around ω_0 :

$$\varphi(\omega) = \sum_0^{\infty} \frac{\varphi^{(n)}(\omega_0)}{n!} \cdot (\omega - \omega_0)^n \quad \text{with} \quad \varphi^{(n)}(\omega_0) = \left. \frac{\partial^n \varphi(\omega)}{\partial \omega^n} \right|_{\omega_0} \quad (4.7)$$

$$\varphi(\omega) = \varphi|_{\omega_0} + \varphi'|_{\omega_0}(\omega - \omega_0) + \frac{1}{2}\varphi''|_{\omega_0}(\omega - \omega_0)^2 + \frac{1}{6}\varphi'''|_{\omega_0}(\omega - \omega_0)^3 + \dots \quad (4.8)$$

The zeroth-order coefficient describes the offset between the oscillations of the carrier frequency ω_0 and the envelope of the electric field. It is called carrier-envelope phase (CEO). The first order spectral phase term is the group delay (GD) describing the translation of the envelope in the time-domain. Starting from the second order phase term on, the group delay dispersion (GDD), the temporal structure of the electric field is influenced. Hereby, all even phase terms lead to a symmetric broadening of the temporal shape while the odd phase terms create pre and post pulses. Analogously, these phase terms are denoted third-order dispersion (TOD) and fourth-order dispersion (FOD).

From the equations presented above one obtains shortest pulse durations if $d\varphi/d\omega = \text{const.}$ In this case the pulse duration is only determined by the pulse spectrum. One can derive the so-called *Time-Bandwidth* product [27]:

$$\Delta\nu \times \Delta\tau \geq K \quad (4.9)$$

Here, $\Delta\nu$ represents the FWHM of the frequency spectrum of the pulse and $\Delta\tau$ the FWHM of the temporal pulse shape duration. K is a constant given by the shape of the frequency spectrum. A prominent example are *Gaussian*-shaped spectra which lead to a *Gaussian* temporal pulse shape. In this case $K=0.44$. An overview of K -factors for a variety of spectral shapes can be found in [27]. However, if the real spectrum can not be approximated with a generic shape one has to perform a numerical *Fourier* transformation to calculate the temporal pulse shape.

4.2 Sources of dispersion [27]

As mentioned above the pulse duration can be altered by changing the spectral phase $\varphi(\omega)$. This is the basic principle of CPA. So, in order to extend the pulse duration one has to set up an optical device which introduces $n(\omega)$ or $z(\omega)$ or both. After the amplification, the pulse has to traverse a setup which introduces exact the opposite dispersion in order to restore the original pulse duration. Typical methods/setup to generate dispersion are given in the following listing:

- **Material:** changes the spectral phase $\varphi(\omega)$ by material dispersion $n(\omega)$
- **Gratings:** changes the spectral phase $\varphi(\omega)$ by angular dispersion $z(\omega)$
- **Prism:** material dispersion $n(\omega)$ and angular dispersion $z(\omega)$
- **Grism:** a combination of a grating and a prism
- **Chirped mirror:** a mirror based on a multilayer dielectric structure which introduces different optical path lengths via its wavelength-selective reflectivity in different depths of the coating

In the following, material dispersion and the dispersion of a stretcher/compressor setup are explained more detailed since they are the main sources of dispersion in the PFS pump laser.

4.2.1 Dispersion introduced by a transparent medium

If one considers a optical pulse propagating through a linear, absorption-free medium of the length L and the refractive index $n(\omega)$ one can write:

$$\tilde{E}(z_0 + L, \omega) = \tilde{E}(z_0, \omega) e^{-i\varphi_L(\omega)} \quad (4.10)$$

The spectral transfer function then reads as:

$$\varphi_L(\omega) = k(\omega) L = \frac{L}{c} \omega n(\omega) \quad (4.11)$$

As explained before, only the phase terms higher then the first order will lead to a change of the temporal shape. Exemplary, only the GDD will be discussed:

$$\begin{aligned} \text{GDD} &= \varphi_L'' = \frac{d^2\varphi_L}{d\omega^2} = \frac{L}{c} \left(2 \frac{dn}{d\omega} + \omega \frac{d^2n}{d\omega^2} \right) \\ &= \frac{\lambda^3 L}{2\pi c^2} \frac{d^2n}{d\lambda^2} \end{aligned} \quad (4.12)$$

4.2.2 Dispersion introduced by grating arrangements

High-energy laser pulses can only be compressed using reflection gratings since the compressed pulse powers, as explained before, trigger non-linear effects in material or exceed the LIDT. So, commonly high-energy CPA laser systems are based on a matched pair of a reflection-grating stretcher and a reflection-grating compressor.

A short pulse hitting a grating will be decomposed after reflection into the first order [27]:

$$\sin(\alpha) + \sin(\beta) = N\lambda \quad (4.13)$$

Here, α is the angle of incidence and β the angle of the reflected beam. N denotes the line density of the grating. First ideas to utilize grating arrangements to change the spectral phase of a pulse were presented by *E. Treacy* in 1969 [48]. He proposed an arrangement of two gratings and an end mirror to introduce negative dispersion. The beam is dispersed at the first grating and a second, parallel grating is used to recollimate the beam. The end mirror reverses the beam path. A scheme of this arrangement is show on the right side of Figure 4.2. The dispersion coefficients of such an arrangement can be calculated to [9]:

$$GDD = \frac{-2D \lambda_0^3 N^2}{2\pi c^2 \cos^2 \beta_0} \quad (4.14)$$

$$TOD = \frac{6D \lambda_0^4 N^2}{4\pi^2 c^3 \cos^2 \beta_0} \left(1 + \frac{\lambda_0 N \sin \beta_0}{\cos^2 \beta_0} \right) \quad (4.15)$$

$$FOD = \frac{-6D \lambda_0^5 N^2}{8\pi^3 c^4 \cos^2 \beta_0} \left[4 \left(1 + \frac{\lambda_0 N \sin \beta_0}{\cos^2 \beta_0} \right)^2 + \left(\frac{\lambda_0 N}{\cos^2 \beta_0} \right)^2 \right] \quad (4.16)$$

where λ_0 denotes the center wavelength and β_0 the corresponding angle of refraction. The grating separation is D . An arrangement like that is called compressor. A sketch of a compressor is shown on the right side of Figure 4.2. As mentioned, its counterpart is the stretcher. A *Martinez*-type stretcher [49] is shown on the left side of Figure 4.2.

As Figure 4.2 depicts, a stretcher and compressor act like a pair. If set up correctly, the chirp introduced by the stretcher is completely compensated by the compressor.

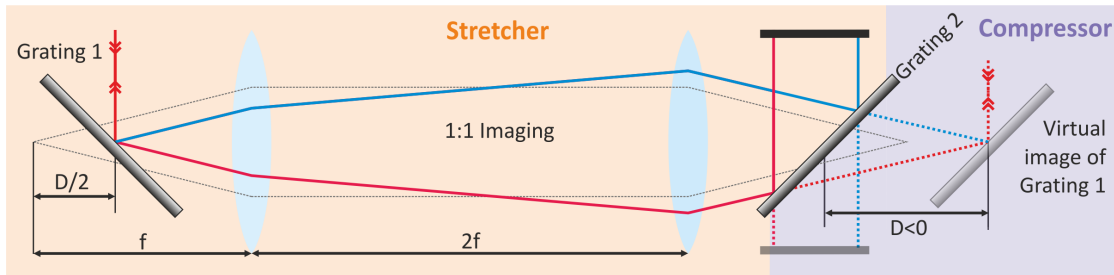


Figure 4.2: Scheme of a stretcher-compressor arrangement. On the left-hand side a stretcher in the *Martinez* configuration is depicted and on the right-hand side the companion compressor in *Treacy* configuration. If set up correctly, the chirp introduced by the stretcher is completely compensated by the compressor. *Illustration taken from [9], with kind permission.*

In a real CPA system, additional material dispersion, e.g. by the laser crystal, is introduced which can be compensated to some extent by a slight mismatch between the stretcher and the compressor setup. However, the more convenient tool is a *Dazzler* (FASTLITE) [50] - an acousto-optic modulator which enables spectral phase and amplitude shaping. The latter also very important in order to counteract changes of the pulse spectrum $I(\omega)$ during amplification caused by an unequal gain distribution originating in the mostly inhomogeneous emission cross section of the laser medium, see also Chapter 5.

Part II

MODELLING

5.1 Description of the model

Based on the theoretical background in Chapter 2, a simulation for the laser pulse amplification in Yb:YAG was developed. Under the assumption that the laser pulse amplification takes place at the end of the pump pulse duration and that the laser pulse duration is much shorter than the fluorescence lifetime the model can be separated into two parts.

In the first part, the inversion population is calculated in a time-dependent way under consideration of a constant M_{ASE} , see Equation 2.29. To ensure the correct simulation of both single- and multi-pass pumping scenarios, the crystal is virtually cut into multiple layers along the pump direction and the number of necessary layers is later checked with a convergence criterion for the extractable energy. The absorption of the pump radiation is treated wavelength- and temperature-dependent. This allows to take into account measured pump spectra as well as any artificial pump spectrum. The temperature-dependent calculation accounts for the temperature-dependence of the cross sections, see Figure 3.5 a). The functional principle of the inversion simulation is depicted in Figure 5.1.

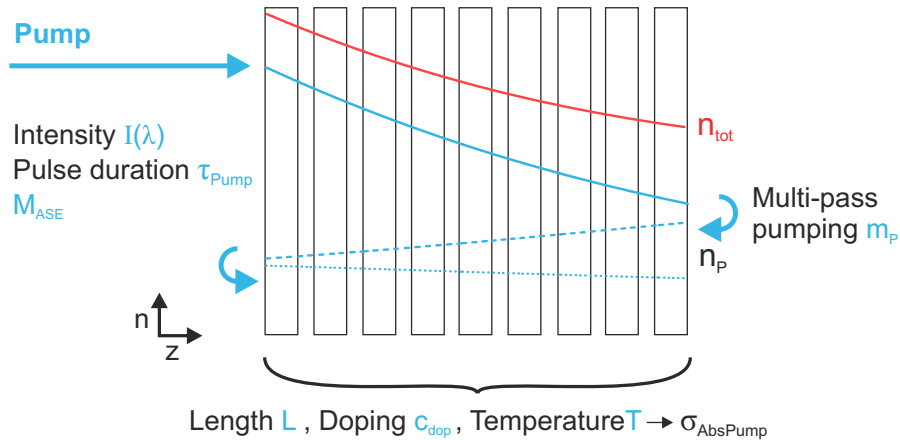


Figure 5.1: Schematic diagram of the simulation of the upper-state population. For a given spectral pump pulse intensity $I(\lambda)$, pump pulse duration t_{pump} and M_{ASE} , the resulting upper-state population density $n(z)$ is calculated with respect to the crystal length L , virtually cut into several layers, the doping concentration c_{dop} , the crystal temperature T and the number of pump passes m_p .

The result of the first part of the simulation, the layer-specific upper state population density, is carried over to the second part of the simulation, the calculation of the amplification based on the reformulated *Frantz Nodvik equation* (Equation 2.24). The same z -discretization as in the first part is used - this time assuring the precise calculation of the reabsorption of amplified radiation. Analogously, the amplification of the laser pulse is calculated in dependence of the wavelength and crystal temperature. As mentioned before, the laser pulse duration is assumed to be much shorter than the pump pulse duration. Therefore the laser pulse is not treated in a time-dependent manner. Hence, the main input parameter is the spectral energy $E_{in}(\lambda)$ along with the number of amplification passes.

The performance of the developed simulation tool will be presented in the next section by analyzing selected pump and amplification scenarios.

5.2 Selected simulation topics

5.2.1 Multi-pass pumping

Due to the quasi three-level structure of its energy levels Yb:YAG exhibits noticeable absorption in the laser wavelength range, see Figure 3.4. Hence, all non-inverted ions will reabsorb a certain part of the amplified radiation. Consequently, it is beneficial to create a high inversion level throughout the gain medium. However, the upper state population along the absorption length is governed by *Beer-Lambert's law*. Thus, the created upper state population drops exponentially with the absorption length which yields an increasing number of ground-state absorbers with crystal depth. The solution to create a high and homogeneous inversion along the gain medium length is to use a shorter gain medium and to "recycle" the not-absorbed pump radiation by applying multiple pump passes, as illustrated in Figure 5.2.

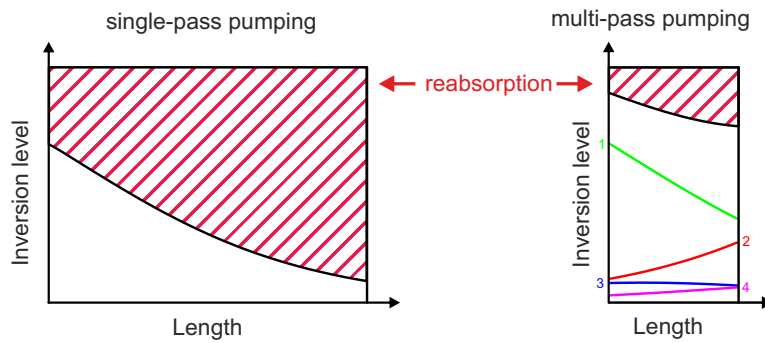


Figure 5.2: Illustration of single-pass vs. multi-pass pumping. In both cases the fraction of absorbed pump energy is the same. Applying multi-pass pumping, the number of reabsorbing ions can be reduced drastically.

The first part of the simulation code was used to evaluate multi-pass pumping. Figure 5.3 shows the findings of that calculation. The simulation parameters are summarized in the figure caption.

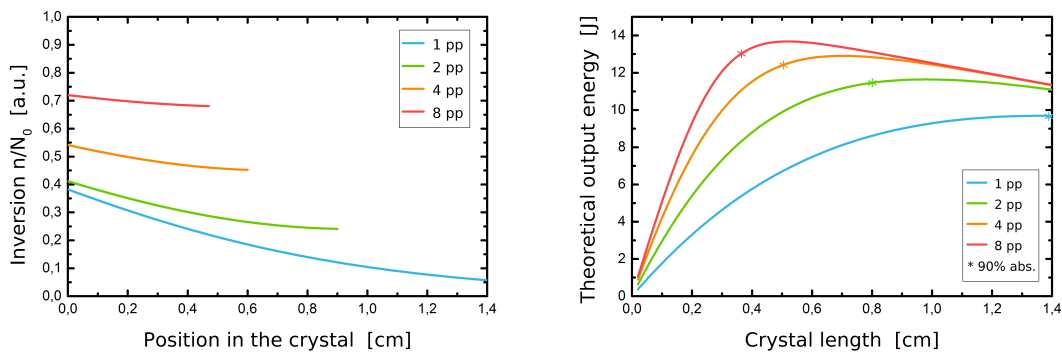


Figure 5.3: Effects of multi-pass pumping. Subfigure a) shows the enhancement of the upper state population when shortening the Yb:YAG crystal length and increasing the number of pump passes (pp). The length of the crystal was chosen such that the amount of absorbed energy is constant. The theoretical maximum output energy, considering reabsorption, in dependence of the crystal length and the number of pump passes (pp) is shown in b). The results were obtained with following simulation parameters: $c_{\text{dop}} = 2\%$, $D_{\text{Pump}} = 1 \text{ cm}$, $I_{\text{Pump}} = 25.5 \text{ kW}$, $t_{\text{Pump}} = 1 \text{ ms}$, $T = 293 \text{ K}$, $M_{\text{ASE}} = 1$

As expected, a higher and more homogeneous inversion level along the crystal length can be generated by multi-pass pumping, see Figure 5.3 a). The mean upper state population can be more than doubled when switching from single-pass to 8-pass pumping. For this calculation, the length of the crystal was chosen such that the amount of absorbed pump energy is 90% in all pump pass configurations. However, Figure 5.3 b) indicates that the ideal length for maximum theoretical output energy differs from the length of equal absorption which is again governed by the interplay between amplification and reabsorption.

For single-pass pumping the maximum energy is extracted at 90% absorbed pump power while at the maximum in the 8-pass case nearly the whole pump power is absorbed. The maximum output energy can be increased by 40% when switching from 1-pass to 8-pass pumping.

So, the benefits of multi-pass pumping are clearly evident. However, the possibility of multi-pass pumping is mainly governed by the brightness of the pump modules and space constrictions.

5.2.2 Gain narrowing

Gain narrowing describes an effect of a reduction of the spectral bandwidth during amplification. This is caused by an unequal gain distribution originating in the mostly inhomogeneous emission cross section of the laser material. For a spectrum centred at the peak of the emission cross section, the central wavelength experiences a higher gain compared to the wings of the spectrum leading to a narrower output spectrum. Furthermore, gain narrowing strongly depends on the total gain of the amplifier/s. In the case of amplifying chirped pulses gain narrowing also leads to a shortening of the stretched pulse duration which can be critical when operating close to the LIDT. The simulation takes account of gain narrowing since it calculates wavelength-dependent based on the measured cross sections [38, 39, 40]. A simulation result showing gain narrowing is depicted in Figure 5.4 a). The simulation parameters are summarized in the figure caption.

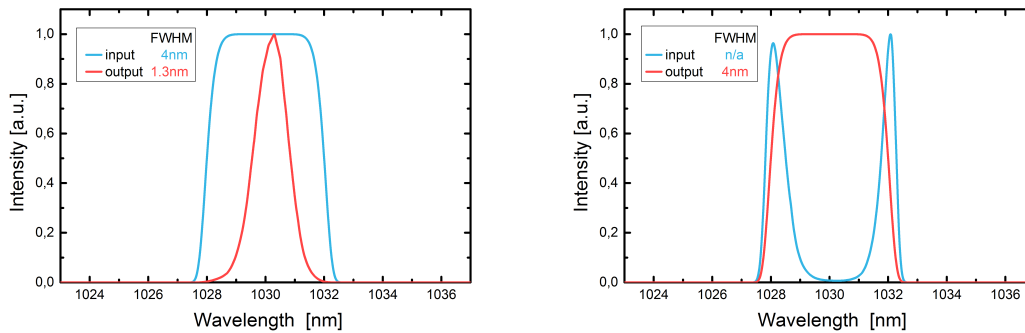


Figure 5.4: Comparison of the amplification of a spectrally unshaped input spectrum a) vs. a spectrally shaped input spectrum b). A closed-loop method was used to calculate the necessary shaping to maintain the full input bandwidth of 4 nm, shown in b). In the unshaped case the spectral bandwidth narrows down to 1.3 nm. For both simulation the total gain was set to be $\approx 10^5$. The results were obtained with following simulation parameters: $c_{\text{dop}} = 2\%$, $D_{\text{Pump}} = 1\text{ cm}$, $I_{\text{Pump}} = 25.5\text{ kW}$, $t_{\text{Pump}} = 1\text{ ms}$, $T = 293\text{ K}$, $M_{\text{ASE}} = 1$

The PFS CPA pump chain is planned to generate a total gain of $G \approx 10^5$. In this case, an unshaped input spectrum with a FWHM = 4 nm (Super-Gaussian shape) will be narrowed down to a FWHM = 1.3 nm, as shown Figure 5.4 a), which would still be sufficient for the targeted pulse duration of $\approx 1\text{ ps}$. The more severe issue in this case is the reduction of the stretched pulse duration by a factor 3, which can lead to damage of the optical components. Spectral amplitude shaping, either before or in the amplifier, is a proven method to circumvent gain narrowing. Due to its easier implementation, we opt for the first possibility. Using an acousto-optic modulator, the input spectrum is altered in a way that the spectral intensity for wavelengths with higher gain is suppressed. The effect is shown in Figure 5.4 b). A closed-loop method was used to calculate the the necessary shaping to maintain the full input bandwidth of 4 nm. S. Klingebiel did an extensive study of gain narrowing using an early version of the simulation. These results are presented in [9, 10].

As a consequence to these considerations, spectral amplitude shaping is mandatory in the PFS CPA pump chain to maintain the broadest spectral bandwidth possible during amplification. An other option to mitigate the effect of gain narrowing can be the use of Yb:glass, which exhibits a much broader amplification bandwidth compared to Yb:YAG [38], in first amplification stages where the thermal load of the crystal is low.

However, the successful suppression of gain narrowing is partially offset by the fact that at lower crystal temperatures, as desired for more efficient amplification, see Section 3.3, the gain bandwidth is reduced compared to room temperature. Although this problem has not yet been treated experimentally and theoretically in the scope of this work, it will remain the subject of further study.

5.2.3 Case study of a >1J-amplifier

In the previous sections, two features of the new simulation code were highlighted but the full capabilities of the code can best be shown in a full case study, e.g. of the >1J-amplifier for the PFS CPA pump laser.

For this amplifier stage, a pump module with a maximum pump power of 11.3 kW at a duty cycle of 1.5% generating a square pump spot of $D_{Pump} = 1$ cm is available. The pump spectrum is nearly Gaussian-shaped with a FWHM of 9 nm centred at 938 nm. A detailed description of the pump module can be found in Section 7.1. Due to space restrictions, see Section 7.3, only a double-pass configuration for the pump radiation can be realized.

The seed beam is assumed to have a circular, top-hat, beam profile with a diameter of 1 cm and a maximum seed energy of 100 mJ. A measured seed spectrum, as depicted in Figure 5.5 d), is used as an input for the simulations.

The focus of this case study lies on investigating the amplification performance of a 2%-doped crystal. This doping concentration was chosen according to the results of a transverse gain calculation, see also Section 2.5. The pump parameters given in Table 5.1 lead to a maximum transverse gain of $G_0 \approx \exp(2.2)$ in this case, which is below the threshold value for the onset of parasitic oscillation in Yb:YAG ($G_0 = \exp(2.4)$) assuming back-reflections at the YAG/Air interface.

All fixed simulation parameters are summarized in Table 5.1:

P_{Pump}	11.33 kW
t_{Pump}	1.5 ms
D_{Pump}	1 cm
Pump passes	2
Pump spectrum	Gaussian-shaped FWHM 9 nm at 938 nm
M_{ASE}	1
Yb-doping	2%
d_{Seed}	1 cm
E_{Seed}	≤ 100 mJ
Seed spectrum	measured see Figure 5.5 d)

Table 5.1: Fixed simulation parameters

At first, the ideal crystal length is determined, using the first part of the model, by calculating the stored energy (including reabsorption, calculated using only the cross sections at 1030 nm). This is done for different crystal temperatures since the desired repetition rate of 10 Hz will lead to a non-negligible temperature rise in the crystal due to the amount of pump radiation transferred into heat (e.g. quantum defect) which strongly influences amplification and reabsorption, see also Section 3.3, The result of this simulation is shown in Figure 5.5 a). It is found, that for temperatures between 300 K and 400 K a crystal length of 0.6 cm is a good compromise.

Secondly, the number of amplification passes is evaluated at 300 K under consideration of the real input spectrum. The aim is to extract as much energy as possible and to reach saturation of the amplification since that will improve the output stability of the amplifier. However, more than 20 amplification passes are hard to realize in the real setup, see also Section 7.3. The simulation revealed, as shown in Figure 5.5 b), that saturation is already observable at a little number of amplification passes. However, as expected, 20 passes are necessary to extract highest output energies. Unfortunately, this is not the maximum extractable energy as can be seen when comparing with the output energy of hypothetical 100 amplification passes.

To get a better estimation of the possible output energy, the simulation is repeated with the now fixed number of 20 amplification passes for different crystal temperatures. Assuming 300 K crystal temperature, a maximum output energy of 3.25 J is simulated. Going to 400 K, the output energy drops to 1.25 J, as depicted in Figure 5.5 c).

Lastly, the output spectrum is checked in order to see if gain narrowing is an issue. To counteract this effect, the input spectrum (Figure 5.5 d), red, FWHM = 3.8 nm) is already spectrally shaped. As depicted in Figure 5.5 d), the spectral bandwidth narrows down a FWHM of 2.6 nm if a gain of 1000 (1 J/1 mJ) is considered and to a FWHM of 3.2 nm at a gain of 30 (3 J/100 mJ) which is both uncritical for the amplification. However, it will influence the compressed pulse duration.

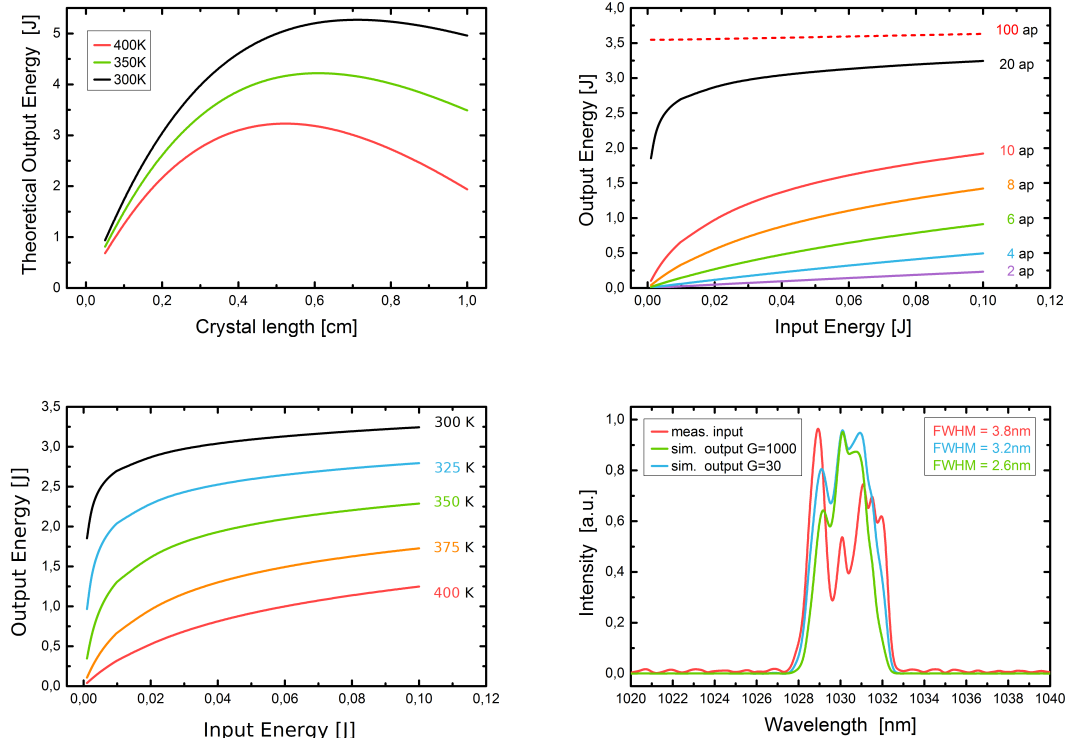


Figure 5.5: Results of a full simulation of the >1J-amplifier. For crystal temperatures between 300 K and 400 K a crystal length of 0.6 cm was found to be a good compromise, see subfigure a). The full number of 20 amplification passes (ap) is necessary in order to extract nearly the maximum extractable energy, as depicted in subfigure b). Assuming 300 K crystal temperature, a maximum output energy of 3 J was simulated. Going to 400 K the output energy drops to 1 J, see subfigure c). The spectral evolution during amplification is shown in d). In the worst case gain narrowing leads a FWHM of 2.6 nm which is uncritical.

So, the simulation of the >1J-amplifier under consideration of the fixed input parameters, summarized in Table 5.1, yields the conclusion that amplification to output energies between 3 J and 1 J, depending on the crystal temperature, should be possible in a 2%Yb-doped YAG-crystal with a length of 0.6 cm when utilizing 20 amplification passes.

5.3 Discussion of the model

On the previous pages, the capabilities of the newly developed simulation of laser pulse amplification in Yb:YAG were demonstrated. Further, not presented, simulations support the importance of the wavelength- and temperature-dependent calculation. As shown e.g. gain-narrowing and the temperature rise through pumping are not negligible and therefore have to be taken into account in a simulation.

Undoubtedly, the assumption of flat-top beam profiles and of a constant M_{ASE} is open to questions. In principle it is possible to expand the simulation to a 2-dim. grid allowing to take real beam profiles into account. However, the improvement in accuracy in this case is negligible compared to the much longer calculation time. For best accuracy, the ASE has to be treated like the amplification of the pulses itself, making a fully ray-traced, time-dependent model of the pumping necessary which would be a topic for a future thesis in its own right.

At the end, the accuracy of a simulation has to be verified by benchmarking with measurements. In this thesis this will be done in Chapter 8 and Chapter 9 where the developed simulation is used for a regression analysis of the measured gain curves to evaluate M_{ASE} and crystal temperature for different Yb:YAG crystals.

Further simulations of pulse amplification in Yb:YAG can be found in [51], [52], [53] and [54]. Unfortunately, the presented details of the simulations in all the publications are not sufficient for an objective comparison. This could be done in the future by analysing the same case with all simulation codes.

Part III

THE PFS PUMP LASER

THE PFS PUMP LASER

As described in the introduction, the amplifier development itself is not sufficient to construct a suitable pump laser for PFS, they also have to become an integral part of the CPA system.

The implementation of the PFS pump laser is one of the core tasks of the PFS project and three Ph.D. students have contributed to this system so far.

Izhar Ahmad did the initial calculations of the stretcher-compressor setup [55].

Sandro Klingebiel revised and extended these calculations and he was primarily responsible for the setup of the stretcher and compressor in the laboratory [9].

The development and implementation of the first Yb:YAG amplification stages presented in this chapter was done in close collaboration between S.Klingebiel and me.

*Due to this close collaboration, some data presented in this chapter can be found in the thesis of S.Klingebiel [9] as well. Figures and data that feature in both theses are indicated with an * in the following.*

Figure 6.1 shows a scheme of the status of the PFS pump laser in the beginning of 2011, published in [10]. This system, without its compressor, served as the "frontend" for the implementation and investigation of the 1 J-amplifier and is therefore described in detail in this chapter.

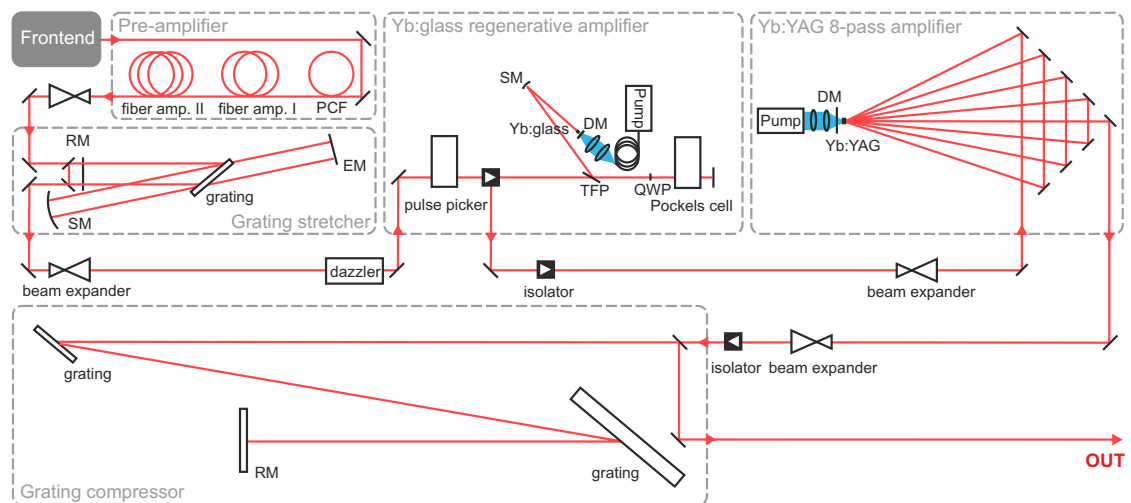


Figure 6.1: Layout of the PFS pump laser. The pulses coming from the frontend (Ti:Sa oscillator) are spectrally shifted to 1030nm in a photonic crystal fiber (PCF) and then pre-amplified in a two-stage Yb:glass fiber amplifier. The pulse duration is extended in a grating based stretcher. The spectral amplitude and phase of the stretched pulses can be shaped with an acousto-optic-modulator (*Dazzler*). After reducing the repetition rate to 10 Hz the pulses are amplified in a regenerative amplifier and in the subsequent multi-pass amplifier. Finally the pulses are compressed in a grating based compressor. (SM: spherical mirror, EM: end mirror, DM: dichroic mirror, RM: roof mirror, TFP: thin film polarizer, QWP: quarter wave plate)

6.1 Frontend and pre-amplifiers

The goal of pumping OPCPA with 1 ps-pulses requires a timing jitter between the seed and pump pulse of below 100 fs which is currently hard to achieve by electronically locking two oscillators. A better solution to achieve this accuracy is to derive the seed and pump pulses from the same source. In our case this is a commercially available Ti:sapphire oscillator (*FEMTOSOURCE™ rainbow™*, *FEMTOLASERS GmbH*) with a repetition rate of 70 MHz and an output power of ≈ 250 mW generating 10 fs pulses in the spectral range between 600 nm and 1050 nm. The output power is split in two parts. The first part (≈ 150 mW) is used to generate the OPCPA seed pulses, described [55, 56, 57], and the second part (≈ 100 mW) is used to generate the seed pulses for the pump laser.

The initial oscillator spectrum is altered via soliton self-frequency shift in a photonic crystal fiber (PCF) [58]. This procedure is necessary since the spectral intensity around 1030 nm, the central lasing wavelength of Yb:YAG, out of the oscillator is not sufficient for stable seeding of the pump laser chain. After the PCF, the spectrum is filtered by an interference filter to 1030 ± 5 nm (FWHM, gaussian shape) resulting in the reduced pulse energy of 3.4 pJ. The spectrum of the oscillator, the spectrum altered by the PCF and the filtered spectrum are plotted in Figure 6.2.

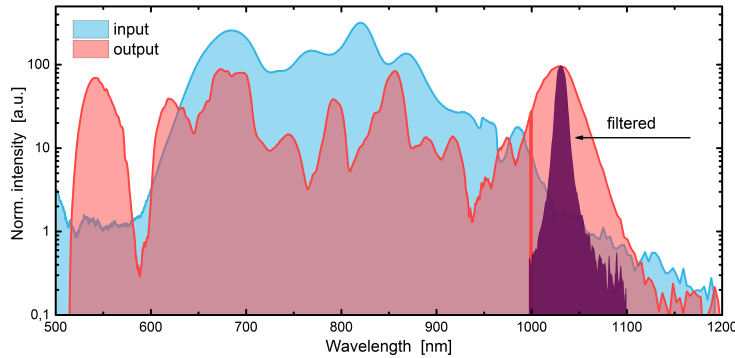


Figure 6.2: Input spectrum of the PCF (i.e. output of the oscillator, blue line), output spectrum of the PCF (red line) and filtered output spectrum (purple line) (Normalized to the energy content). *

The pre-amplifier of the PFS pump chain is a double-stage Yb-doped fiber amplifier developed by the Institute of Applied Physics (IAP) of the Friedrich-Schiller-Universität (FSU) in Jena. Both fibers are pumped at 980 nm with 180 mW and 5 W respectively boosting the output pulse energy by a factor of ≈ 4100 to 14 nJ (1 W @ 70 MHz). The measured autocorrelation trace after the second fiber amplifier is shown in Figure 6.3 a). The FWHM of this trace is 4.8 ps. Taken the measured spectrum, depicted in Figure 6.3 b), into account, a pulse duration of 3.24 ps (FWHM) is calculated [9] indicating a chirp introduced by dispersion in the fibers.

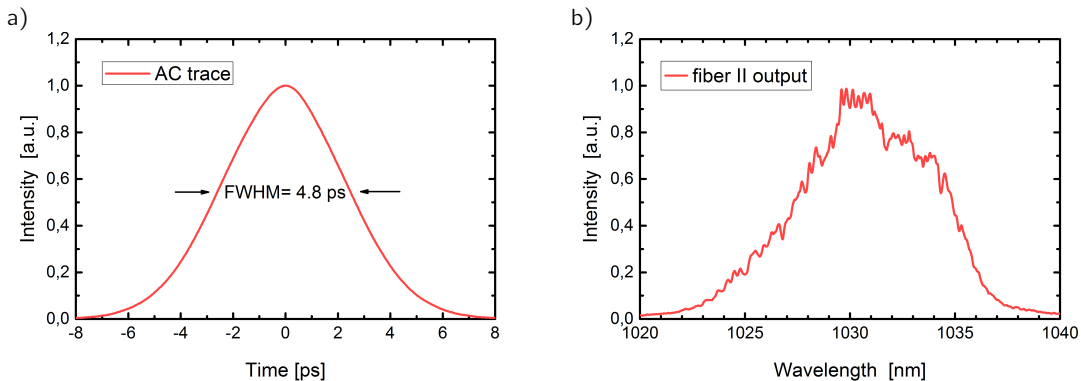


Figure 6.3: Measured autocorrelation trace a) and spectrum b) after the second fiber amplifier. The calculated pulse duration is 3.24 ps (FWHM) indicating a chirp introduced by dispersion in the fibers. *

6.2 The stretcher

The theoretical basics of a stretcher-compressor setup for a CPA-system were introduced in Chapter 4. The design of such a system is not a trivial task since many aspects have to be considered such as amplified bandwidth and the stretched pulse duration necessary for a damage-free operation. Both are linked by the stretcher/compressor dispersion and are governed by the needs imposed by the amplifier design. The amplified bandwidth is subject to the characteristics of the amplifying medium and is further limited by gain narrowing. Since the pulses are stretched, this effect will also reduce the stretched pulse duration.

For their initial calculations, I.Ahmad [59] and S.Klingeblie [60] assumed an amplified bandwidth of 1.5 nm and a target stretched pulse duration of 2 ns leading to a target GDD of $\approx 6 \times 10^8 \text{ fs}^2$. With the help of Ray-Tracing-Software (*Raytrace, Universität Erlangen & LambdaSpect for Autodesk Inventor*) it was found that a stretcher based on the Martinez design [49] would be the best solution for our purpose since it allows for a comparably small footprint.

After the revised calculations of S.Klingeblie, the setup of the stretcher was slightly adapted (see 5.3.1 in [9]). The final parameters are: one dielectric grating with a line density of 1740 lines/mm used under a angle of incidence (AOI) of $\alpha = 60^\circ$, a virtual grating separation of $D = 6 \text{ m}$ and a relay system comprising a spherical mirror with a focal length of $f = 2.7 \text{ m}$, a folding mirror and a roof mirror. Since the setup is passed two times and the separation between the grating and the folding mirror equals $D/2$ the final distance between them is $D/4 = 1.5 \text{ m}$. The resulting phase terms are: $\text{GDD} = 4.94 \times 10^8 \text{ fs}^2$, $\text{TOD} = -1.03 \times 10^{10} \text{ fs}^3$ and $\text{FOD} = 3.55 \times 10^{11} \text{ fs}^4$. The stretcher is set up in an airtight perspex box since beam pointing deviation caused by air turbulences will introduce a timing jitter [61].

A side view of the stretcher including a single-pass (4 reflections on the grating) and a top view depicting a double-pass (8 reflections on the grating) are illustrated in Figure 6.4.

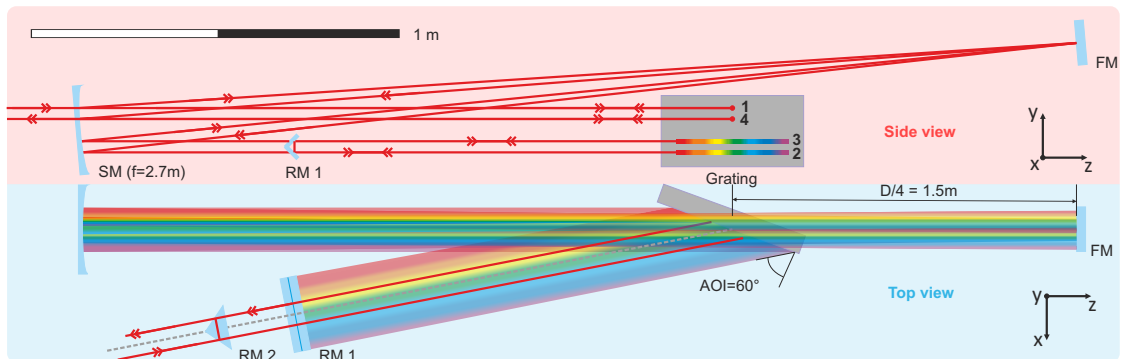


Figure 6.4: Beam path through the stretcher for a single-pass (4 reflections on the grating)(side view) and double-pass (8 reflections on the grating)(top view). The incoming beam (1) is dispersed under an AOI of $\alpha = 60^\circ$ at the dielectric grating (1740 lines/mm) and then relayed on the grating (2) via a spherical mirror (SM) and a folding mirror (FM). A roof mirror (RM 1) reverses the beam on an identical path (3)(4). Due to the double-pass utilization (RM 2) of the stretcher setup the grating separation is $D/4 = 1.5 \text{ m}$. The resulting phase terms are: $\text{GDD} = 4.94 \times 10^8 \text{ fs}^2$, $\text{TOD} = -1.03 \times 10^{10} \text{ fs}^3$ and $\text{FOD} = 3.55 \times 10^{11} \text{ fs}^4$.*

The pulse duration after double-passing the stretcher is measured to be $\approx 4 \text{ ns}$ with a transmitted bandwidth of 4.5 nm centered at 1030 nm. The transmitted spectrum, i.e. the seed spectrum for the next amplifier, is shown in Figure 6.6 a). Through the spectral cut-off and additional reflection losses the pulse energy is reduced from 14 nJ to 0.5 nJ .

After the stretcher, the beam size is expanded and the pulses pass through an acousto-optic modulator (*Dazzler, FASTLITE*). The *Dazzler* enables spectral amplitude and phase shaping which is later applied to counteract gain narrowing and for fine tuning of the compression of the pulses. Furthermore, a pulse picker, consisting of a *Pockels*-cell and a *Faraday*-isolator, is used to reduce the repetition rate of the pulses to 10 Hz before seeding the subsequent amplifier.

6.3 The regenerative amplifier

The first amplifier in the PFS CPA pump chain is a regenerative amplifier. The active medium is a $\varnothing 15 \times 8$ mm Yb:FP15-glass rod with a doping concentration of $N_{Yb} = 6 \times 10^{20} \text{ cm}^{-3}$. For this amplifier, Yb:glass is preferable since it exhibits a larger emission bandwidth compared to Yb:YAG [38] and in this case the lower emission cross section can easily be compensated by additional amplification round trips. The active medium is pumped through a dichroic mirror by a fiber-coupled diode laser (5 W peak power @ 10 Hz, 1.5 ms, 976 nm) generating a pump spot size of $100 \mu\text{m}$ ($2w$) at the position of the active medium. Further parts of the cavity are a spherical mirror ($f = 100$ mm), a thin-film polarizer (TFP) under an AOI of 65° and a plane end mirror. The combination of a quarter-wave plate (QWP) and a *Pockels*-cell, that rotates the polarization an additional quarter-wave if switched on, allows for adjusting the number of amplification round trips in the cavity. A detailed layout of the regenerative amplifier is shown in Figure 6.5.

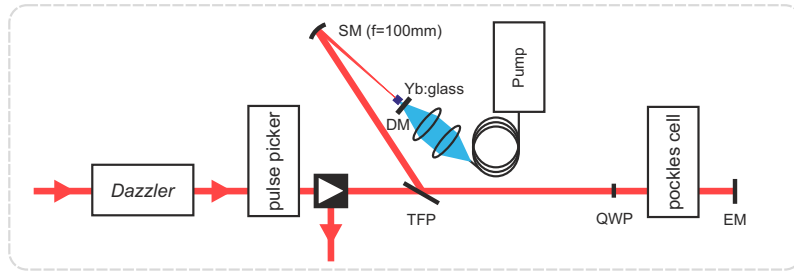


Figure 6.5: Detailed layout of the regenerative amplifier. The cavity consists of a TFP, a spherical mirror (SM, $f = 100$ mm), a dichroic mirror (DM) and an end mirror (EM). The active medium is an Yb:FP15-glass rod pumped by fiber-coupled diode laser (5 W peak power @ 10 Hz, 1.5 ms, 976 nm). The pulses are coupled into the cavity via the TFP. A QWP in combination with a *Pockels* cell allows to adjust the number of amplification round-trips in the cavity by switching the *Pockels* cell.

Experiments show that a *Pockels* cell opening time of 840 ns, corresponding to 112 round trips in the cavity, is necessary to reach a saturated pulse energy of $153 \mu\text{J}$ when seeded with the direct output of the stretcher. Figure 6.6 a) shows the measured input and output spectrum. It is obvious that the pulse undergoes a red shift. This is caused by the stretching of the pulse. Longer wavelengths travel at the front (in the time domain) of the pulse and thus experience a higher gain. As mentioned in the previous section, the pulse passes through a *Dazzler* before it is coupled into the stretcher. This device is now used to compensate the red shift. The necessary input spectrum and the resulting output spectrum are shown in Figure 6.6 b). Since the energy of the seed pulses is reduced due to the shaping, the *Pockels*-cell opening time has to be increased to 945 ns (126 round trips) to achieve a comparable saturated energy of $157 \mu\text{J}$. The saturated operation mode also leads to a good energy stability of $\sigma_E = \pm 0.5\%$.

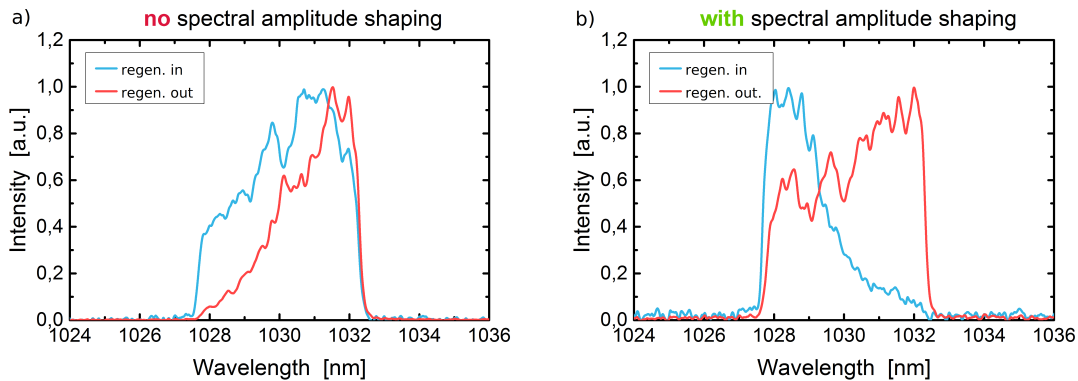


Figure 6.6: Comparison between spectrally shaped b) and unshaped a) seeding of the regenerative amplifier. In the unshaped case, the pulses experience a red shift during amplification a). Introducing a certain spectral phase with the *Dazzler* suppresses this effect b).

6.4 The 8-pass booster amplifier

The second amplifier in the PFS CPA pump chain is a multi-pass amplifier. It comprises 8 amplification passes through a diode-pumped Yb:YAG crystal. The general concept of the amplifier is illustrated in Figure 6.7. Preliminary investigations concerning this amplifier architecture were done in close collaboration with the Polaris workgroup of the Institut für Optik und Quantenelektronik of the Friedrich-Schiller-Universität in Jena and published in 2008 [62]. A detailed description of the amplifier can also be found in [10].

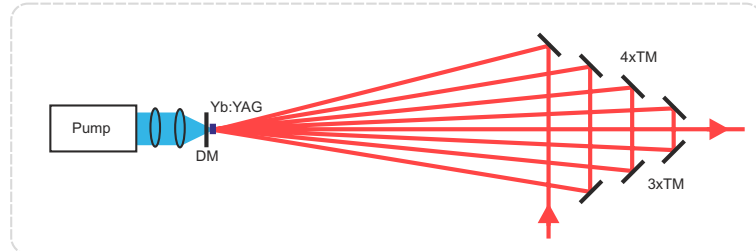


Figure 6.7: Detailed layout of the multi-pass amplifier. A $\varnothing 15 \text{ mm} \times 8 \text{ mm}$ Yb:YAG crystal with a doping concentration of 3% is pumped by a 4 kW diode-laser pump module (@ 10 Hz, 1.5 ms, 940 nm). Several turning mirrors (TM) and a dichroic (DM) mirror are used to set up 8 passes through the crystal.

The pump module for this amplifier is a commercially available laser-diode module from *JENOPTIK Laser GmbH*. It consists of one diode stack comprising 25 actively-cooled, fast-axis collimated laser-diode bars and the corresponding beam stacking optics. In total an output power of 4 kW at a wavelength of 940 nm ($\Delta\lambda = 4 \text{ nm}$) can be delivered at a duty cycle of 1.5%. An additional torical lens and one aspherical lens are used to generate the pump profile at the position of the active medium. Figure 6.8 shows a photograph of the pump beam delivery and an image of the generated pump beam profile in the crystal. The non-ideal homogeneity of the pump beam profile is caused by the internal beam-stacking in the pump module.

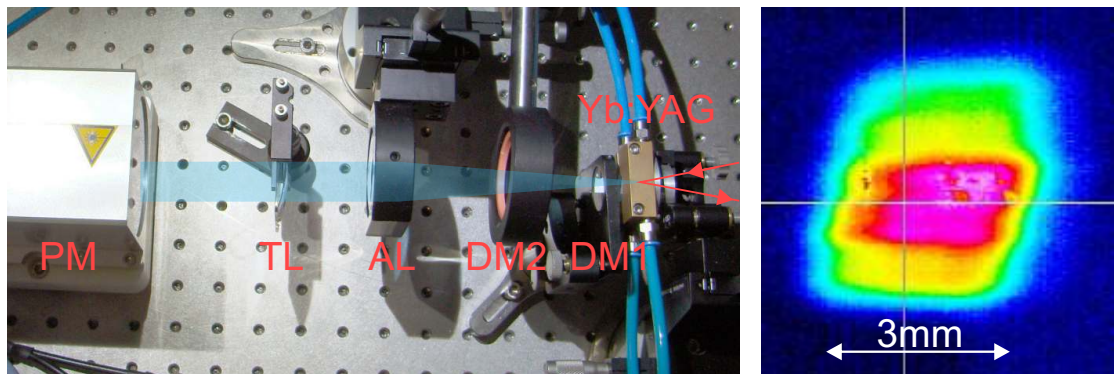


Figure 6.8: Photograph of the 4 kW pump setup and the generated pump beam profile in the crystal. The beam emitted from the pump module (PM) is further shaped by a torical lens (TL) and an aspherical lens (AL) to generate a beam profile in the crystal as shown on the right hand side. The Yb:YAG crystal is mounted in a water-cooled brass heat sink. The first dichroic mirror (DM1) is used to set up the amplification passes while the second one (DM2) is introduced for safety reasons in order to not destroy the pump module in the case DM1 gets damaged.*

Since the thermal load of the gain material in this amplifier is much higher compared to the regenerative amplifier, Yb:YAG was chosen as active medium since it exhibits a much higher thermal conductivity compared to Yb:glass. The currently used crystal has a size of $\varnothing 15 \text{ mm} \times 8 \text{ mm}$ and a doping concentration of 3 at.%. Both $\varnothing 15 \text{ mm}$ facets are AR-coated for 940 nm and 1030 nm. It is mounted in a water-cooled brass heat sink via a $100 \mu\text{m}$ thin indium foil to ensure proper heat extraction.

The non-ideal pump beam profile and non-optimized thermal management lead to strong thermal lensing of the crystal when pumped with the full pump power at 10 Hz repetition rate. The approach chosen to mitigate that effect was a reduction of the pump power to 2.5 kW. At that power level, and with the 1.5 ms pump duration chosen according to simulations, the pump energy per pulse amounts to 3.75 J. First tests showed that this pump energy is sufficient to reach the maximum pulse energy of 300 mJ - limited by the LIDT. However, the length of every single double-pass had to be adjusted individually in order to counteract the thermal lensing by exploiting diffraction and to maintain the same beam size of ≈ 4.3 mm (FWHM) in the crystal for each double pass. Unfortunately, this circumstance also fixes the pump energy to the value used during optimization.

The first test of the amplification revealed very strong gain narrowing. Without precautions the stretched pulse duration was shortened to <1 ns leading to the damage of certain optics if the pulses were amplified to pulse energies exceeding 60 mJ. The first attempt to counteract this effect was the implementation of a spatial light modulator in the fourier plane of a zero-dispersion stretcher. The input spectrum was shaped in such a way that gain narrowing is completely suppressed and output pulse energies in the range of 300 mJ are possible [10]. After the *Dazzler* arrived, it turned out to be the more convenient device to shape the spectrum of the stretched pulses. An exemplary input spectrum and the resulting output spectrum are plotted in Figure 6.9 b). The amplified bandwidth is 3.8 nm allowing for a fourier-limited pulse duration of ≈ 700 fs. Further experiments revealed that the beam profile out of the booster had to be optimized for seeding the subsequent amplification stage in order to deliver a sufficient pump profile for the OPCPA leading to a reduced maximum pulse energy of 220 ± 9 mJ. The 8-pass amplification performance for this case is shown in Figure 6.9 a). Despite the fact that the pump spot is not ideally homogeneous the amplified beam profile is very smooth as shown in Figure 6.10.

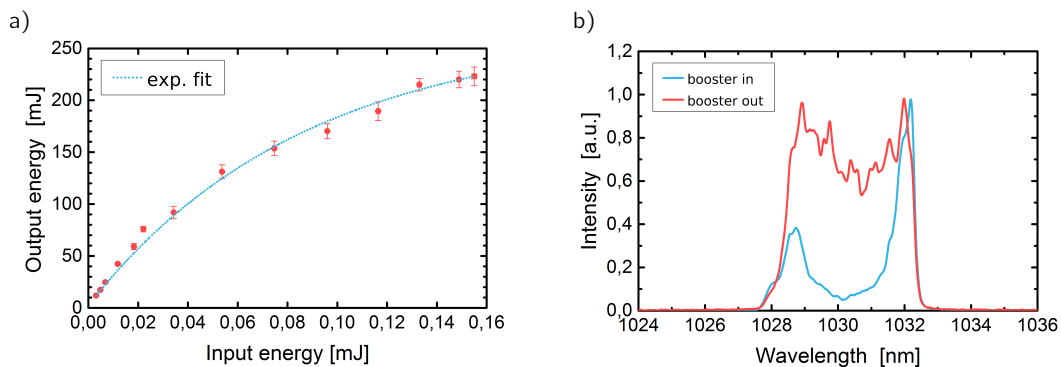


Figure 6.9: Performance of the 8-pass amplifier a) and the corresponding spectra b). A maximum output energy of 220 mJ is realized on a daily basis. The amplified bandwidth is 3.8 nm if seeded with a proper input spectrum allowing for a fourier-limited pulse duration of ≈ 720 fs.

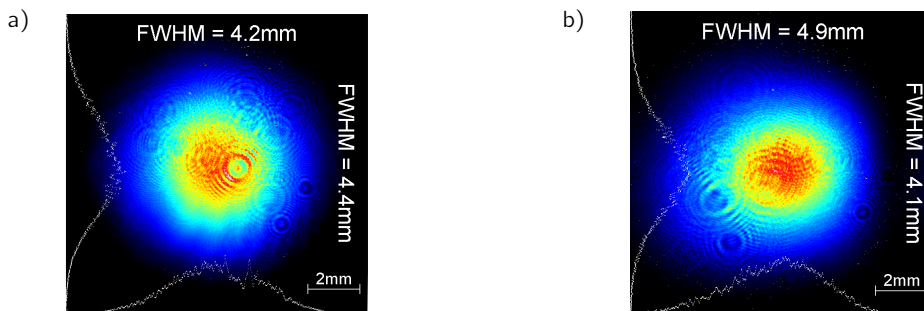


Figure 6.10: Input a) and output b) beam profile of the 8-pass amplifier. The beam out of the regenerative amplifier is enlarged to ≈ 4.3 mm (FWHM) to seed the multi-pass. After amplification the beam profile has a more elliptical shape with a mean diameter of ≈ 4.4 mm (FWHM). The fringes are introduced by the filters used to attenuate the beam.*

6.5 The grating compressor

After the pulse amplification, the chirp introduced by the stretcher has to be compensated in order to generate fourier-limited pulse durations. This is done with a compressor, introducing exactly the opposite chirp, compared to the stretcher, if set up with identical gratings, i.e the same line density, an identical AOI and the same (virtual) grating separation.

Again, first calculations were carried out by I.Ahmad [55] and revised by S.Klingebiel [9] leading to a *Treacy*-type compressor setup [48]. To fully compensate the chirp introduced by the stretcher the line density of the gratings has to be 1740 lines/mm, the AOI = 60° and the grating separation $D = 6$ m. The resulting phase terms are: $GDD = -4.94 \times 10^8 \text{ fs}^2$, $TOD = 1.03 \times 10^{10} \text{ fs}^3$ and $FOD = -3.55 \times 10^{11} \text{ fs}^4$, see Section 6.2. The assumed LIDT, including a safety margin, of the available dielectric gratings is $\approx 500 \text{ mJ/cm}^2$ (for few ps pulses). For the a final pulse energy of 10 J at 1 ps pulse duration one calculates the necessary beam diameter for a top-hat beam profile to be 5 cm. The whole compressor setup is currently being installed in a vacuum chamber for the same reason as explained in Section 6.2.

A technical drawing of the compressor including ray-tracing is shown in Figure 6.11.

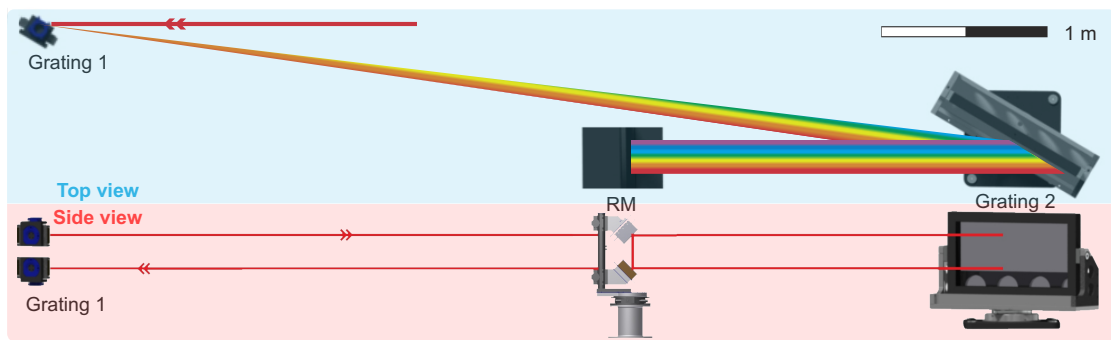


Figure 6.11: Technical drawing of the compressor. Two gratings (1740 lines/mm) under an AOI of 60° are set up with a grating separation of 6 m. A roof mirror (RM) is used to reverse the beam path. The resulting phase terms are: $GDD = -4.94 \times 10^8 \text{ fs}^2$, $TOD = 1.03 \times 10^{10} \text{ fs}^3$ and $FOD = -3.55 \times 10^{11} \text{ fs}^4$. Since no folding of the beam path is applied so far the proportions of the setup are rather large, see the printed scale. *

Material dispersion introduced after the stretcher, e.g. 100 round-trips in the 8 mm long Yb:glass rod in the regenerative amplifier, has to be compensated as well. This can be done by adjusting the grating separation. Additional higher phase terms can be compensated using the *Dazzler*. The results of *FROG* [63] measurement of a compressed pulse is shown in Figure 6.12.

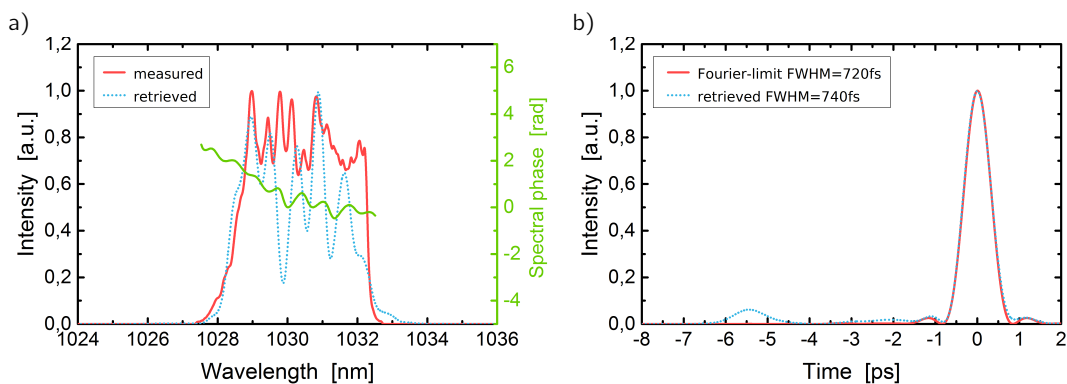


Figure 6.12: FROG evaluation of a compressed 200 mJ pulse. A good agreement between measured and retrieved spectrum was found a). The residual phase is in the range of $\Delta\varphi = 3$ rad. The corresponding pulse durations are shown in b). The compressed pulse has a pulse duration of 740 fs (FWHM) which is close to the Fourier-limit of 720 fs (FWHM). *

The optical losses introduced by the compressor setup are measured to be 24%.

6.6 Summarized key parameters

In the previous sections of Chapter 6, the individual stages of the PFS pump laser chain and their current status were described in detail. Figure 6.13 resembles Figure 6.1 now including all the key parameters of the PFS CPA pump laser system. For a quick overview all the key parameters are also summarized in Table 6.1.

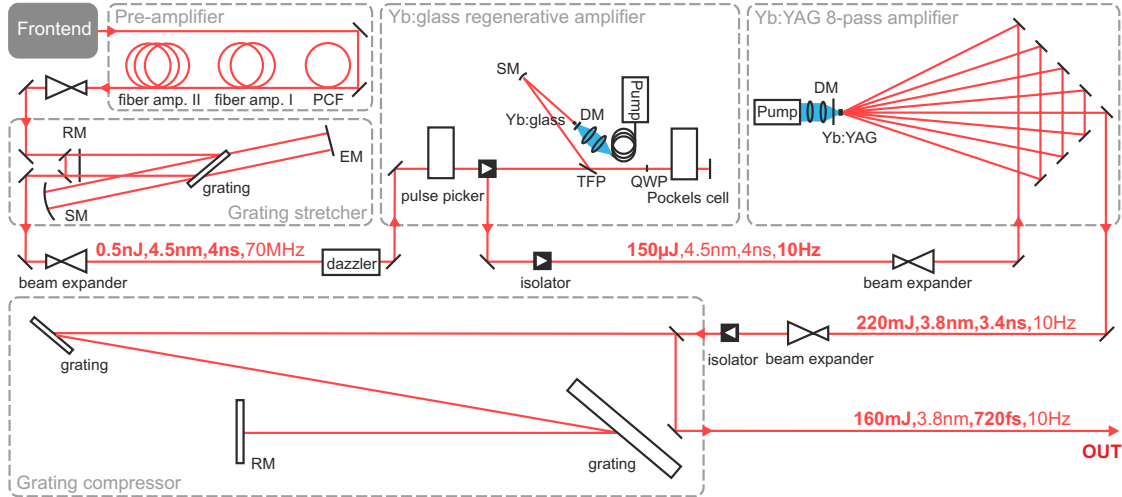


Figure 6.13: Detailed layout of the PFS pump laser including key parameters. The pulses coming from the frontend (Ti:Sa oscillator) are spectrally shifted to 1030 nm in a photonic crystal fiber (PCF) and then pre-amplified in a double stage Yb:glass fiber amplifier. A double pass through a grating stretcher expands the pulse duration. The spectral amplitude and phase of the stretched pulses can be shaped with an acousto-optic-modulator (dazzler). After reducing the repetition rate the pulses are amplified in a regenerative amplifier and in the subsequent multi-pass amplifier. Finally, the pulses are compressed in a grating based compressor. (SM: spherical mirror, EM: end mirror, DM: dichroic mirror, RM: roof mirror, TFP: thin film polarizer, QWP: quarter wave plate)

Seed	Ti:Sa oscillator + PCF	$f_{\text{rep}} = 70 \text{ MHz}$	$\lambda = 1030 \text{ nm}$ $\Delta\lambda = 10 \text{ nm}$ $E_{\text{out}} = 3.4 \text{ pJ}$
Pre amplifier	Yb-doped double stage fiber amplifier	$P_{\text{pump1}} = 180 \text{ mW (cw)}$ $P_{\text{pump2}} = 5 \text{ W (cw)}$ $f_{\text{rep}} = 70 \text{ MHz}$ $\lambda_{\text{pump}} = 980 \text{ nm}$	$E_{\text{out}} = 14 \text{ nJ}$ $\Delta\lambda = 10 \text{ nm}$ $\tau_{\text{pulse}} \approx 3.24 \text{ ps}$
Stretcher	modified <i>Martinez</i> -type	1740 lines/mm AOI = 60° D/4 = 1.5 m	$E_{\text{out}} = 0.5 \text{ nJ}$ $\Delta\lambda = 4.5 \text{ nm}$ $\tau_{\text{pulse}} \approx 4 \text{ ns}$
Amplifier 1	Yb:FP15-glass regenerative amplifier	$P_{\text{pump}} = 5 \text{ W (qcw)}$ $\lambda_{\text{pump}} = 976 \text{ nm}$ $\tau_{\text{pump}} = 1.5 \text{ ms}$ $f_{\text{rep}} = 10 \text{ Hz}$	$E_{\text{out}} = 150 \mu\text{J}$ $\Delta\lambda = 4.5 \text{ nm}$ $\tau_{\text{pulse}} \approx 4 \text{ ns}$
Amplifier 2	Yb:YAG 8-pass amplifier	$P_{\text{pump}} = 2.5 \text{ kW (qcw)}$ $\lambda_{\text{pump}} = 940 \text{ nm}$ $\tau_{\text{pump}} = 1.5 \text{ ms}$ $f_{\text{rep}} = 10 \text{ Hz}$	$E_{\text{out}} = 220 \text{ mJ}$ $\Delta\lambda = 3.8 \text{ nm}$ $\tau_{\text{pulse}} \approx 3.4 \text{ ns}$
Compressor	<i>Treacy</i> -type	1740 lines/mm AOI = 60° D = 6 m	$E_{\text{out}} = 160 \text{ mJ}$ $\Delta\lambda = 3.8 \text{ nm}$ $\tau_{\text{pulse}} = 740 \text{ fs}$

Table 6.1: Key parameters of the PFS CPA pump laser system

Part IV

CONCEPT OF THE 1 J-AMPLIFIER

CONCEPT OF THE 1 J-AMPLIFIER

As mentioned before, the so far installed PFS pump laser system, as described in the previous chapter, serves as the "frontend" for the main objective of this dissertation - the development and implementation of a scalable amplifier boosting the pulse energy to the 1 J-range.

However, the main problem encountered during installation of the 300 mJ-amplifier is thermal lensing. The aberrations due to the non-uniform pump beam profile, see Figure 6.8, and the non-ideal cooling of the Yb:YAG crystal had to be mitigated via beam shaping by diffraction in each of the passes. This strategy does not scale with changing the beam diameter and thus this architecture remains a one-off prototype.

For the 1 J-amplifier, new schemes for pumping and cooling of the Yb:YAG crystal have to be realized to minimize thermal lensing and to allow for a reproducible operation and scalability.

7.1 Pump module for the 1 J-amplifier

The laser-diode pump module available for the 1 J-amplifier was purchased in 2006 from *Jenoptik Laserdiode GmbH* (now *JENOPTIK Laser GmbH*) and intentionally planned for and tested in a first amplifier scheme [64, 65].

The module consists in total of 16 laser-diode stacks. Each stack comprises 4 horizontally-stacked, fast-axis-collimated laser-diode bars which are passively cooled via a copper heat sink, as exemplary shown in Figure 7.1 a). These stacks are assembled in 2 polarisation-coupled branches each consisting of 2x4 waveguide-coupled stacks as shown in Figure 7.1 b). Each of the four sub-arms (4 waveguide-coupled stacks) is one unit in terms of cooling and power supply and can be controlled individually.

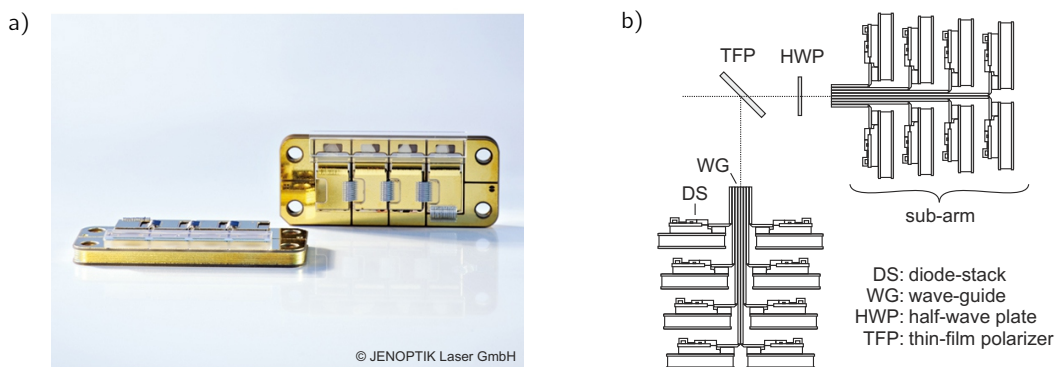


Figure 7.1: Examples of 4 horizontally-stacked, fast-axis collimated laser-diode bars a) and the actual arrangement of 16 such stacks in the pump module b). With kind permission of *JENOPTIK Laser GmbH* a) and M. Siebold b).

This combination of the 16 laser-diode stacks leads to an output beam aperture of $12 \times 52 \text{ mm}^2$ with a slow-axis divergence of 10° and a nearly collimated fast-axis. The gross output power of each bar is 250 W (@300 A, 10 Hz) giving a total gross output power of 16 kW.

In the first amplifier design [64, 65] the crystal was mounted and cooled via its two largest crystal faces and pumped transversely. However, the internal wave-guide coupling together with the transverse pumping lead to a striped intensity profile in laser direction deteriorating the beam profile strongly during amplification. Furthermore, the cooling concept proved to be not sufficient for long-term 10 Hz operation.

To improve the cooling, we decided to utilize the active-mirror concept, explained in detail in the next chapter. Therefore, the pump profile of the existing pump module had to be adapted and improved. This is achieved by the use of micro-lens beam-homogenizers recently available with very high throughputs. This homogenization method is based on the *Köhler-integrator* principle [66], shown in Figure 7.2 a), where two micro-lens arrays and one lens are used to generate a homogenized beam image. The image size is given by the pitch of the micro lenses, their focal length and the focal length of the imaging lens. For a certain pump spot size these parameters have to be adapted to the initial divergence of the pump module.

To homogenize both slow- and fast-axis of the pump module, arrays from *Süss MicroOptics* were purchased. These homogenizers have the benefit that both cylindrical arrays are fabricated into the front- and back-side of the same substrate which simplifies the alignment significantly. The radius of curvature (ROC) of the micro lenses is $750\ \mu\text{m}$ and their pitch is $250\ \mu\text{m}$. With an additional aspherical lens ($f_{FL} = 60\ \text{mm}$) a flat-top $10\times 10\ \text{mm}^2$ (FWHM) pump profile, shown in Figure 7.2 b), was realized.

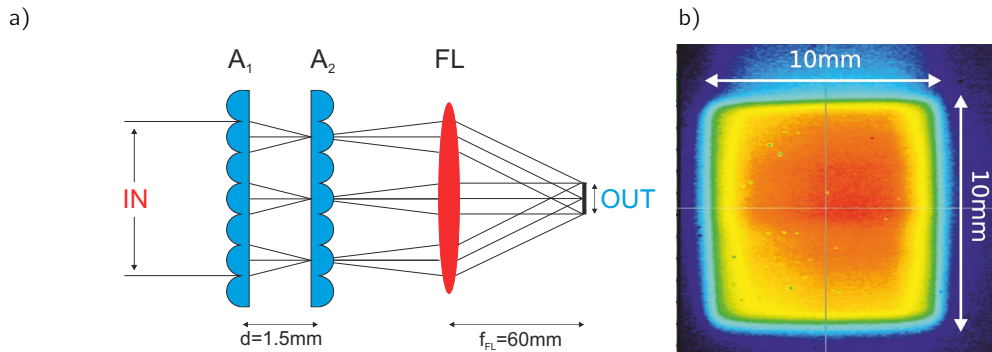


Figure 7.2: Scheme of the homogenizing setup a) and pump beam profile b) of the 13 kW pump module. In both slow- and fast-axis, two micro-lens arrays (A_1 , A_2 , actually both on the same substrate) together with an aspherical lens are used to generate the flat-top pump profile shown in b).

Due to the internal coupling (polarization and wave-guide) and the homogenizing elements additional optical losses are introduced reducing the overall available pump power to a maximum of 13.3 kW. The power-current-dependence is shown in Figure 7.3 a). Since the peak emission wavelength of a not stabilized laser-diode stack in qcw operation depends on the temperature of the heat sink (typically: $\Delta\lambda = 0.3\ \text{nm/K}$) the possibility of individually cooling the 4 sub-arms allows to match the spectrum of the pump module perfectly to the absorption spectrum of Yb:YAG as depicted in Figure 7.3 b).

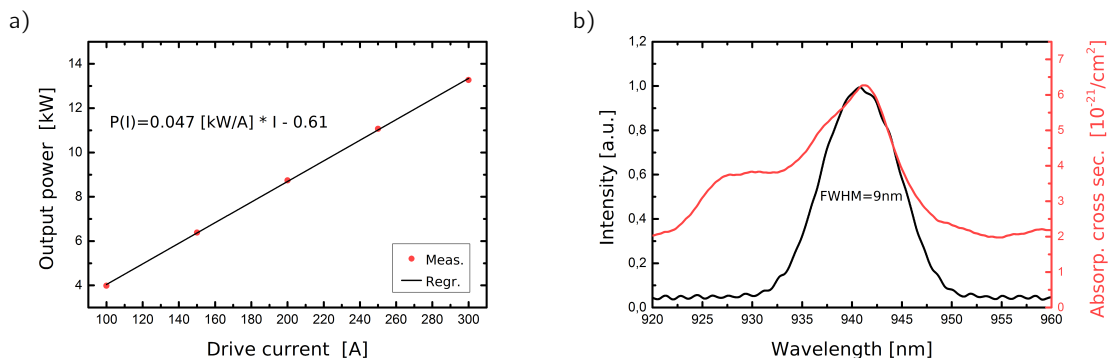


Figure 7.3: Pump power of the 13 kW module in dependence of the drive current (a) and the corresponding output spectrum (b) in comparison to the absorption cross section of Yb:YAG (red) at room temperature.

7.2 Active-mirror Yb:YAG crystal assemblies

In the last decade the thin-disk laser concept [14, 67] proved its capabilities for effective cooling of the Yb:YAG as evidenced by the demonstration of several kW of output power in cw-operation. However, thin-disks require a high doping concentration which is counterproductive if large beam diameters are required. In fact, the high doping concentration facilitates parasitic effects, e.g. transverse lasing which arises if the gain for spontaneous emitted photons in transverse direction exceeds the reflection losses at the edge of the laser material and thus a positive feedback is generated, as explained in Section 2.5.

An alternative is to use thicker disks featuring lower doping concentrations also known as the active-mirror concept [11, 22]. In this approach, analogously to the thin-disk concept, the crystal is cooled via its back surface. Due to the fact that the thickness of the crystal is much smaller than its diameter, the heat transfer in the longitudinal direction dominates, hence minimizing the thermal lens.

The cooling of the crystal can either be achieved by direct water-cooling of the back surface or by bonding the crystal onto a cooled heat sink. Therefore, the back surface of the crystal has to be coated with a high reflection coating for both pump and seed radiation and thus the crystal is inherently double passed by the pump radiation. Figure 7.4 illustrates the thick-disk/active-mirror concept.

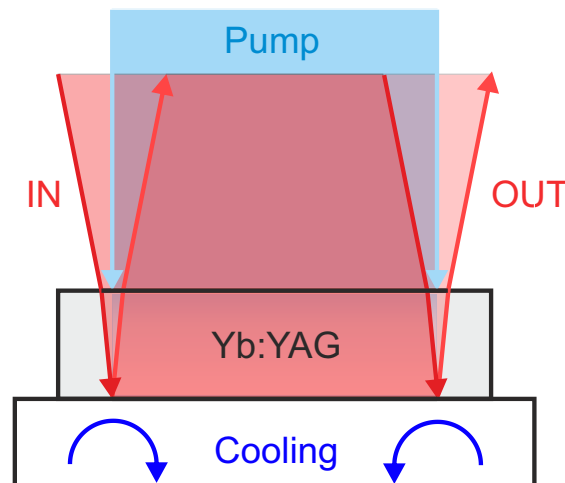


Figure 7.4: Scheme of the thick-disk/active-mirror concept. A thick crystal is cooled via its large back surface. The back surface is either directly water-cooled or the crystal is bonded onto a heat sink. The back surface of the crystal has to be coated with a high reflection coating for both pump and seed radiation.

As mentioned above, the backside of the crystal can either be directly water-cooled or be bonded onto a special heat sink. Direct water-cooling, on the one hand, allows high heat dissipation but the high water pressure necessary may lead to deformation of the Yb:YAG crystal. This deformation should be less in the case of bonding but very flat heat sinks are required and the bonding layer should be very thin in order to allow good thermal transfer.

Nonetheless, bonding crystals is not a trivial task and not all bonding technologies can be applied in our case or are readily available. A compilation of bonding technologies and their pros and cons is given on the next page.

Compilation of bonding technologies

- Soldering:
 - + standard technology used for thin-disk lasers
 - special coating necessary which limits the damage threshold (LIDT < 1 J/cm² @ 10 ns)
- Chemical bonding:
 - + ultra-thin bonding layers
 - custom-made
 - expensive
 - currently not ready for production
- Glueing:
 - + no special precautions for crystal and heat sink
 - + cost-efficient
 - + can be done "in-house"
 - technology has to be developed
 - poor thermal conductivity of the glue layer

The decision was made to try the latter approach because the "in-house" and cost-efficient realisation were promising to glue a large number of crystals in a short time. Nevertheless the development of the gluing technology was a challenging task.

Several glues and heat sinks were tested in order to find the ideal approach. At the end, three different types of glues, in the following named glue #1,#2,#3 were used to bond the crystals onto heat sinks which are either plated with nickel or gold. It has to be mentioned that glue #2 is unknown since this crystal was not glued by ourselves. So, the chemical composition and thus the thermal properties of glue #2 can differ from the others.

While glueing the crystals, the occurrence of interference fringes between the back site of the crystal and the heat sink could be observed under illumination with white light, as shown in Figure 7.5. This leads to the conclusion that the glue-layer thickness must be on the order of several μm . Furthermore, it was possible to minimize the number of observed fringes to $m < 3$ indicating a residual layer thickness deviation in the range of 1 μm .



Figure 7.5: Example of an Yb:YAG crystal glued on a gold-plated heat sink. At white light, an interference pattern in the thin glue layer between crystal and heat sink is observable leading to the conclusion that the glue layer must be in the order of several μm .

As explained in Section 2.5, the threshold for the onset of parasitic oscillations for the 1 J-stage is expected for doping concentration $>2\%$. Unfortunately, since the depopulation of the upper laser level through parasitic lasing is not covered by the developed simulation the output energy in case of a higher doping concentration can not be calculated precisely. It is expected to be lower compared to the 2% case but maybe it is sufficient to reach an output energy >1 J as well.

From particular interest is the effect of the lower thermal load when using thinner crystals. The lower crystal temperature in that case should increase the amplification performance. However, it will also enhance the parasitic effects.

An interesting approach to enhance the absorption of the ASE and thus suppress parasitic oscillations was shown by *Yagi et al.* [68] by using a Cr^{4+} co-doped edge cladding. Unfortunately, this approach was not at our disposal by that time. That's why we decided to investigate the influence of the size of the unpumped area surrounding the pump spot since the ground-state absorption in the unpumped area, caused by the quasi-three-level nature of Yb:YAG, also acts as an absorbing edge cladding.

Therefore, several Yb:YAG crystals differing in doping concentration, thickness and size were purchased in order to investigate the impact of the parasitic oscillations. The crystals were glued, as briefly explained before, on different heat sinks, forming six different crystal/sink combinations, as listed in Table 7.1 below.

crystal	heat sink coating	glue	abbreviation
$2\%_{\text{dop.}} \times 6\text{mm} \times 20 \times 20\text{mm}^2$	Au	#1	$2\% \times 6 \times 20$ Au1
$2\%_{\text{dop.}} \times 6\text{mm} \times 40 \times 40\text{mm}^2$	Au	#1	$2\% \times 6 \times 40$ Au1
$6\%_{\text{dop.}} \times 3\text{mm} \times 20 \times 20\text{mm}^2$	Au	#1	$6\% \times 3 \times 20$ Au1
$6\%_{\text{dop.}} \times 3\text{mm} \times 20 \times 20\text{mm}^2$	Ni	#2	$6\% \times 3 \times 20$ Ni 2
$8\%_{\text{dop.}} \times 2\text{mm} \times 20 \times 20\text{mm}^2$	Au	#1	$8\% \times 2 \times 20$ Au1
$8\%_{\text{dop.}} \times 2\text{mm} \times 20 \times 20\text{mm}^2$	Ni	#3	$8\% \times 2 \times 20$ Ni 3

Table 7.1: Overview of the available crystals setups and their abbreviation used in the following

For illustration, the $8\% \times 2 \times 20$ Au1 crystal setup and a setup comparable to the $2\% \times 6 \times 40$ Au1 crystal setup are shown in Figure 7.6. The latter was not investigated further in the framework of this dissertation since a different heat sink was used which introduced severe wavefront aberrations.

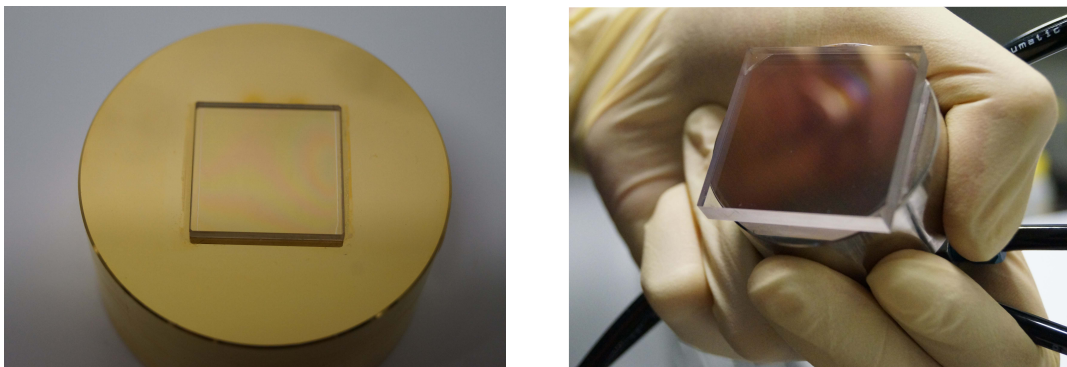


Figure 7.6: Photographs of a 8%-doped $2\text{mm} \times 20 \times 20\text{mm}^2$ Yb:YAG crystal bonded onto a gold-coated heat sink ($8\% \times 2 \times 20$ Au1)(left) and of a 2%-doped $6\text{mm} \times 40 \times 40\text{mm}^2$ crystal glued onto a nickel-plated heat sink (right). The latter heat sink lead to severe wavefront aberrations and therefore the amplification performance of this crystal assembly was not investigated further.

7.3 Relay-imaging multi-pass amplifier setup

7.3.1 Relay-imaging amplifier concepts

In combination with the active-mirror cooling concept, the improved beam profile of the pump module should help to minimize thermal lensing. Nevertheless, a means of compensating a range of possible thermal lensing has to be provided by the design of the new multi-pass amplifier. In a standard multi-pass a spherical thermal lens will lead to focussing or defocussing of the beam altering the beam size for each round trip and thus influencing the overall efficiency. As an ultimate consequence, a focusing thermal lens can lead to optical damage.

A way to circumvent this problem is relay imaging - the multi-pass is set up in such a way that in each pass the crystal plane is imaged onto itself via a $4f$ -configuration. The advantage of such an imaging approach is that regardless of thermal effects the beam size in the imaging plane stays constant - a thermal lens would just lead to different beam diameters on the imaging optics. However, it has to be checked if this is critical. Furthermore, a thermal lens can be compensated by adjusting the distance between the imaging optics. The drawbacks of an imaging amplifier are a higher complexity and the necessity for operation under vacuum conditions due to the high intensities in the intermediate foci.

An example of a double-pass relay-imaging amplifier in a $4f$ -configuration is shown in Figure 7.7. The layout was generated using *LambdaSpect* [69], a ray-tracing tool-kit for *Autodesk Inventor* [70].

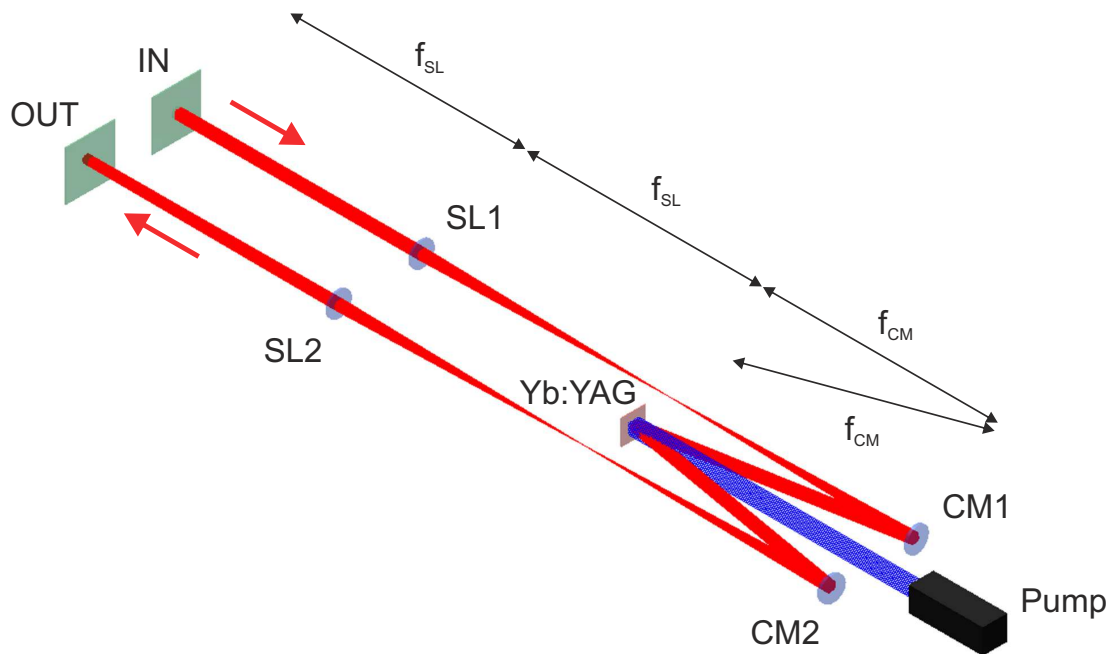


Figure 7.7: Setup of a double-pass relay-imaging amplifier in $4f$ -configuration. The input plane (IN) is imaged via a spherical lens (SL1)(f_{SL}) and a concave mirror (CM1)($f_{CM} = f_{SL}$) to the active-mirror Yb:YAG crystal which is double passed. From there it is imaged onto the output plane (OUT) via CM2 and SL2.

Alternatively, one could combine the relay imaging setup with the folded bow-tie approach to increase the number of amplification passes but this would introduce larger angles on the concave mirrors with each double-pass leading to a declining overlap between pump and seed.

So, increasing the number of amplification passes and keeping the angles on the concave mirrors small and constant for each double passes demands to use all 3 spatial dimensions. An example for a 4-pass 3D relay-imaging configuration is depicted in Figure 7.9. The double-pass setup (Figure 7.7) in the x-y plane is extended by an identical configuration in the x-z plane.

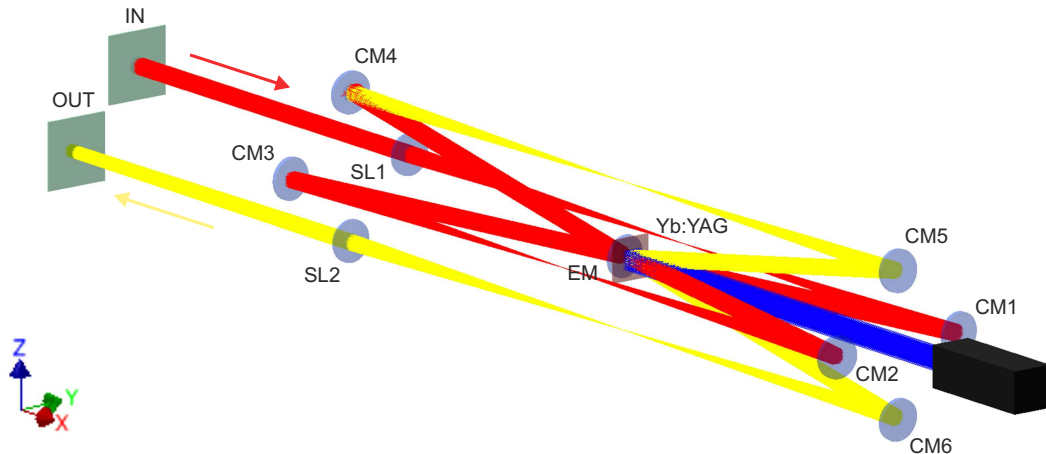


Figure 7.9: Concept of a 3D 4-pass relay-imaging amplifier. The double-pass setup in the x-y plane (red) is extended by an identical setup in the x-z plane (yellow). The folding is achieved by an additional end mirror (EM) in the image plane of Yb:YAG crystal, which is now located back-to-back to the crystal.

This 3D 4-pass relay-imaging setup can be expanded by introducing further imaging passes in different planes rotated around the x-axis. The maximum amount of possible passes then is mainly given by geometrical constraints, namely the diameter of the curved mirrors and the outer diameter of the setup. Another benefit of this 3D relay-imaging setup is its rotational symmetry which allows for the use of tubes as vacuum vessels, hence simplifying and reducing the price of the vacuum installations.

As simulated in Section 5.2.3, 20 amplification passes are needed to achieve an output energy $> 1\text{J}$. The constraints in the laboratory were an outer diameter of the vacuum tube of 320 mm and a length not exceeding 3 m. The diameter of the concave mirrors is 1". First drafts showed that 10 passes are possible in such a configuration. As explained before, this can be extended to 20 passes with a quarter-wave plate (QWP) in combination with a polarizer. Another constraint is the short working distance of the pump module which makes additional folding of the setup necessary.

The result of a conceptual design study under the above given constraints is shown in Figure 7.10 and discussed in the following.

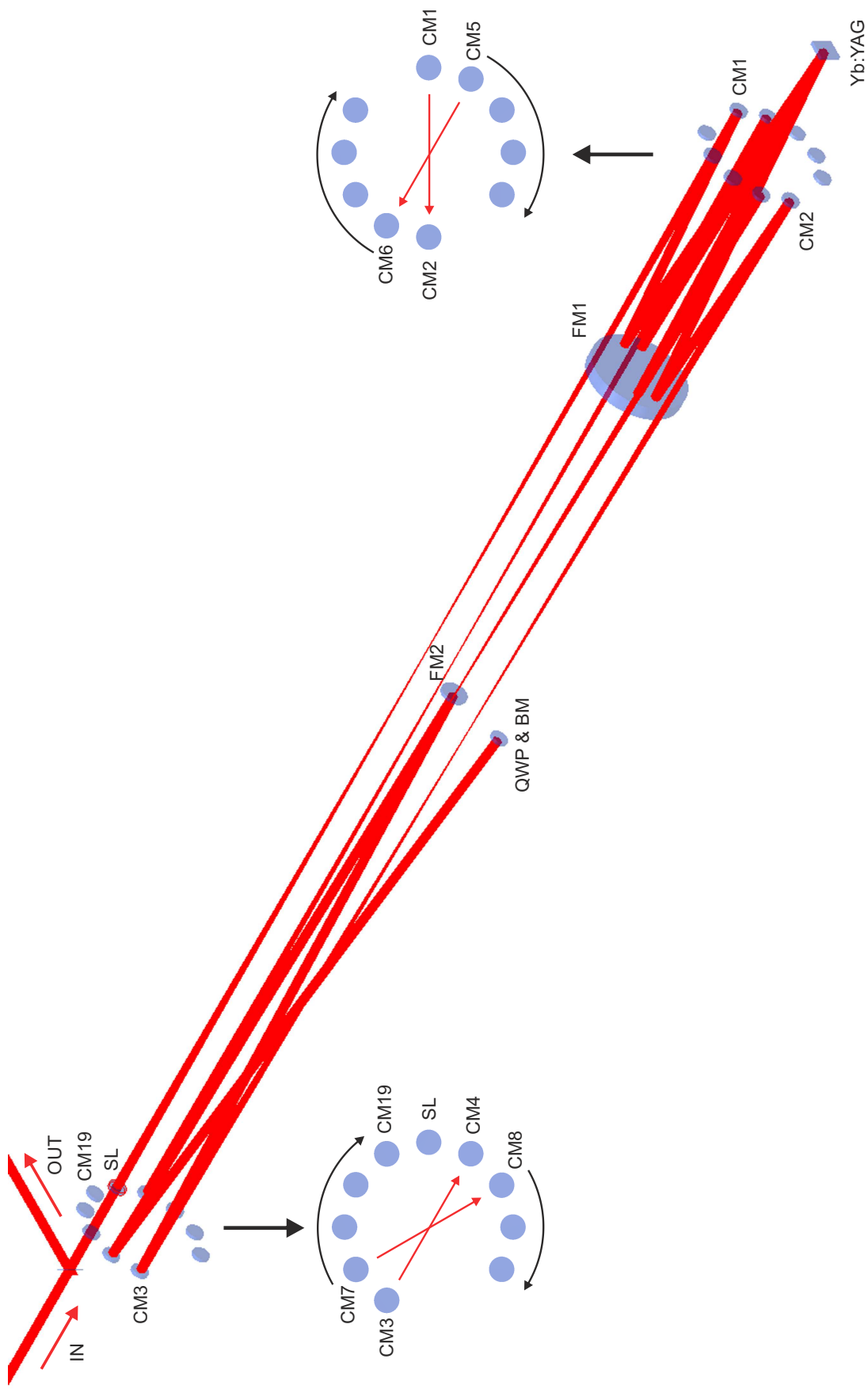


Figure 7.10: Concept of the 3D 20-pass relay-imaging amplifier. It combines 5 double-passes in 5 different planes rotated by an angle of 30° with respect to each other. The whole arrangement is passed twice, realized via back-reflection and polarization-separation, allowing for 20 amplification passes in the Yb:YAG crystal. For the sake of clarity only 4 passes are shown. The incoming beam is imaged with a spherical lens (SL) and a concave mirror (CM1) (ROC = 2 m) to the Yb:YAG crystal in the pump chamber via a folding mirror (FM1). The active-mirror Yb:YAG is double passed. From there the beam is imaged via CM2 and CM3 onto a plane-mirror (FM2) at the image plane position of the Yb:YAG crystal. The transition between the amplification planes is realized via an angle offset between CM2 and CM3. After reflection at FM2 the beam reaches CM4 which is the starting point for the next double-pass through the arrangement on a similar path as before. After 10 passes the beam is back-reflected via CM19 in combination with a plane mirror (BM). A quarter-wave plate (QWP) ensures the separation of the output beam via a polarizer.

7.3.2 Ray-tracing analysis of the 3D 20-pass relay-imaging amplifier

Utilizing curved mirrors under a non-zero AOI introduces wavefront aberrations known as astigmatism leading to different focal lengths in the longitudinal and sagittal beam plane. The concept of the 20-pass 3D relay-imaging amplifier implies that all concave mirrors are used under a certain AOI. This is necessary, on the one hand, to guide the beam from the concave mirrors mounted on the rings towards the center, i.e. the Yb:YAG crystal, and on the other hand, to realize the transition between the amplification planes. Thus, astigmatism and other wavefront aberrations could be a serious issue and therefore have to be analysed. This was done using *LambdaSpect* and a *Matlab* script for post-processing. The simulated wavefronts in the output plane in dependence of the number of passes are plotted in Figure 7.11.

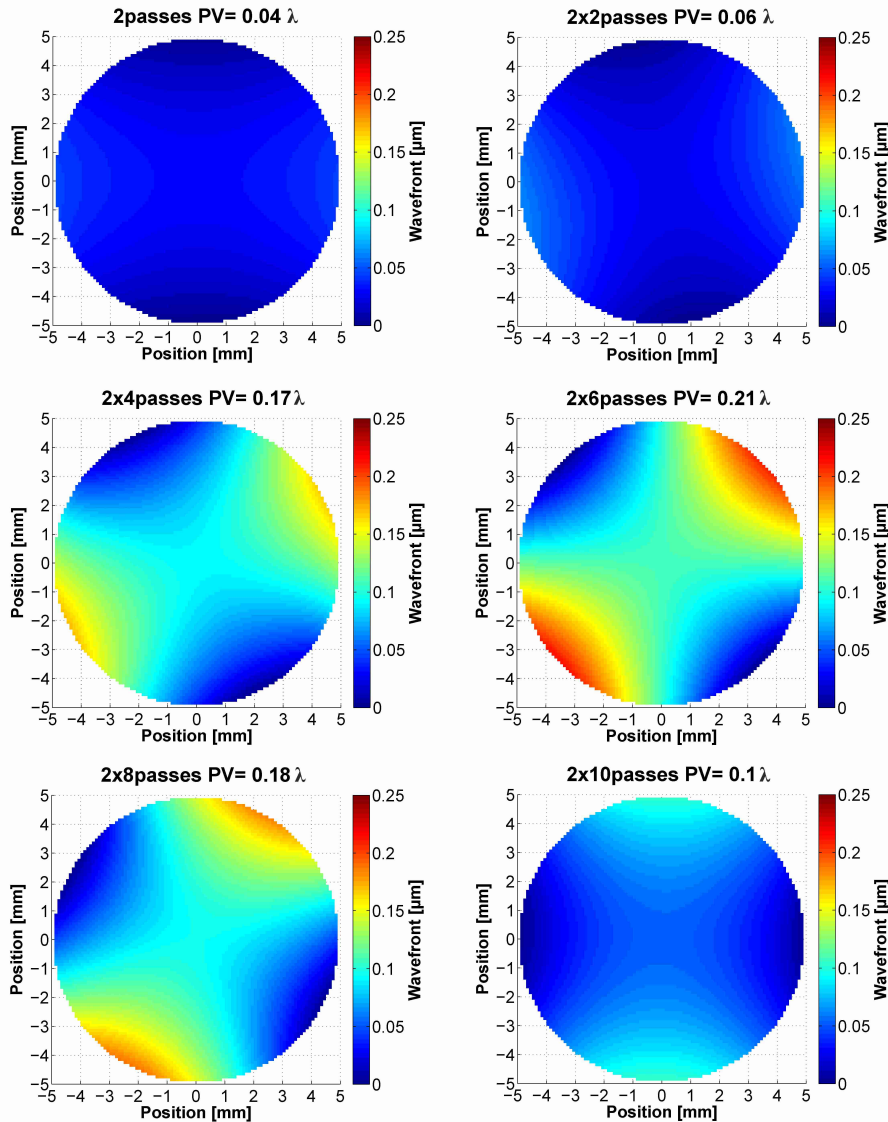


Figure 7.11: Results of a wavefront analysis of the relay-imaging amplifier for different amplification passes. The "2x...passes" indicates the back-reflection. For 2x6passes the largest aberrations ($PV = \lambda/5$) were found. The maximum aberrations for the complete 20 passes are in the range of $\lambda/10$.

Comparing the subfigures in Figure 7.11, one can identify a sort of symmetry axis which rotates according to the number of amplification passes. After 2x6passes, when "half" of the setup is used, the aberrations are highest with a $PV = \lambda/5$. After the complete 20 passes through the setup the symmetry axis has shifted nearly by 90° compared to the initial orientation and the aberrations have declined to a $PV = \lambda/10$. So, the rotation symmetrical approach of the amplifier setup compensates for the astigmatism and the maximum aberrations of $PV = \lambda/10$ after 20 passes can easily be compensated by a deformable mirror if necessary.

After the discussion of the static aberrations inherent to the optical setup, now the influence of the a thermal lens in the Yb:YAG crystal is theoretically investigated. Neglecting higher order aberrations for the moment, a thermal lens will mainly introduce an additional spherical wavefront curvature. To analyse this, a refined version of a *Matlab* script based on ABCD-matrices, originally developed by S. Klingebiel, was used.

Since $dn/dt > 0$ in Yb:YAG [71], a thermal lens will lead to a focussing of the beam. In dependence of the number of round trips in the imaging amplifier this effect adds up and thus the beam diameter on the optics can get smaller than the limit set by the LIDT which is in our case $2w_{min} \approx 0.65$ cm for a pulse energy of 1 J. Figure 7.12 shows the evolution of the beam diameter for the 10th round trip (end mirror $\rightarrow 4f \rightarrow$ Yb:YAG $\rightarrow 4f \rightarrow$ output plane) in the 20-pass relay-imaging amplifier in dependence of the focal length of the thermal lens. If the focal length of the thermal lens for a single reflection off the crystal is shorter than $f_{TL} < 50$ m the beam diameter on CM1, CM3 resp. drops below the above given damage limit.

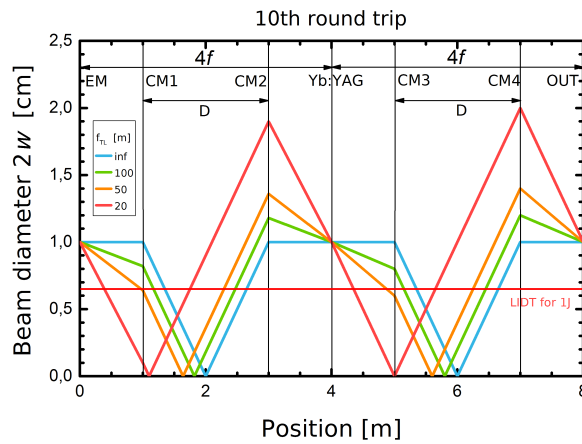


Figure 7.12: Analysis of the influence of a thermal lens to the 10th round trip in the 20-pass relay-imaging amplifier. The position of the intermediate foci shifts in dependence of the focal length of the thermal lens in Yb:YAG. For focal length below 50 m the beam diameter on certain optics is below the limit given by the damage threshold of the used coatings. However, the beam size in the crystal itself stays constant.

However, a major benefit of the relay-imaging multi-pass concept is the possibility to compensate the thermal-lens-induced shift of the intermediate foci by adapting the distance D between the two groups of concave mirrors. As an example, as illustrated in Figure 7.13, for the case of $f_{TL} = 50$ m D has to be shortened by 20 mm in order to restore the beam diameters of the configuration without thermal lensing.

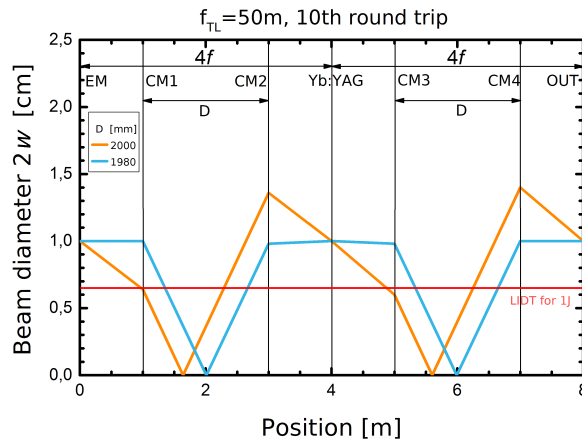


Figure 7.13: Counteracting a thermal lens with the 3D 20-pass relay-imaging amplifier setup. By adapting the distance D between the two groups of concave mirrors the influence of the thermal lens on the beam diameter can be minimized. In the case of $f_{TL} = 50$ m the distance D has to be shortened by 20 mm.

7.3.3 Mechanical design of the 20-pass relay-imaging amplifier

In summary, the analysis of the concept of the 20-pass relay-imaging amplifier so far has not revealed any major drawbacks - except its complexity which may lead to a challenging mechanical design. As already mentioned, several geometrical and space constraints have to be taken into account.

The basic idea for the realization is to mount all optics on carrier rings to keep the rotational symmetry. The rings are adjustable and mounted on 4 carrier rails. Additional mounting rings, supporting the carrier rails, are used to fix the carrier rings and rails into a $\varnothing 320$ mm vacuum tube which consists of 4 parts. The opto-mechanical assembly only contacts the main part of the tube ($L = 1.6$ m) allowing for fast access of the pump chamber and the concave mirror rings.

The mechanical design is illustrated in Figure 7.15 on the next page.

Another important constraint for the mechanical design is the very short working distance of the pump module. The distance between the last lens of the homogenization optics, see Section 7.1, and the Yb:YAG crystal is only 60 mm, requiring an elaborate design of the so-called "pump chamber". Furthermore, the beam path has to be folded two more times compared to the setup shown in Figure 7.10 to ensure the accessibility of the Yb:YAG crystal for the pump and seed beams as shown in Figure 7.14 a). The second folding optic is a dichroic mirror with high reflectivity for 1030 nm and high transmission for 940 nm under an $\text{AOI} = 45^\circ$. The close proximity of these two wavelengths in combination with the required high damage threshold and low losses of the mirror was a great challenge for the coating manufacturer and finally solved by using electron beam deposition (EBD) in combination with HfO_2 as the high-index material of the coating. However, due to the fabrication process the position of the reflection edge under vacuum conditions shifts which has to be taken into account and pre-compensated. The above mentioned short working distance of the pump module made it necessary to include the imaging lens of the pump beam homogenization setup into the pump chamber, i.e. into the vacuum tube, illustrated in Figure 7.14 b) which made additional motorization necessary.

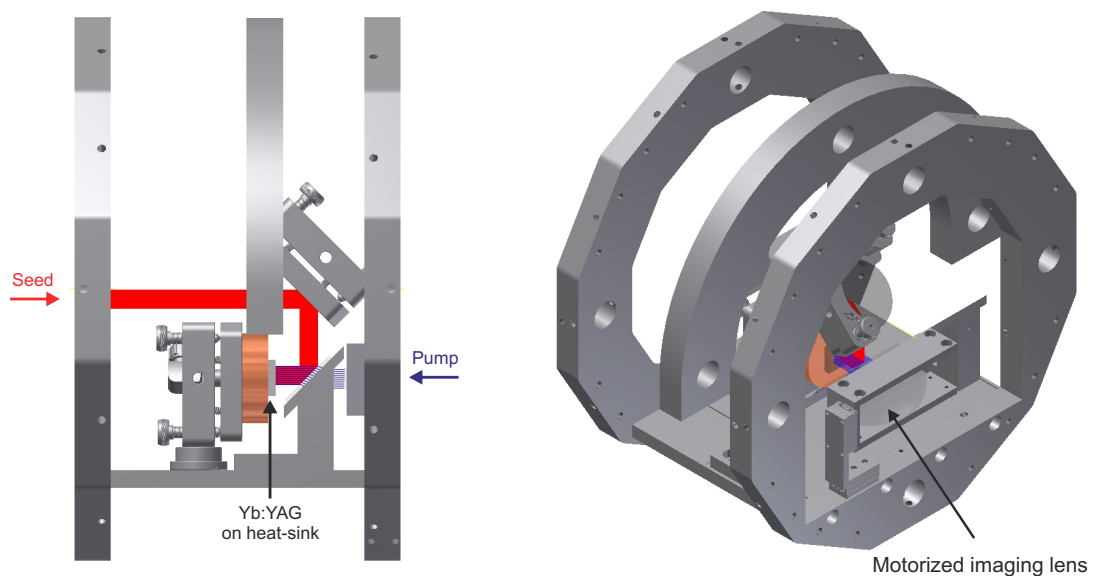


Figure 7.14: Mechanical design of the pump chamber. In order to ensure the accessibility of the Yb:YAG crystal for the pump beam (blue) and the seed beam (red) the seed beam path had to be folded two more times. Therefore, as depicted on the left side, a dichroic mirror reflecting the seed beam and transmitting the pump beam at 45° AOI is necessary. Due to the very short working distance of 60 mm of the pump module, the imaging lens of the pump beam homogenization setup had to be included into the pump chamber, as depicted on the right side.

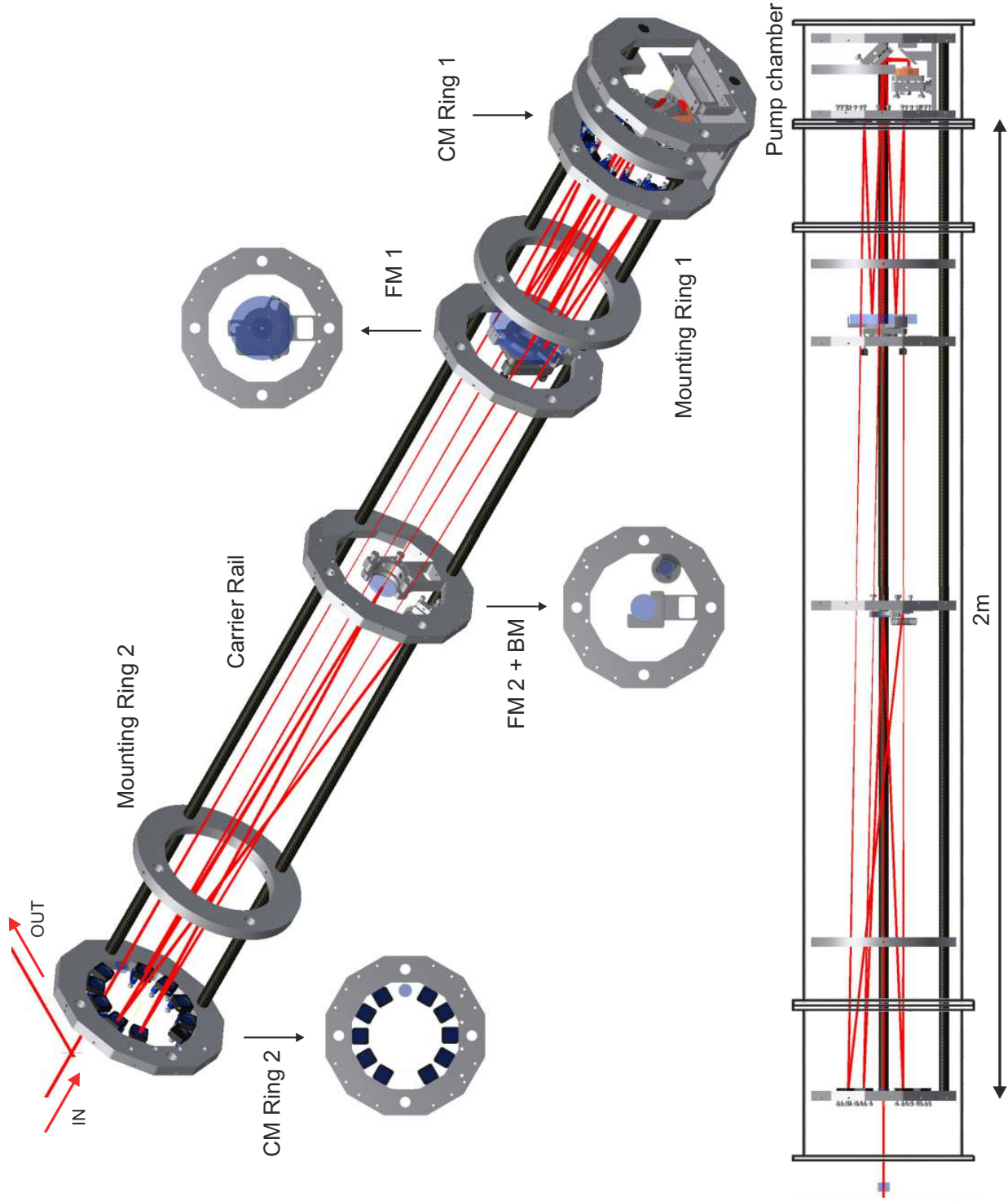


Figure 7.15: Mechanical design of the 3D 20-pass relay-imaging amplifier. The illustration resembles Figure 7.10 now including the mechanical parts. All optics are mounted on carrier rings which itself sit adjustable on carrier rails (4 in total, only 2 depicted). The rotational symmetry of this construction allows for fitting the whole setup into a vacuum tube, as indicated in the lower illustration, where the setup is attached via the mounting rings. The vacuum tube consists of 4 parts and only the main part ($L = 1.6\text{m}$) used to mount the construction which allows for fast access of the pump chamber and the concave mirror rings. (CM: concave mirror, FM: folding mirror)

So, in conclusion and despite the complexity of the whole setup the decision was made to build the 3D 20-pass relay-imaging amplifier in the above presented design. The pros of this approach are its ability to compensate thermal lensing and the constant beam size in the Yb:YAG plane. This allows for highest energy extraction and furthermore for comparing the performance of the different Yb:YAG crystal setups in a reproducible manner. However, the cons are that some optics, e.g. the end mirror, are not easily accessible which makes the alignment and replacement complicated and might be a drawback for operation.

The following figures show photographs taken during the implementation of the 3D 20-pass relay-imaging amplifier in the laboratory.

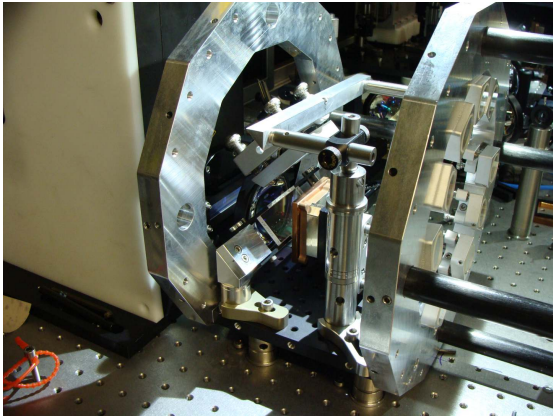


Figure 7.16: Early version of the pump chamber

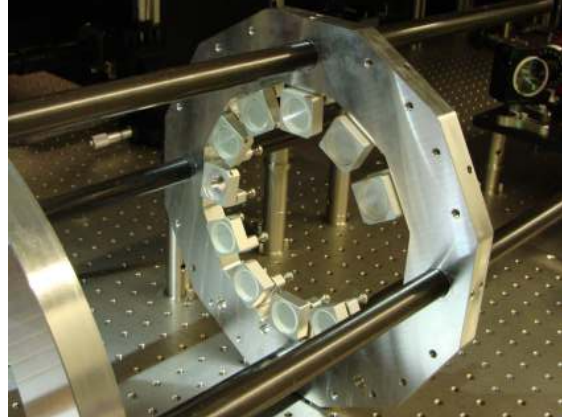


Figure 7.17: Carrier ring with a set of concave mirrors



Figure 7.18: Impressions of the tube inner arrangement I



Figure 7.19: Impressions of the tube inner arrangement II

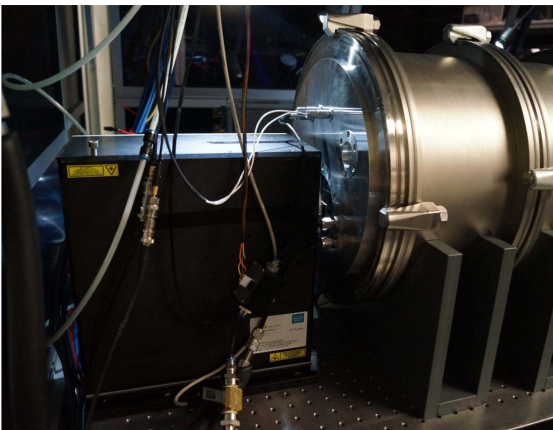


Figure 7.20: Front part of the tube with pump module



Figure 7.21: The final vacuum arrangement

Part V

EXPERIMENTS

LOW-ENERGY EXPERIMENTS

In this chapter, all crystal setups introduced in Section 7.2 are characterized according to their performance in the 20-pass relay-imaging amplifier. For all measurements in this campaign, the amplified pulse energy was constrained to 400 mJ in order to stay safely below the damage fluences for all experimental conditions. This ensures the comparability of all measurements, while still encountering first signs of saturation.

8.1 Input parameters of the "low-energy" campaign

The main aim of this "low-energy" campaign was to investigate the performance of the different crystal setups with respect to the heat sink temperature (T_{HS}) and repetition rate (f_{rep}). All other parameters, such as input beam profile and seed spectrum, were kept constant.

In order to obtain a well-defined beam profile for seeding the amplifier, the beam out of the 300 mJ amplifier, see Figure 6.10 b) is enlarged and only the center part is transmitted by an adjustable iris. Subsequently, the beam is spatially filtered to remove the resulting diffraction rings. This setup allows the adjustment of the ideal beam size for amplification simply by opening or closing the iris. After some pre-tests, the beam size was set to 4.6 mm (FWHM), as shown in Figure 8.1 a). A typical seed spectrum, spectrally pre-shaped to counteract the gain narrowing in the amplifier, is depicted in Figure 8.1 b). A stable high order modulation is noticeable whose origin is not yet fully understood.

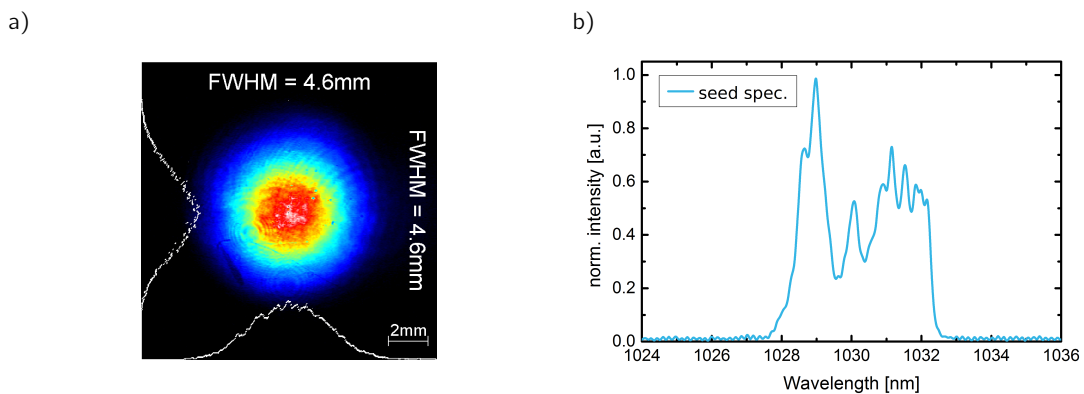


Figure 8.1: Typical input beam profile (a) and seed spectrum (b) for the low-energy campaign. To counteract gain-narrowing the seed spectrum is already pre-shaped with the *Dazzler*.

As described in Section 7.3, the amplifier is set up in a vacuum tube, except for the pump module, which requires a transfer window for the pump radiation. This window and the dichroic mirror, to separate pump and seed beam, introduce optical losses ($\approx 15\%$) reducing the maximum available pump power to 11.3 kW. During the whole campaign, the pump power was always set to this maximum. However, for certain measurements the pump pulse duration was varied.

Table 8.1 summarizes the input parameters of the "low energy" campaign.

P_{Pump}	11.3 kW
t_{Pump}	¹ 1000 μs ... 2000 μs ² 1500 μs
A_{Pump}	10x10 mm ² (FWHM), see Figure 7.2 b)
Pump passes	2
Pump spectrum	Gaussian-shaped, FWHM 9 nm at 938 nm see Figure 7.3 b)
Amplification passes	2x5x2 = 20
d_{Seed}	\approx 4.6 mm (FWHM), see Figure 8.1 a)
Seed spectrum	measured, see Figure 8.1 b)
E_{Seed}	¹ 1 mJ ² set to achieve max. 400 mJ output

Table 8.1: Common parameters of the "low energy" campaign. ^{1,2} indicates different experimental runs.

8.2 Regression analysis procedure

The model of the laser pulse amplification, which is described in Part ii, is based on a set of input parameters. Some of them, such as the number of pump and amplification passes are given by the setup. Others, such as beam size or heat sink temperature (T_{hs}), can be measured. Nevertheless, there are two parameters which elude independent quantification. One of them is the impact of the amplified spontaneous emission (ASE) resp. parasitic oscillations (PO) which are accounted for by the term M_{ASE} in the simulations. The second unknown parameter is the effective crystal temperature (T_{eff}) at which the amplification takes place. It depends on the heat sink temperature (T_{hs}) and the repetition rate (f_{rep}) and is considered in the simulation via the temperature-dependence of the emission and absorption spectra.

Since all the other parameters are known, M_{ASE} and T_{eff} can be determined by fitting the model results to the measured amplification performance.

However, the modelling results are no simple analytical functions of these two parameters and thus this fitting is done in 2 steps, presented on the next page.

At first, the "single-shot" ($f_{rep} = 0.2 \text{ Hz}$) data are used to calculate the M_{ASE} . This is done under the assumption that in single-shot operation the effective crystal temperature and heat sink temperature should closely match.

Figure 8.2 a) illustrates step I. It shows the measured data of the 2% \times 6 \times 20 Au1 crystal setup and the corresponding error bars for a single-shot measurement at $T_{hs} = 20^\circ \text{C}$. The plotted lines are the result of the M_{ASE} evaluation using the simulation. The range indicated by the error bars of the measurement corresponds to $\pm 1\%$ error of M_{ASE} .

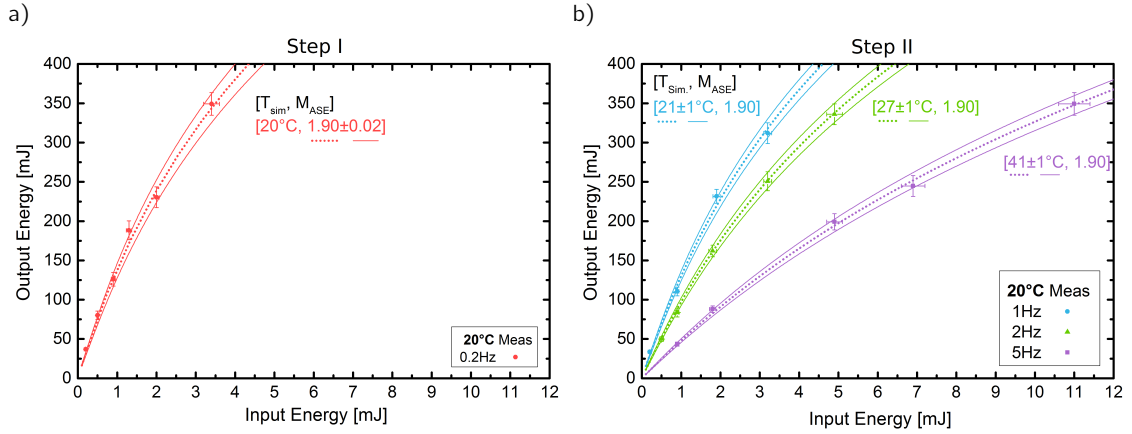


Figure 8.2: Illustration of the regression analysis procedure performed with results obtained with the 2% \times 6 \times 20 Au1 crystal setup at $T_{hs} = 20^\circ \text{C}$. In Step I (a) the simulated temperature (T_{eff}) was kept constant at T_{hs} since they should closely match in single-shot operation ($f_{rep} = 0.2 \text{ Hz}$) while M_{ASE} was determined. An error of $\pm 1\%$ M_{ASE} reproduces the range given by the error bars of the measurement. Subfigure b) shows step II of the analysis. In step I the determined value for M_{ASE} is now kept constant while T_{eff} for the higher repetition rates is calculated. In that way, M_{ASE} can be determined with an accuracy of $\pm 1^\circ \text{C}$, neglecting however the systematic error caused by the assumption of a fixed M_{ASE} .

In step II, illustrated in Figure 8.2 b), the value of M_{ASE} determined in step I is used to calculate the effective crystal temperature for the higher repetition rates. In that way, T_{eff} can be determined with an accuracy of $\pm 1^\circ \text{C}$. However, assuming a fixed M_{ASE} might be fraught with some inaccuracies since a higher effective crystal temperature leads to a higher absorption of the ASE in the pumped area and thus should give a lower M_{ASE} . Therefore, a unique solution is not possible with this approach. Nevertheless, assuming a fixed M_{ASE} is expected to give a reasonable value for T_{eff} .

The gain curves measured at different heat sink temperatures are analysed in the same way leading to a set of $T_{eff}(f_{rep}, T_{hs})$ and $M_{ASE}(T_{hs})$. Using this data set, a slope value $R_{crystal}$ can be extracted:

$$T_{eff}(f_{rep}, T_{hs}) = R_{crystal} \cdot f_{rep} + T_{hs} \quad (8.1)$$

$R_{crystal}$ [K/Hz] represents a heat property characteristic for any given crystal setup and measures the dependence of the effective crystal temperature on the pump repetition rate, which is proportional to the power of the absorbed pump light. It depends on the thermal properties of the individual crystals, the crystal thickness and the crystal size. Furthermore, it is determined by the thermal conductivity and thickness of the glue layer and the effective thermal conductivity of the heat sink. Thus, $R_{crystal}$ can be used to compare the different crystal setups.

8.3 Amplification performance

The amplification performance of the individual crystal assemblies was characterized in two steps where the results of the second step were used to perform the regression analysis presented above.

In the first step, the gain was measured at an input energy of 1 mJ and a repetition rate of 1 Hz in dependence of the pump pulse duration and heat sink temperature. This way of evaluation directly shows if parasitic oscillations occur: At the point in time when the transverse gain reaches the threshold, see Section 2.5, parasitic oscillations can establish and thus will reduce the gain. For lower heat sink temperatures the overall gain is higher and the absorption of ASE in the unpumped area is reduced due to the lower ground-state absorption, see Section 7.2 and Section 3.3. Hence, the depletion of the gain should start earlier and the reduction should have a higher impact compared to higher heat sink temperatures. However, the final gain at the lower heat sink temperatures can still be higher compared to higher heat sink temperatures - which is from particular interest in this measurement. As an example, the behaviour of the 2°x6x20 Au1 crystal setup is shown in Figure 8.3 a). The described influences of the parasitic effects are clearly noticeable.

In the second step, the repetition-rate dependent amplification is studied at a pump pulse duration of 1500 μs for 3 different heat sink temperatures. Measurements exhibiting the highest gain are located closer to the left side of the plot, see Figure 8.3 b) illustrating the measurement of the 2°x6x20 Au1 crystal setup at $T_{\text{hs}} = 20^\circ\text{C}$ including the resulting curves of the regression analysis explained in Section 8.2.

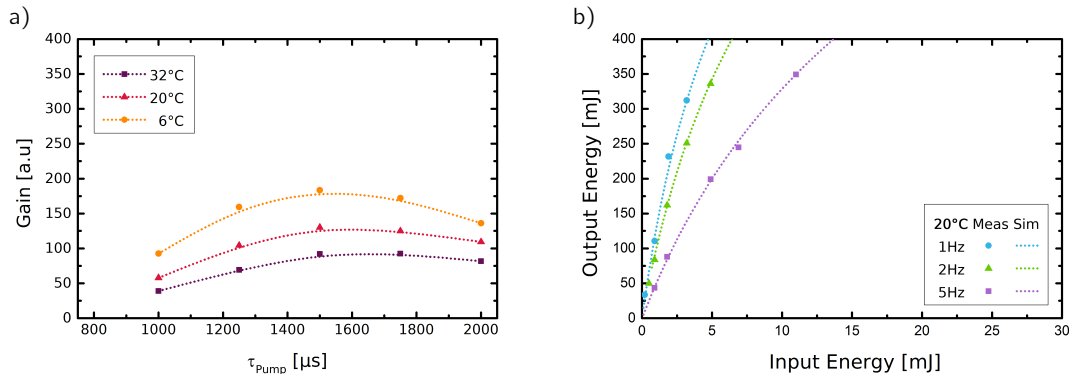


Figure 8.3: Example of the two-step procedure for determining for the amplification performance of the 2°x6x20 Au1 crystal setup. Subfigure a) shows the gain at an input energy of 1 mJ in dependence of the pump pulse duration and the heat sink temperature. As expected, lower heat sink temperatures lead to a higher gain but also increase parasitic effects. These effects lead to a reduction of the gain for longer pump pulse durations. The output energy in dependence of the pump repetition rate at $T_{\text{hs}} = 20^\circ\text{C}$ is shown in b). One clearly sees that the increase of the repetition rate which leads to an increase of the effective crystal temperature reduces the gain and hence the output energy. *The dotted lines in a) are not the result of a simulation, there are just to guide the eye. The scales of the subfigures a) and b) are chosen to allow direct comparability with the subfigures on pages 69,70,71.*

On the following pages, the measurement results of all crystal setups are illustrated according to the above mentioned routines. Comparable results, i.e. the gain of identical crystals, are compiled on the same page.

8.3.1 2%×6×20 Au1 crystal setup

vs. 2%×6×40 Au1 crystal setup

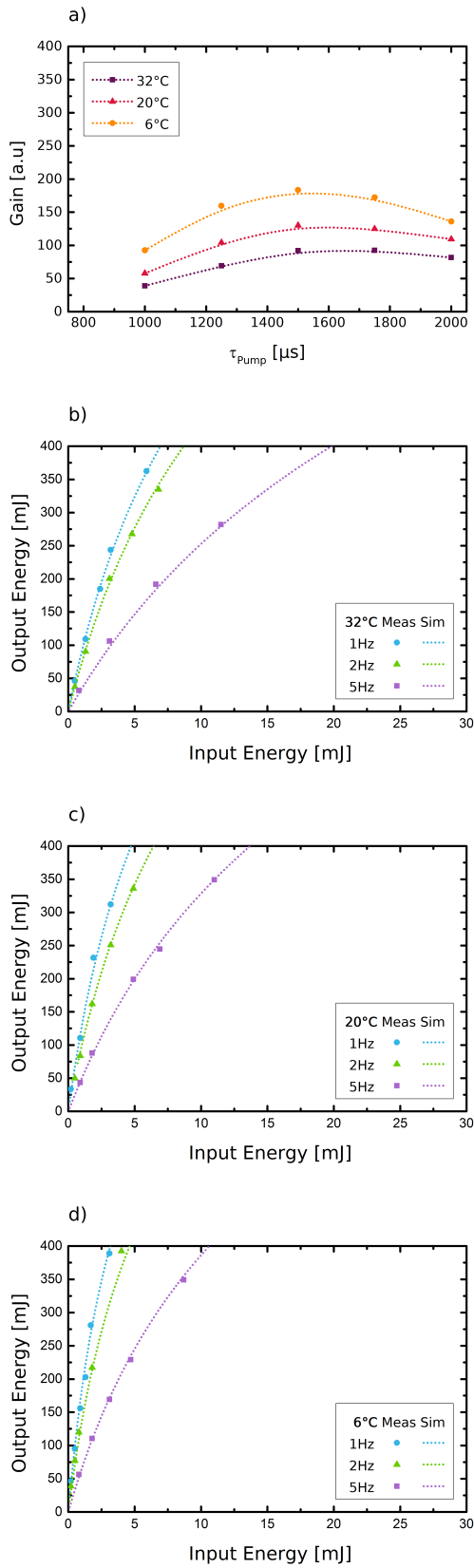


Figure 8.4: 2%×6×20 Au1 crystal setup

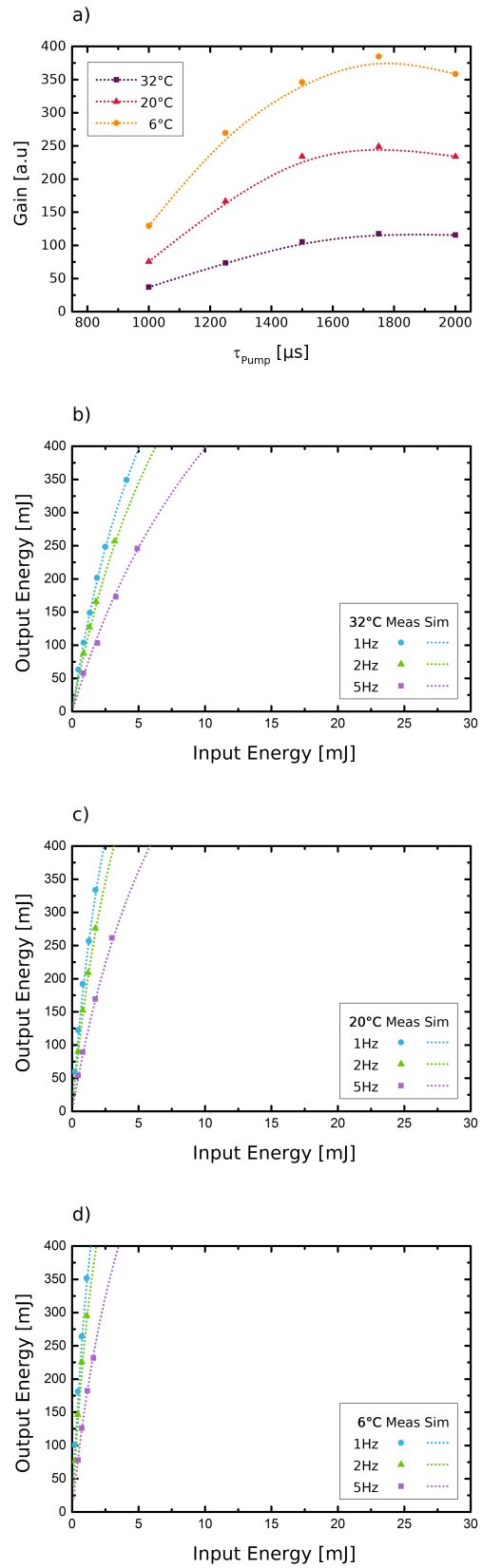


Figure 8.5: 2%×6×40 Au1 crystal setup

The scales of the subfigures b,c,d on pages 69,70,71 are kept constant for direct comparability

8.3.2 6% \times 3 \times 20 Au1 crystal setup

vs. 6% \times 3 \times 20 Ni 2 crystal setup

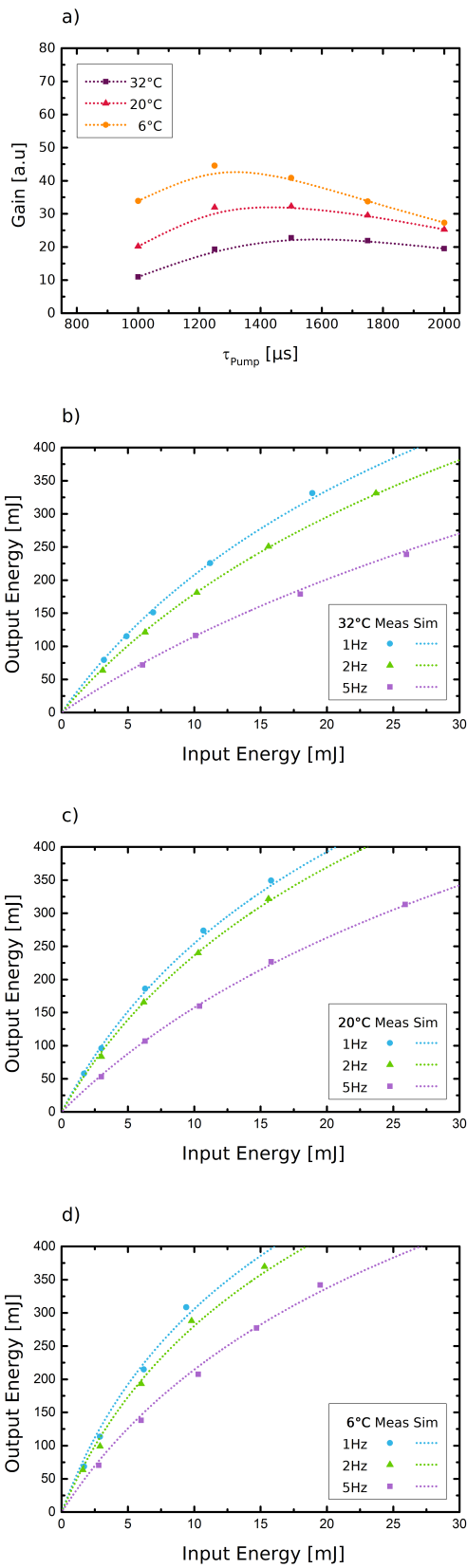


Figure 8.6: 6% \times 3 \times 20 Au1 crystal setup

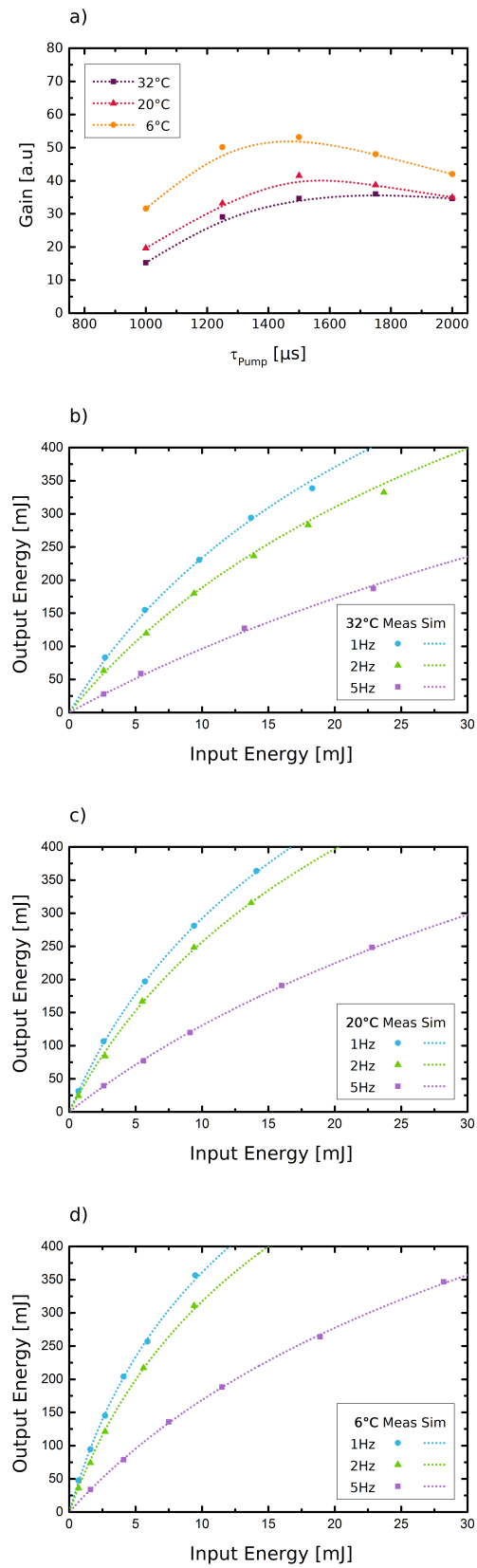


Figure 8.7: 6% \times 3 \times 20 Ni 2 crystal setup

The scales of the subfigures b,c,d on pages 69,70,71 are kept constant for direct comparability

8.3.3 8% \times 2 \times 20 Au1 crystal setup

vs. 8% \times 2 \times 20 Ni 3 crystal setup

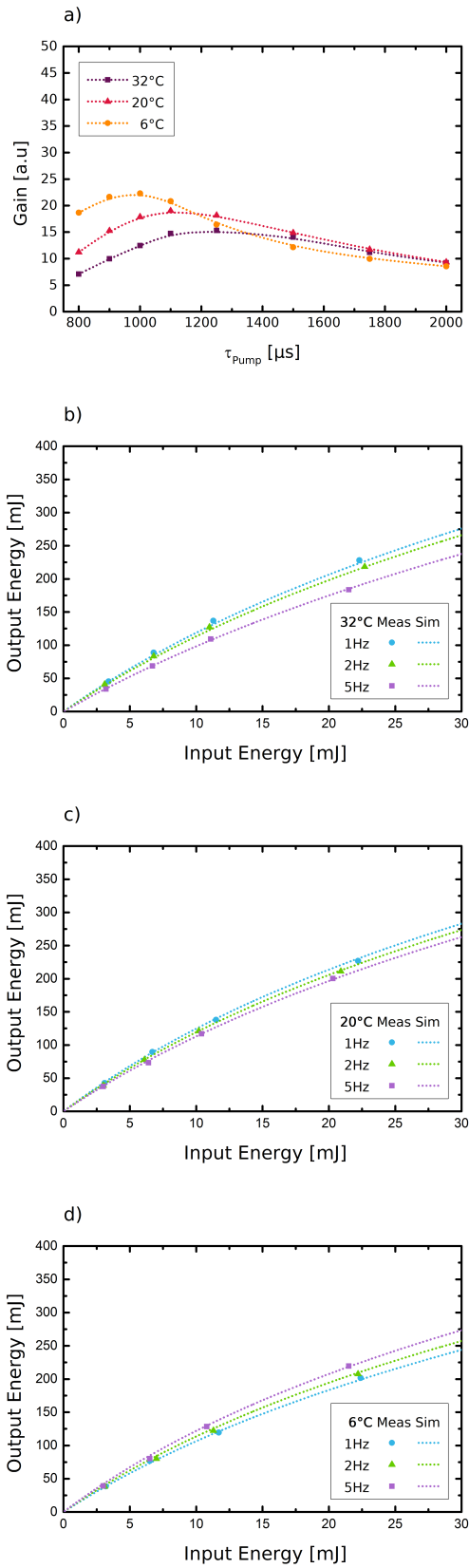


Figure 8.8: 8% \times 2 \times 20 Au1 crystal setup

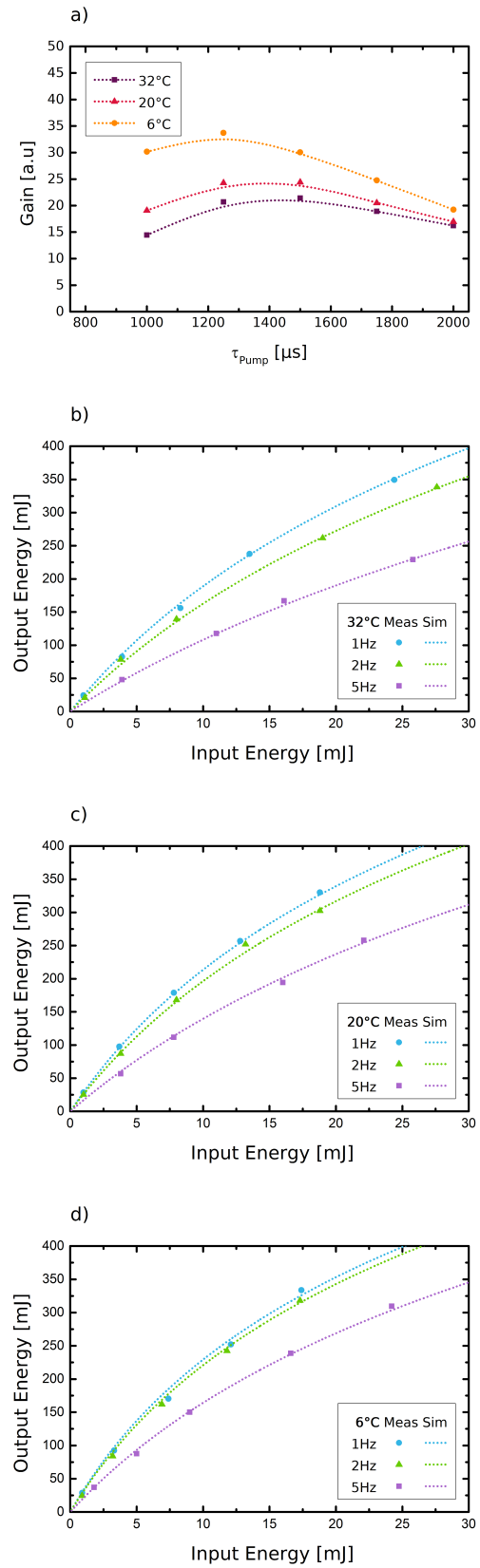


Figure 8.9: 8% \times 2 \times 20 Ni 3 crystal setup

The scales of the subfigures b,c,d on pages 69,70,71 are kept constant for direct comparability

8.4 Comparison of the amplification performance

The following table summarizes the key performance parameters extracted from [Figures 8.4 - 8.9](#). In addition to M_{ASE} and T_{eff} , calculated with the analysis described in Section 8.2, it further specifies the maximum gain obtained in the pump duration dependent measurements.

crystal setup	T_{hs} [° C]	$G_{max}@ 1 \text{ mJ}$	M_{ASE}	$R_{crystal}$ [K/Hz]
2% \times 6 \times 20 Au1	32	93 @ 1750 μ s	1.83	3.27 ± 0.86
	20	130 @ 1500 μ s	1.90	
	6	184 @ 1500 μ s	2.07	
2% \times 6 \times 40 Au1	32	118 @ 1750 μ s	1.76	2.42 ± 0.69
	20	249 @ 1750 μ s	1.76	
	6	385 @ 1750 μ s	1.88	
6% \times 3 \times 20 Au1	32	23 @ 1500 μ s	1.91	1.71 ± 0.72
	20	32 @ 1250 μ s	2.01	
	6	44 @ 1250 μ s	2.23	
6% \times 3 \times 20 Ni 2	32	36 @ 1750 μ s	1.84	3.22 ± 0.80
	20	42 @ 1500 μ s	1.94	
	6	53 @ 1500 μ s	2.13	
8% \times 2 \times 20 Au1	32	15 @ 1250 μ s	2.20	0.93 ± 0.16
	20	19 @ 1100 μ s	2.38	
	6	22 @ 1000 μ s	2.77	
8% \times 2 \times 20 Ni 3	32	21 @ 1500 μ s	2.09	1.48 ± 0.69
	20	24 @ 1250 μ s	2.20	
	6	34 @ 1250 μ s	2.49	

Table 8.2: Summarized results of the low energy campaign and the results of the regression analysis. The best values are highlighted in green and the worst in red.

So, all pump duration dependent measurements ([Subfigures a](#)) in 8.4 - 8.9), show that there is an ideal pump pulse duration for each crystal assembly in order to achieve the highest gain which is determined by the onset of parasitic effects as explained in Section 8.3. However, all measurements show that the highest individual gain is achieved at the lowest heat sink temperature which at the same time lead to a premature start of parasitic effects which increases with the doping concentration due to the higher initial transverse gain.

Therefore, the highest gain is measured in the 2% \times 6 \times 40 Au1 assembly ($G=385 @ T_{hs} = 6^\circ$) followed by the 2% \times 6 \times 20 Au1 crystal setup ($G=184 @ T_{hs} = 6^\circ$). In this case, the only difference between both setups is the 3 times larger absorbing length for ASE in the 2% \times 6 \times 40 Au1 - proving the concept of effective ASE resp. PO suppression by a larger unpumped area or an absorbing cladding. The fact that the calculated values for M_{ASE} , see Table 8.2, in case of the 2% \times 6 \times 40 Au1 crystal setup at $T_{hs} = 20^\circ\text{C}$ and $T_{hs} = 32^\circ\text{C}$ are identical proves that in this case no parasitic oscillations occur at all. The potential of cooling down the crystals can also be seen in this measurements, see [Figure 8.5 b](#)), c), d). In absence of parasitic effects, the reduction of the gain when switching to higher repetition rates can be fully compensated by operating at lower heat sink temperatures.

Furthermore, as expected, the thinner crystals - despite having a lower thermal conductivity due to the higher doping concentration [72, 73] - exhibit a better capability in terms of the heat removal as proven by the lower R_{crystal} in this cases. The only exemption is the 6% \times 3 \times 20 Ni 2 crystal assembly which nearly has the same R_{crystal} compared to the 2% \times 6 \times 20 Au1 crystal assembly. Since the main material of all heat sinks is the same (Cu) an explanation for this behaviour can either be the ≈ 4 times lower thermal conductivity of Ni compared to Au (70 W/mK vs. 300 W/mK [74]), or there could be a difference in the thermal conductivity of the used glue. Unfortunately, thermal properties of just one glue type are available (glue #1: 0.22 W/mK). The same behaviour is evident for the two 8%-doped assemblies leading to the conclusion that the combination of Au-plated heat sinks and glue #1 is preferable in terms of heat removal. Additionally, the fact that R_{crystal} is lower for the 2% \times 6 \times 40 Au1 assembly compared to the 2% \times 6 \times 20 Au1 assembly is an evidence that at this crystal thickness already a large amount of heat spreads in radial direction.

Another interesting effect which can be seen when comparing 8.6 a) & 8.6 b) and 8.8 a) & 8.8 b), is that the gain at 1 Hz is lower and the parasitic effects start earlier if the heat sink is Au-coated. An explanation for this effect is an enhancement of the back-reflections by the Au-coating since its reflectivity is higher compared to Ni ($R=0.99$ vs. $R=0.72$ at $\text{AOI}=0^\circ$ and 1030nm [74]). A comparable effect is reported in [45].

8.5 Comparison of the output beam profiles and wavefronts

During all the measurements described above, the output beam profile and wavefront as well as the output spectrum were monitored. A typical output spectrum, measured with the 2% \times 6 \times 20 Au1 crystal setup, in comparison to the seed spectrum is depicted in Figure 8.10. The effect of gain narrowing is clearly visible.

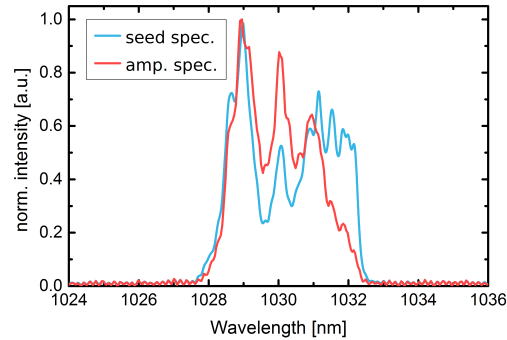


Figure 8.10: Seed spectrum (blue) and a typical output spectrum (red) of the low-energy measurements. The output spectrum is narrowed down by gain narrowing.

A comparison of the input beam profile and the transmitted beam profile without amplification is shown in Figure 8.11. High order modulations in the transmitted beam are observable which may originate from dust on the optics by the filters in front of the camera.

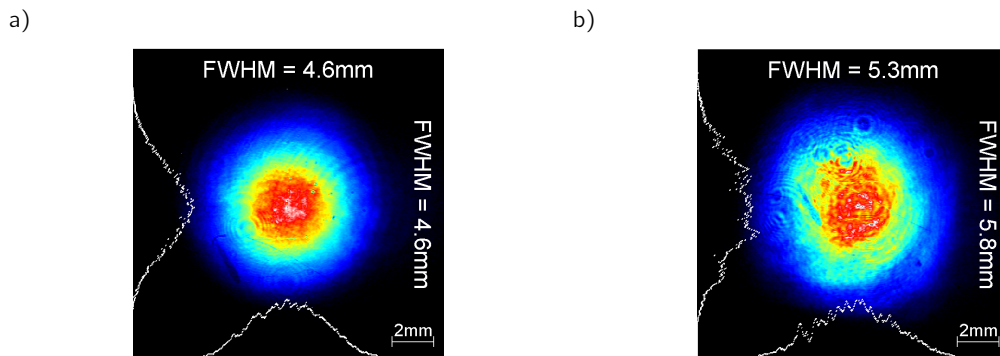
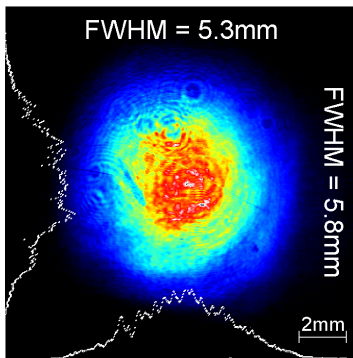


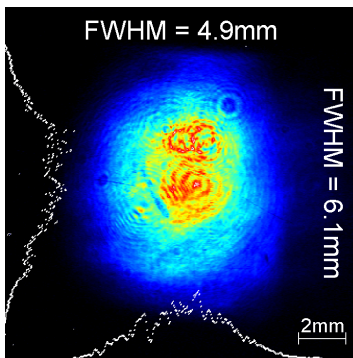
Figure 8.11: Comparison of the input beam profile a) and transmitted beam profile b). The transmitted profile shows additional high order distortions most likely originating from dust on the optics or the filters in front of the camera.

Figure 8.12 shows the output beam profile and wavefronts for different repetition rates in comparison to the unamplified output beam profile and wavefront, measured with the 2% \times 6 \times 20 Au1 crystal setup. A change of the beam profile when going to higher repetition is observable - the beam extends a little bit in y-direction. The measured wavefronts exhibit mainly astigmatism. The fact that wavefront aberrations are highest at 1 Hz repetition rate is not yet fully understood. Furthermore, the effect of the thermal lens in the Yb:YAG crystal is evident when evaluating the wavefront via *Zernike* polynomials. The obtained radius of curvature of the measured wavefront changes from the \approx 264 m without amplification to \approx 18 m at 5 Hz repetition rate, meaning the output beam will be focused 18 m behind the output plane. According to the simulations presented in Section 7.3.2 this 18 m focal length at the output equals a focal length of the Yb:YAG crystal of 180 m for a single reflection off the crystal. In comparison with Figure 7.12 one can see that the beam diameters on all optics in this case are larger than set by the damage threshold of the coatings. Furthermore, the simulation yields a necessary change of distance D between the concave mirrors by -2.8 mm which is in excellent agreement with our empirical findings when adapting this distance in the experiment.

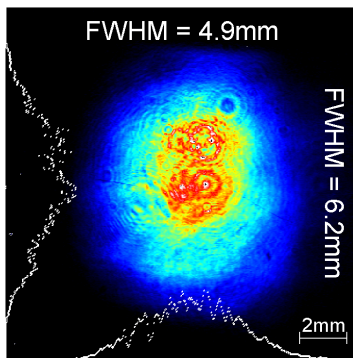
Beam profile



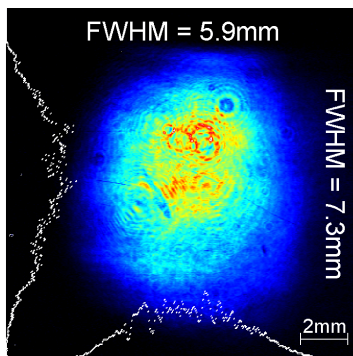
unamp.



1Hz



2Hz



5Hz

Wavefront

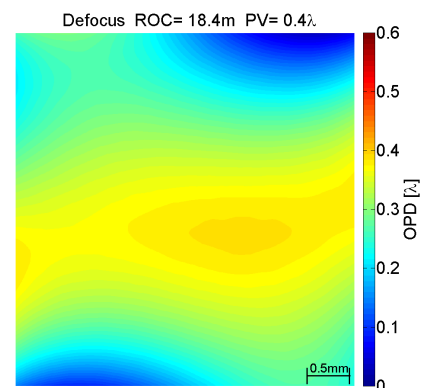
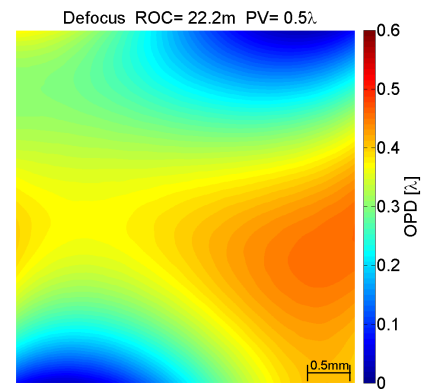
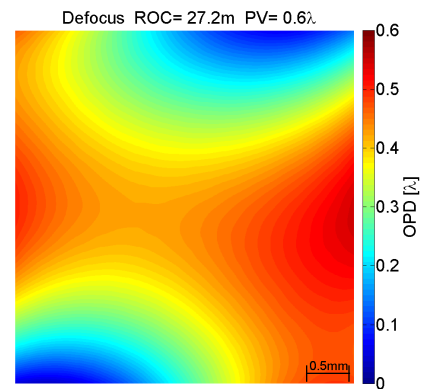
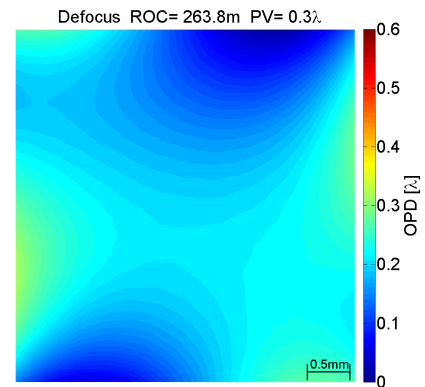


Figure 8.12: Output beam profiles and wavefronts for different repetition rates. When going to higher repetition rates the beam profile extends more in y-direction leading to a slightly elliptical beam profile. The plotted lineouts refer to the intensity peak. The noticeable fringes are due to the used filters in front of the camera. All measured wavefront maps show mostly astigmatism. The maximum wavefront deviation of 0.6λ is obtained in the 1Hz case which is not yet fully understood. The fact the radius of curvature of the wavefront - evaluated using *Zernike* polynomials - changes from the ≈ 264 m without amplification to ≈ 18 m at 5 Hz repetition rate is an evidence for the thermal lens in the crystal.

8.6 Conclusions of the "low-energy" campaign

- the 2%-doped crystals exhibit the highest gain of all investigated assemblies
- all higher-doped crystals suffer severe gain losses due to parasitic oscillations/effects which increases at lower crystal temperatures
- a larger unpumped margin hence absorbing cladding improves the ASE suppression
- the effect of 3-D heat conduction plays a role at least in the 6 mm thick crystals, thus a larger unpumped edge also improves the heat removal since more heat can flow radially than in axial direction
- Au-coated heat sinks are preferable in terms of effective cooling but seem to enhance parasitic oscillations
- in absence of parasitic effects, the reduction of the gain when switching to higher repetition rates can be compensated by going to lower heat sink temperatures
- the higher gain at lower heat sink temperatures might also be a solution to extract comparable energies at reduced crystal thicknesses while keeping a low doping concentration

From these investigation it follows, somewhat unexpectedly, that the rather thick 2% \times 6 \times 40 Au1 crystal assembly exhibits the best performance compromise in terms of gain, ASE suppression and heat conductivity.

The calculated values of M_{ASE} and T_{eff} allow the extrapolation of the output energy for higher input energies. Figure 8.13 a) illustrates the extrapolated saturated energy of the 2% \times 6 \times 40 Au1 and the 8% \times 2 \times 20 Au1 crystal assembly for 20 amplification passes at a heat sink temperature of 20 °C. Although the 8%-doped and thus thinner crystal would have a 15° C lower crystal temperature at 10 Hz repetition rate compared to the 2%-doped crystal the parasitic effects lead to a reduction of saturated energy by 40%. Figure 8.13 b) shows different scenarios for the saturated gain in the 2% \times 6 \times 40 Au1 crystal assembly at 1 Hz repetition rate and at different heat sink temperatures. Immediately evident is the beneficial effect of a reduced crystal temperature on the output energy. However, calculating the maximum extractable energy by assuming hypothetical 100 amplification passes leads to the conclusion that in our setup the output energy is mainly limited by the restricted number of amplification passes.

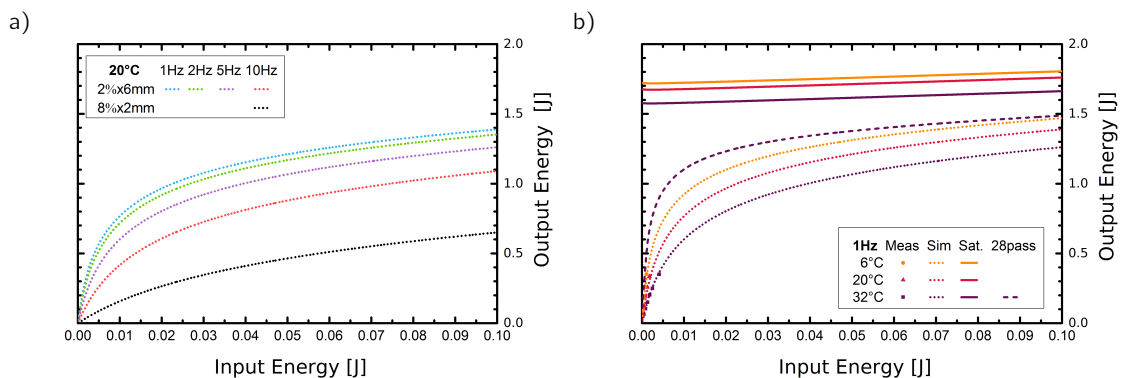


Figure 8.13: Extrapolated output energy of the 2% \times 6 \times 40 Au1 and the 8% \times 2 \times 20 Au1 crystal assembly based on the calculated values of M_{ASE} and T_{eff} . Subfigure a) shows the expected output energies at $T_{hs} = 20^\circ\text{C}$ (dotted, colored lines). The black dotted line illustrates the gain of the 8% \times 2 \times 20 Au1 at $f_{rep} = 10\text{ Hz}$ and $\tau_{pump} = 1100\ \mu\text{s}$. The parasitic effects in this case lead to a 40% lower output energy. Subfigure b) illustrates different scenarios for the saturated gain at 1 Hz repetition rate. The straight lines show the maximum extractable energies calculated by assuming 100 amplification passes were assumed. The dotted lines show the output energy for 20 amplification passes. In both cases one clearly sees the impact of the crystal temperature on the output energies. Nevertheless, the output energy is mainly limited by the restricted number of amplification passes. This also proven by the fact that in case of 32° C heat sink temperature 8 additional passes would lead to the same output energy as in the 6° C case (dashed purple line).

HIGH-ENERGY EXPERIMENTS

As concluded in the previous chapter, the 2% \times 6 \times 40 crystal assembly is best suited for creating pulse energies exceeding 1 J. As a consequence all high-energy experiments were carried out exclusively with this setup.

Besides the main focus of generating pulse energies >1 J the amplified beam profile and the amplified bandwidth are of special interest as well. Since the amplified pulses will later be frequency-doubled and used as pump pulses for OPCPA their near-field beam profile and wavefront have to meet stringent requirements. A top-hat beam profile and a flat wavefront ensure highest frequency doubling and OPCPA efficiencies. Furthermore, the signal beam profile after OPCPA strongly depends on the pump beam profile. To ensure shortest pulse durations after compression it is mandatory to preserve the full bandwidth during amplification. Hence, the spectral pre-shaping by the *Dazzler* has to be adapted to compensate the gain narrowing effects in the 1 J-amplifier.

While the beam profile mainly depends on the repetition rate (thermal lensing), the heat sink temperature (wavefront aberrations due to stress) and the amplification level (saturation effects) the amplified spectrum strongly depends on the overall gain (gain narrowing). So, the beam profile and amplified bandwidth have to be observed for every input/output energy step as well as for the heat sink temperature and adapted if necessary. In order to get an estimate of the strength of these processes and to find ideal input parameters for the high-energy operation several preparatory measurements were performed. The input parameters were kept identical to the low-energy measurements, see Section 8.1, meaning the crystal was pumped with 11.3 kW at a pulse duration of 1500 μ s on a spot size of 10 \times 10mm².

9.1 Preparatory measurements for the high-energy campaign

Figure 9.1 shows again the evolution of the beam profile in dependence of the repetition rate at 20 °C heat sink temperature. The beam profile was measured in the output image plane (near-field) and after 1 m of propagation at an output energy of ≈ 30 mJ.

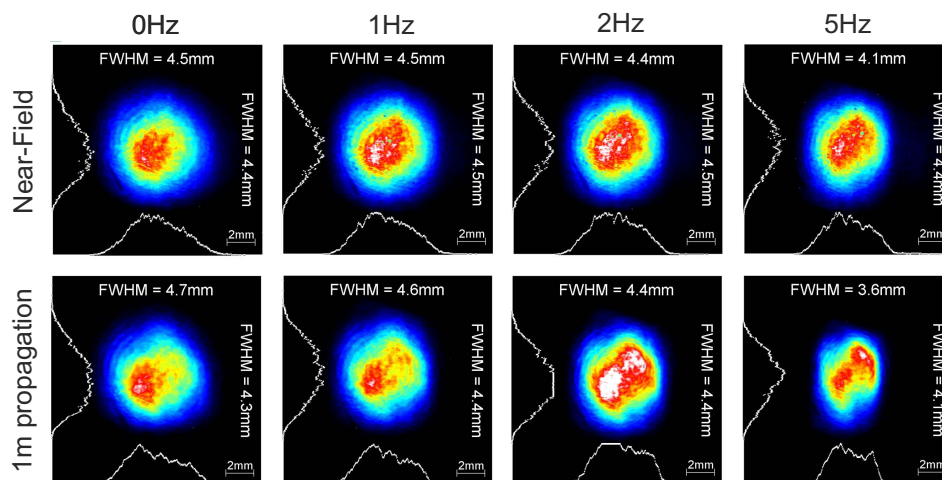


Figure 9.1: Beam profile in dependence of the repetition rate and position. 0 Hz corresponds the unamplified case. For 1 Hz and 2 Hz repetition rate the change of both beam profiles is very minor. However, at 5 Hz, the influence of the thermal lens is clearly evident. After 1 m propagation the beam size has decreased noticeably and high-order wavefront errors also influence the near-field shape in this case. A measurement with a wavefront sensor obtained a change of the ROC of the wavefront from -12 m at 0 Hz to 7 m at 5 Hz.

As shown in Figure 9.1, a noticeable change of the near-field beam profile and of the beam profile after 1 m propagation is detectable when switching to 5 Hz repetition rate. The thermally induced wavefront aberrations - mostly astigmatism and spherical errors as measured in the "low-energy" campaign - lead to a focussing of the beam when switching to higher repetition rates. As expected, the near field profile is less affected by this effect. Since the beam profile after 1 m propagation is comparable to the beam profiles on the curved mirrors in the setup, these optics may suffer damage issues due to this focussing. As mentioned, this thermal lensing can be mitigated by adapting the distance between the imaging optics which is done later on.

The change of the near-field beam profile when increasing the input and consequently the output energy is shown in Figure 9.2. The averaged diameter increases from ≈ 4.5 mm (FWHM) at the lowest input/output energy to ≈ 7.2 mm (FWHM) at the maximum measured output energy and the shape of the near-field beam profile gets more "top-hat"-like. This is caused by the larger pump beam profile, see Figure 7.2 b), compared to the initial seed beam profile and by saturation effects in the center part of the beam which leads to a steepening of the edges. Furthermore, at high energy, a sharp edge appears on the lower part of the beam which is most likely caused by clipping at the small dichroic mirror, see Figure 7.14. This clipping is unavoidable in the current setup but does not limit the high-energy operation.

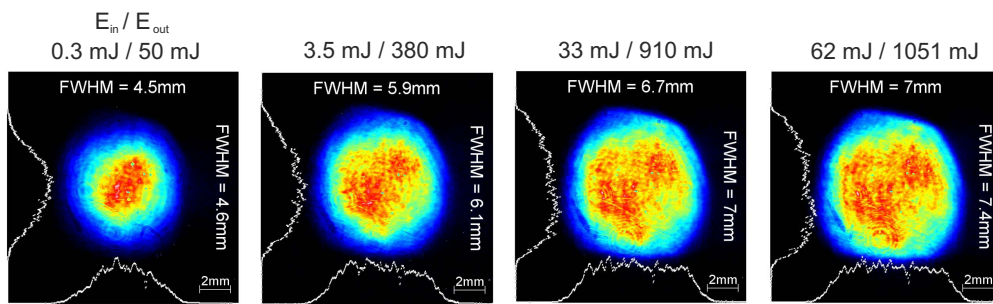


Figure 9.2: Near-field beam profiles depending of the input/output energy at 1 Hz. The averaged diameter changes from ≈ 4.5 mm (FWHM) to ≈ 7.2 mm (FWHM) when going to the highest measured output energy. Furthermore, the beam profile gets more "top-hat"-like which is caused by saturation effects in the beam center part leading to a steepening of the edges.

However, in the course of this preparatory measurements it turned out that there is a thermal drift of the beam inside the vacuum tube when the repetition rate is increased due to heating of the mechanical parts caused by the residual pump light. While the drift could be stabilized/counteracted in the 1 Hz and 2 Hz case by additional cooling devices and remote alignment of the crystal this was out of the correction range at 5 Hz. Additionally, the stress-induced wavefront aberrations at low heat sink temperatures lead to severe changes of the beam profile prohibiting long-term high-energy operation.

Therefore, the full characterization of the amplification performance was exclusively carried out at a heat sink temperature of 20 °C and at 1 Hz and 2 Hz repetition rate.

9.2 High-energy amplification performance

9.2.1 Amplified pulse energy and spectra

After the preparatory phase and the necessary adaptations of the beam profile and seed spectrum the seed energy was increased stepwise and the resulting output energy, beam profile and wavefront, as well as the amplified spectrum were measured. These measurements were carried out at 1 Hz and 2 Hz repetition rate and at a heat sink temperature of 20 °C. The limit for the maximum output energy was set to 1 J in order to not risk any damage of the optics and thus allow for multiple measurements.

Figure 9.3 a) shows the measured amplification performance and the according simulated curves. The final output spectra and the necessary input spectrum are depicted in Figure 9.3 b).

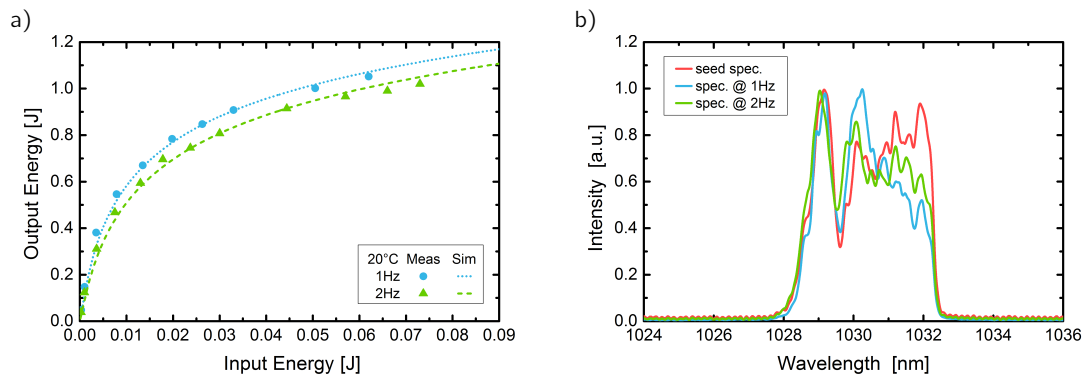


Figure 9.3: High-energy amplification performance of the 2% \times 6 \times 40 crystal setup at 1 Hz and 2 Hz repetition rate and at a heat sink temperature of 20 °C. Subfigure a) depicts the measured amplification performance. At both repetition rates an output energy of 1 J was achieved. Furthermore, the measurements revealed a pulse-to-pulse stability of 1.5% rms at 1 J output energy for both repetition rates. The simulation (dotted lines) implies that even higher output energies are possible when using the full seed energy. However, this was not tested yet in order to prevent damaging of the optics. Subfigure b) shows the amplified spectra at 1 J output energy for a 1 Hz and 2 Hz repetition rate. For comparison the seed spectrum is shown as well. The full spectral bandwidth can be maintained when amplifying to 1 J principally allowing for pulse durations < 0.8 ps after compression.

The main result of the measurements is that at both repetition rates an output energy of 1 J was achieved. While a seed energy of 62 mJ is needed to generate 1 J output energy at 1 Hz repetition rate, the seed energy had to be increased to 73 mJ at 2 Hz due to the higher crystal temperature in this case. Furthermore, the measurements revealed a pulse-to-pulse stability of 1.5% rms at 1 J output energy for both repetition rates. Again, the measured slopes can be reproduced using the simulation code and predicting pulse energies > 1.1 J when using the maximum seed energy of 90 mJ. In comparison to the extrapolated output energies based on the "low-energy" campaign, see Figure 8.13, the measured and simulated output energies are $\approx 15\%$ lower which is due to the fact that a new dichroic mirror, exhibiting different transmission and reflexion characteristics, was installed providing a higher damage threshold.

Again, the *Dazzler* was used in order to shape the seed spectrum in such a way that the full spectral bandwidth of ≈ 3.4 nm is maintained while amplifying to the full energy. Since the same *Dazzler* settings were used for 1 Hz and 2 Hz operation the slight difference in the corresponding high-energy spectra, see Figure 9.3 b), might be an evidence for the different temperature-dependent gain narrowing.

9.2.2 Compression and FROG-evaluation of the amplified pulses

As mentioned, the full spectral bandwidth of the seed pulses can be maintained when amplifying to output energies in the range of 1 J. Moreover, the amplified spectra show a fairly good agreement with the output spectra of the 8-pass booster amplifier, see Figure 6.9 b), which were compressed down to 740 fs, described in detail in Section 6.5.

To adjust and evaluate the pulse duration of the amplified pulses a second-order, single-shot *FROG* [63] was used. By analysing the corresponding autocorrelation trace, the pulse duration (FWHM) was minimized online using the *Dazzler*. The same minimal pulse duration with a shot-to-shot stability of $\pm 1\%$ rms was achieved for 1 Hz and 2 Hz operation.

For the evaluation of the measured FROG-traces, *FROG 3.1.2* provided by *Femtosoft Technologies* was used. The results of the FROG evaluation revealing the shortest pulse duration is shown in Figure 9.4.

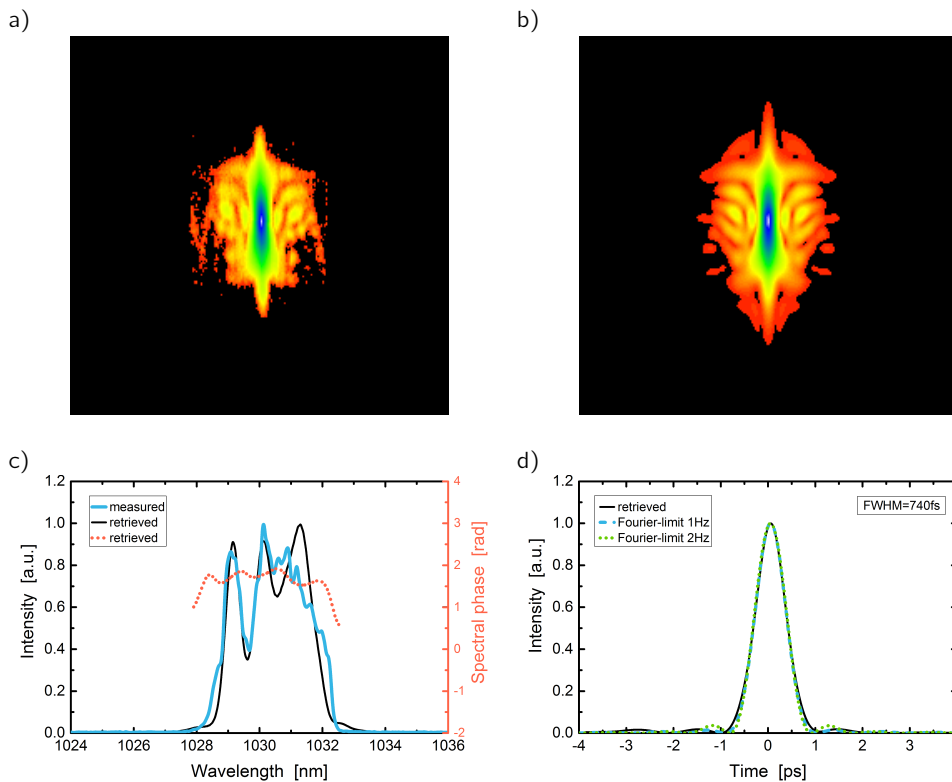


Figure 9.4: FROG evaluation of the shortest compressed pulse. The measured FROG-trace - obtained at 1 Hz and a pulse energy of 800 mJ after compression - is shown in subfigure a) and the retrieved trace - calculated with FROG 3.1.2 from Femtosoft Technologies - is illustrated in subfigure b). The retrieved pulse spectrum (c, black) matches the measured one (c, blue) very well. The corresponding spectral phase (c, orange) is nearly flat. Hence, the retrieved pulse shape (d, black) reproduces the pulse shape calculated by the *Fourier*-transformation of the measured spectra (d, blue & green). The FWHM of the retrieved pulse duration is 740 fs.

A good agreement between the measured and retrieved pulse spectra was obtained (FROG error=0.2% on a 1064x1064 grid), as shown in Figure 9.4 c). The retrieved spectral phase is nearly flat. Thus, the retrieved pulse duration of 740 fs (FWHM) closely matches the Fourier-limited pulse duration of 738 fs (FWHM) extracted from the measured spectra, see Figure 9.4 d). Under consideration of the measured compressor transmission (76%), the maximum compressed pulse energy is calculated to 0.8 J and 0.78 J for 1 Hz and 2 Hz, respectively. Thus, the pulse power (transmitted energy/pulse duration (FWHM)) is calculated to 1.08 TW for 1 Hz and 1.05 TW for 2 Hz. Using a more refined analysis which takes the retrieved temporal pulse shape, cf. Figure 9.4 d), into account leads to a pulse peak power 0.96 TW for 1 Hz and 0.92 TW for 2 Hz operation.

9.2.3 Amplified beam profile and wavefront

The preparatory studies showed that the difference of the near-field beam profiles at low output power between 1 Hz and 2 Hz repetition rate are rather small. An increase of the beam diameter and a steepening of the edges was observed when generating higher output energies. Both findings are confirmed when amplifying to 1 J, as shown in Figure 9.5 a) & b).

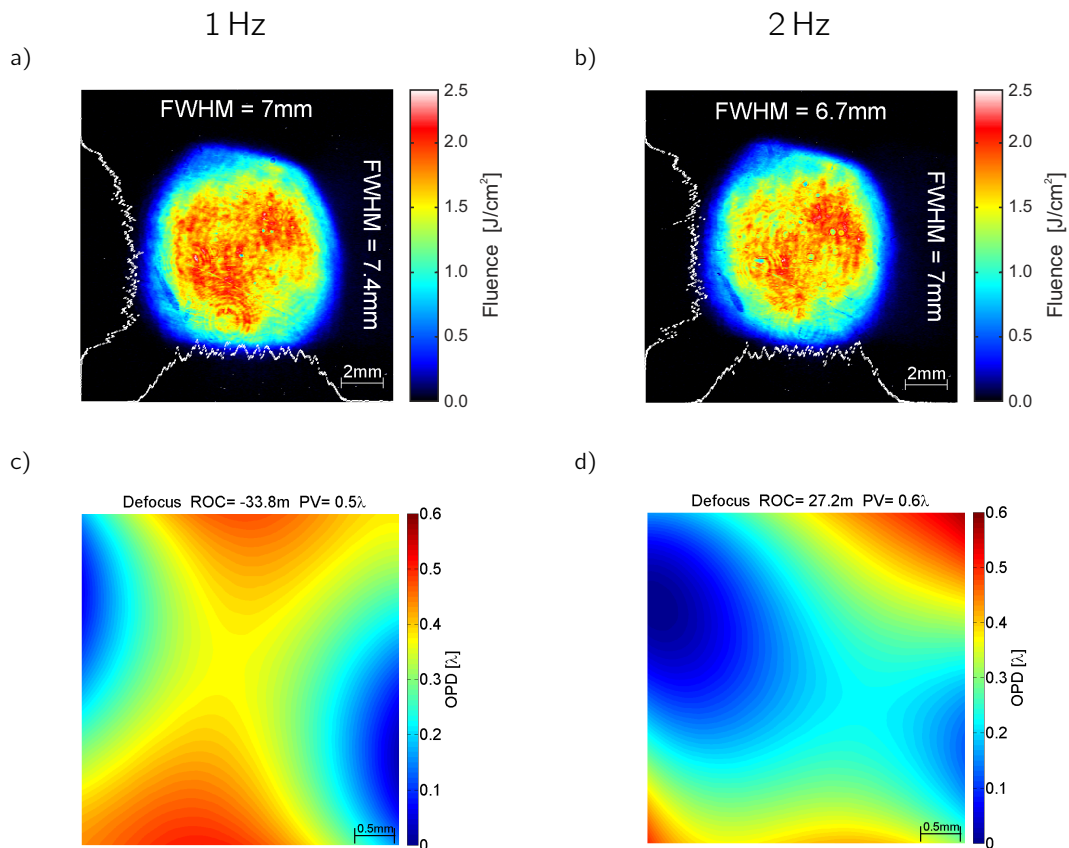


Figure 9.5: Beam profile and wavefront at 1 J output energy for 1 Hz a),c) and 2 Hz b),d) repetition rate. The beam profile and wavefront were measured in the imaging plane at the output of the amplifier tube. The qualitative difference between the beam profiles for 1 Hz and 2 Hz operation is minor. An averaged diameter of ≈ 7 mm (FWHM) is measured. Again, the measured wavefront, see subfigures c) and d), is dominated by astigmatism. The ROC of the spherical component of the wavefront changes from -34 m at 1 Hz to 27 m at 2 Hz due to the positive thermal lens.

The measured beam profiles for 1 Hz and 2 Hz operation at high energy show a very good agreement with an averaged beam diameter of ≈ 7 mm (FWHM). No real "hot-spots" are detectable. The mean fluence in both cases is 1.4 J/cm^2 with a maximum value of 2.5 J/cm^2 .

The evaluation of the measured wavefronts via *Zernike*-polynomials revealed a change of the ROC from -34 m at 1 Hz operation to 27 m at 2 Hz, see Figure 9.5 c) & d). So, in both cases the beam is nearly collimated which was achieved by adapting the distance of the imaging optics in such a way that the unamplified beam out of the tube diverges and thus pre-compensates for the focusing thermal lens.

9.3 Summary of the "high-energy" campaign

- the main achievement of the "high-energy" campaign is the amplification of the laser pulses to energies >1 J with a pulse-to-pulse stability of 1.5% rms at 1 Hz and 2 Hz repetition rate
- while amplification the full spectral bandwidth is maintained and the pulses were compressed to a close-to-*Fourier*-limit pulse duration of ≈ 740 fs (FWHM)
- under consideration of the pulse shape, the peak power of the pulse is calculated to ≈ 1 TW for 1 Hz operation and 2 Hz operation.
- so, to our knowledge, we built the first diode-pumped, Yb:YAG CPA-system generating 1 TW pulses

Part VI

FUTURE AMPLIFIERS

CONCEPT FOR A ≥ 10 J-AMPLIFIER

As mentioned in the very beginning, also amplifiers delivering ≥ 10 J are needed for the final operation of the PFS. In this chapter possible amplifier and crystal designs for a ≥ 10 J-amplifier, developed using the experiences gathered with 1 J-stage and further scaling considerations, are presented.

10.1 Pump modules for the 10 J-amplifier

The pump engine for the 10 J-amplifier was developed according to our specifications by *Las-tronics GmbH* in Jena. It consists of two pump modules, each delivering a net output power of 43.5 kW, which can be combined via polarization coupling. The typical degree of polarization of the built-in laser diodes is 92% leading to a maximum peak power of 80 kW after combination at a maximum duty cycle of 1.5%. By the use of micro-lens beam homogenizers, see Section 7.1, a square spot size of $20 \times 20 \text{ mm}^2$ is generated at a working distance of 150 mm after the last imaging lens. Analogously to the pump modules of the other amplifiers the center pump wavelength is 940 nm and can be adjusted via the cooling temperature. A photograph of the pump engine and the pump beam profile in the combined case are depicted in Figure 10.1.

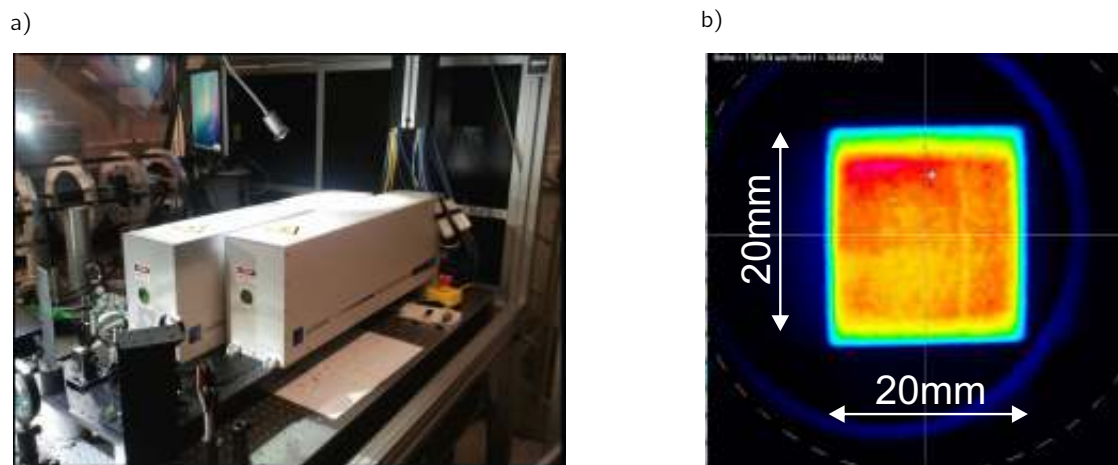


Figure 10.1: Pump engine for the 10 J-amplifier. Two pump modules a), each delivering a net output power of 43.5 kW, can be combined via polarization to achieve a total output power of 80 kW on square size of $20 \times 20 \text{ mm}^2$ at a working distance of 150 mm after the last imaging lens b).

The brightness of the modules according to the specifications is $0.5 \text{ W/cm}^2 \text{sr}$ with a maximum divergence angle of 4° in both directions in the image plane. This enhanced brightness should help to realize one of the two multi-pass pumping concepts presented in the following.

The first idea is known from thin-disk laser heads [75]. Parabolic and turning mirrors are used to realize imaging multi-pass pumping. The principle and a thinkable design for the 10 J-amplifier are shown in Figure 10.2.

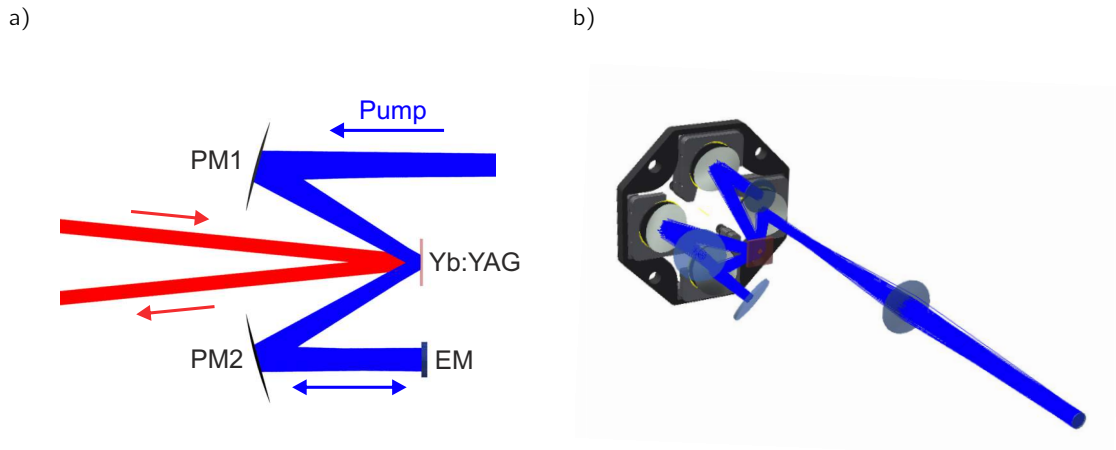


Figure 10.2: Multi-pass pumping setup with parabolic mirrors. Subfigure a) shows the principle of this pump scheme. 2 parabolic mirrors (PM) and one end-mirror (EM) are used to establish 4 pump passes in this case. A 3D arrangement thinkable for the 10 J-stage is illustrated in b). It comprises 4 parabolic mirrors and three folding mirrors allowing for 8 pump passes through the Yb:YAG crystal.

As depicted in Figure 10.2 a), the pump radiation impinges on a larger AOI compared to the laser beam. This large angle in combination with thick crystals might result in an inhomogeneous pump beam profile and therefore has to be verified in the beginning.

Alternatively, the multi-pass pumping can be realized with one big lens [76] instead of the parabolic mirrors. The principle and a possible design for the 10 J-amplifier are shown in Figure 10.3.

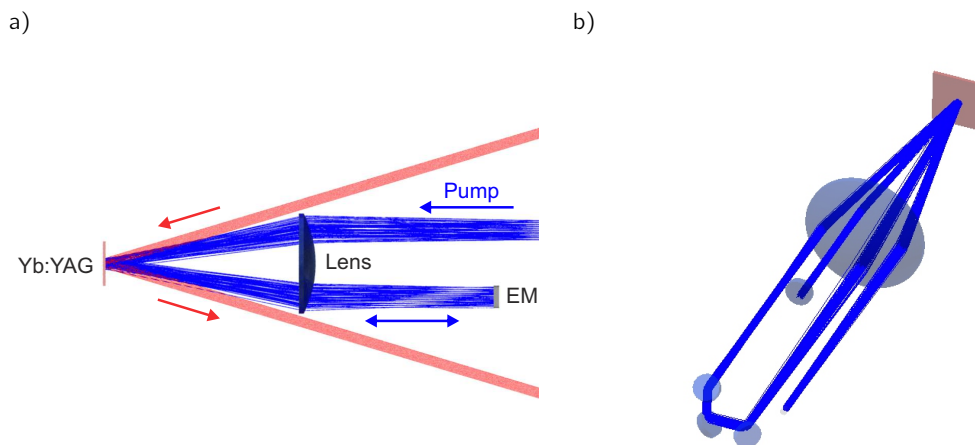


Figure 10.3: Multi-pass pumping setup with a big lens. Subfigure a) shows the principle of this pump scheme. A big lens and one end-mirror (EM) are used to establish 4 pump passes in this case. A 3D arrangement thinkable for the 10 J-stage is illustrated in b). It comprises 4 passes through the common lens and three folding mirrors allowing for 8 pump passes through the Yb:YAG crystal. For a better visibility the pump beam size was reduced for illustration.

In this case, the incidence angle of the pump radiation can be smaller compared to multi-pass pumping with parabolic mirrors. On the other hand, the fact that angles for the laser beam are larger compared to the pump might lead to a non-uniform beam profile after amplification.

10.2 Amplifier design for a 10 J-stage

As mentioned before, the amplifier design for the 10 J-stage will be an adapted version of the 1 J-amplifier. The key design issue is that due to the larger beam size of ≈ 20 mm (FWHM) larger optics (1.5") are necessary while at the same time the outer diameter of the vacuum tube should stay 320 mm. Under consideration of the size of the mirror mounts only octagonal carrier rings, see inset Figure 10.4, are possible. Thus, the number of amplification passes is limited to $2 \times 3 \times 2 = 12$.

The design sketch for a 10 J-stage, developed considering the experiences with the 1 J-design, is shown in Figure 10.4. A drawback of the 1 J-design was the difficulty to access the optics located in the second image plane. Therefore, an additional folding mirror (FM2) is used analogous to FM1 in the 10 J-design allowing for fast access of the second imaging plane as well.

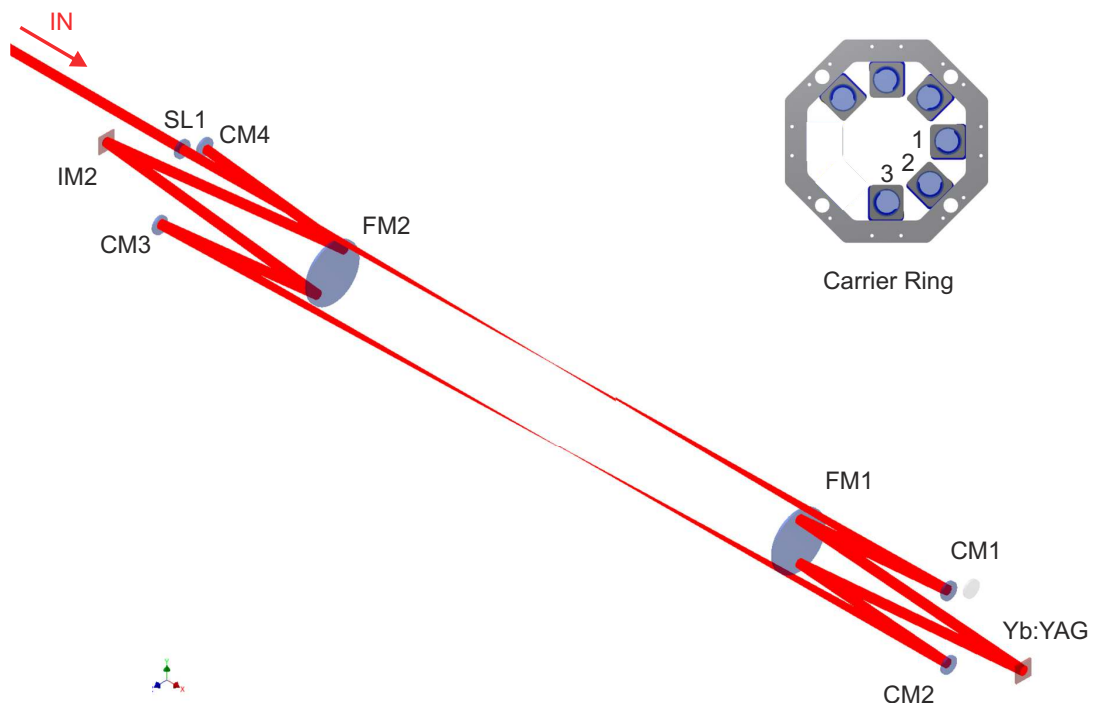


Figure 10.4: Design sketch for a 10 J-amplifier based on the experiences gained with the 1 J-design. According to the size of the mirror mounts necessary for 10 J-pulses octagonal carrier rings are feasible when considering a diameter of 320 mm for the vacuum tube. Furthermore, a second folding mirror (FM2) is implemented which guarantees accessibility also for the second image plane (IM2). In the illustration, the beam path for the first amplification plane is highlighted. The subfigure illustrates a carrier ring capable of mounting 8 1.5" mirrors. Analogously to the mechanical design of the 1 J-amplifier all optics are mounted on carrier rings which itself sit on carrier rails, see Figure 7.15.

During the implementation of the 1 J-stage, the dichroic pump mirror necessary due to the short working distance of the pump module proved to be a bottle neck in terms of damage threshold and transmission under vacuum conditions. As presented, according to the enhanced brightness of the 80kW pump engine, such a dichroic mirror is not necessary for the 10 J-stage. However, the presented pump solutions have to be verified and adapted to the new amplifier design.

10.3 Yb:YAG design considerations

In terms of the Yb:YAG crystal design, the same considerations as for the 1 J-amplifier apply. The main goal is to minimize the the crystal thickness in order to optimize the heat extraction while at same time the transverse gain should be kept small in order to minimize parasitic effects.

The main result of the experiments with the 1 J-stage was that under consideration of the given pump parameters parasitic effects starts to occur at a doping concentration of >2% which was expected since the transverse gain including reabsorption in the unpumped area exceeds the limit for the onset of parasitic oscillations in this cases, see Section 2.5. However, the drop in gain caused by parasitic oscillations was not expected to be that severe. This issue was mitigated by adding additional absorber length, i.e. using the larger 2% \times 6 \times 40 Au1 crystal. Thus, the onset of parasitic oscillations was effectively suppressed leading to higher output energies.

Hence, the suppression of parasitic oscillations is a key aspect for designing the crystals for the 10 J-stage. One solution is to taper the edges of the crystal under a certain angle. For Yb:YAG one calculates $28.43^\circ \leq \beta \leq 33.33^\circ$ [77]. Doing so, the transverse ASE is effectively reflected out of the crystal through the AR-coated front surface. Another possibility, known from Ti:Sa lasers, is to use an refractive index matched absorber fluid surrounding the crystal [78]. In this case, the ASE will not undergo *Fresnel*-reflection at the crystal edge and can effectively be absorbed in the fluid. A new technology developed in the last years and now commercially available is to use Cr⁴⁺ co-doped YAG claddings to absorb the ASE [68]. This is from particular interest since the absorber can be directly co-sintered to ceramic Yb:YAG which is the only alternative when large beam diameters and thus crystal diameters in the order of several cm are required.

However, despite this possibilities for effective suppression of the ASE there is a upper limit for the transverse gain. At a certain gain just a single pass of the spontaneously emitted photon across the longest path through the pumped area is enough to seriously deplete the inversion. Assuming the ASE fluence being equal to saturation fluence one calculates [79]:

$$\left[4 (\log G_0^2)^{1/2} \right] / G_0 \geq \Omega \quad (10.1)$$

Here Ω is the maximum solid angle in which the spontaneous photons can be emitted. In our case ($D_{pump} \approx 2$ cm, thickness ≈ 1 cm) the maximum Ω calculates to ≈ 0.2 leading to a maximum $G_0 = \exp(4)$. This is in excellent agreement with the measurements 2% \times 6 \times 40 crystal assembly, see Chapter 8, where $G_0 \approx \exp(4)$ is reached when pumping with 2000 μ s at 6 $^\circ$ heat sink temperature and first evidences of this effect are found. *D. Albach et al.* investigated comparable Yb:YAG crystal assemblies specifying $G_0 \leq \exp(4)$ as the upper limit for the transverse gain as well [45, 51].

As an example, the absorption of a 0.25% Cr⁴⁺-doped cladding was measured to be $\alpha = -5.5 \text{ cm}^{-1}$ at 1030 nm [45]. Taking the reflectivity of 0.09 for the air/YAG interface into account, see Section 2.5, the thickness of of the Cr⁴⁺-doped cladding calculates to ≥ 1.5 mm in order to absorb enough radiation that at a transverse gain of $G_0 = \exp(4)$ in the pumped area the net gain remains below unity, see Section 2.5.

So, under assumption of a existing absorber solution for the ASE the design parameter for the transverse gain for the 10 J-stage is set to $G_0 = \exp(4)$. As described above, further design parameters for the crystals are a pump power of 80 kW on a square spot size of 20 \times 20mm² with maximum 8 pump passes and 12 amplification passes with a seed energy of 1 J. According to the experiences with the 1 J-stage the pump pulse duration is assumed to be 1500 μ s and the crystal temperature is 300 K.

In the following the simulation results for three different disk approaches obtained with the above mentioned parameters are presented.

10.3.1 Single-disk design

In analogy to the 1 J-stage the first simulated design is a single disk. A quick estimation, assuming twice the pump intensity ($\approx 20 \text{ kW/cm}^2$) and diameter ($d_{\text{Pump}} = 2 \text{ cm}$) compared to the 1 J-amplifier leads to a maximum doping concentration of 0.5% for the 10 J-stage. Thus, also a ≈ 4 times longer absorption path for the pump radiation, i.e. crystal thickness, is necessary. The results of the full simulation - the maximum transverse gain, i.e. in the surface layer of the disk, and the output energy depending on the crystal thickness - of a single disk pumped either with 2, 4 or 8 passes are shown in Figure 10.5. Also depicted for comparison are results for higher doping concentrations. Again, the energy drop after the ideal thickness is due to reabsorption in the depth of the crystal. As mentioned, this simulation excludes the effects of gain depletion by transverse effects.

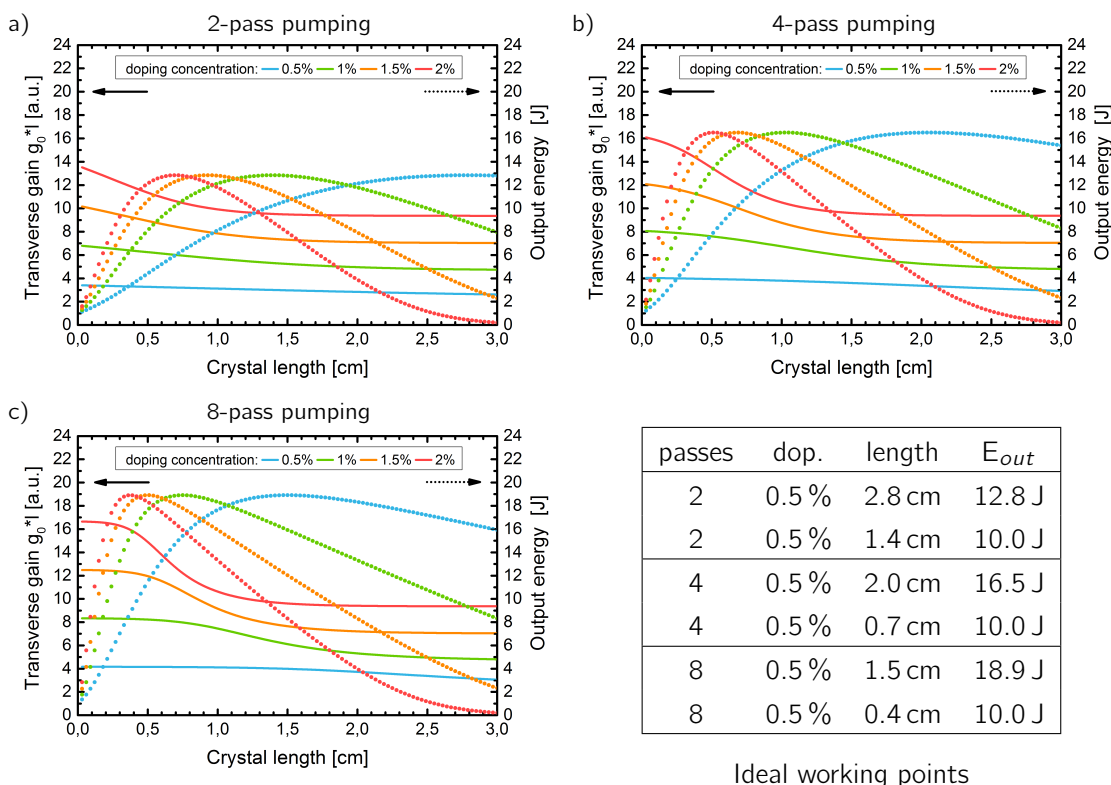


Figure 10.5: Simulation results for a 10 J+ single-disk amplifier assuming a pump power of 80 kW on a square pump spot of $20 \times 20 \text{ mm}^2$. The straight lines represent the transverse gain, the dotted lines the possible output energy. In order to limit $g_0 D \leq 4$ the doping concentration should not exceed 0.5% as can be seen from the blue solid lines. The ideal crystal thickness and the corresponding output energies as well as the necessary thickness to achieve 10 J are summarized in the table. Going from 2 to 8 pumping passes the output energy at 0.5% doping level can be increased by $\approx 50\%$. However, in this case the crystal thickness 2.5-fold larger than in the 1 J-amplifier. (Simulation parameters as summarized on page 88)

The simulation results for pumping with 80 kW on a square pump spot of $20 \times 20 \text{ mm}^2$ show that the doping concentration should not exceed 0.5% in order to guarantee $g_0 D \leq 4$. As shown in Figure 10.5 the maximum output energy can be increased from 13 J up to 19 J by going from 2 to 8 pump passes while at the same time the minimum crystal thickness can be reduced by almost a factor of two. The maximum output energy of $\approx 19 \text{ J}$ while staying below the limit $g_0 D \leq 4$ can be extracted in 12 amplification passes from a 0.5%-doped Yb:YAG disk pumped in 8 passes. However, the crystal thickness in this case is calculated to 1.5 cm which might be too large for effective heat removal according to the experimental experience with the 1 J-stage, especially if one takes into account the higher pump fluence.

10.3.2 Double-disk design

In order to resolve the cooling problem, in the following we will investigate a double disk approach. Instead of one thick Yb:YAG crystal two individual crystals located in the 2 imaging planes of the amplifier are used. So, instead of 80 kW on a single crystal, two Yb:YAG crystals will be pumped with 43.5 kW each on a square pump spot of $20 \times 20 \text{ mm}^2$. This should allow for a doping level of 1% and hence a reduced crystal thickness improving the heat removal.

For the simulations, all other parameters are identical to the ones used for the 80 kW single-disk approach. Figure 10.6 summarizes the obtained simulation results where the transverse gain corresponds to a single disk and the output energy is calculated for both disks.

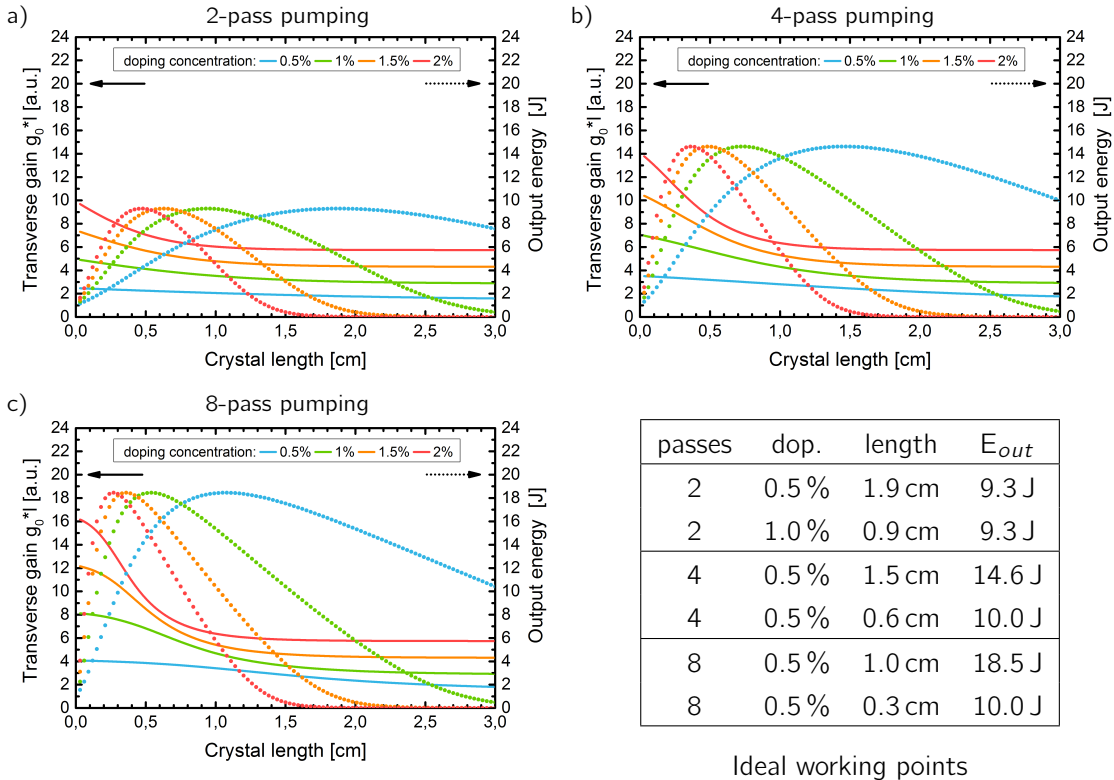


Figure 10.6: Simulation results for a 10 J+ double-disk amplifier assuming a pump power of 43.5 kW on a square pump spot of $20 \times 20 \text{ mm}^2$ for each disk. The straight lines represent the transverse gain of a single crystal, the dotted lines the possible output energy amplifying with both disks. The ideal crystal thickness and the corresponding output energies as well as the necessary thickness to achieve 10 J are summarized in the table. The main result is that comparable energies to the single-disk design can be extracted. In case of 8 pass pumping the output energy of 18.5 J is comparable to a single-disk at the reduced crystal length of 1 cm. Generally, the calculated crystal length for maximum output energy in the double-disk design are 33% shorter compared to the a single-disk reducing the thermal issues significantly. (Simulation parameters as summarized on page 88)

The simulation shows that the above given estimate of 1% to stay below the limit $g_0 D \leq 4$ is only practical for 2-pass pumping. For 4 and 8 pump passes the maximum doping level is 0.5%. Nevertheless, the double-disk simulations yields 33% shorter crystal thickness compared to the single-disk approach in order to get the maximum output energy. Furthermore, in case of 2 0.5%-doped disks pumped with 8 passes the output energy of 18.5 J is nearly identical to the single-disk design but at the reduced crystal thickness of 1 cm.

Thus, utilizing two disks pumped with half the intensity is a promising alternative to mitigate thermal issues. A back-of-the-envelope calculation yields a ≈ 3 times higher repetition rates compared to the single disk design. However, to realize this approach another folding mirror is necessary, see Figure 10.4, which can introduce additional stability issues.

Remark to the single- and double-disk designs

For the single- and double-disk calculations the design parameter was $g_0D \leq 4$. This limit is valid for all crystal temperatures. So, the idea to utilize shorter crystals - to improve the heat removal - with the same doping concentrations as presented at lower crystal temperatures leads to $g_0D \geq 4$ due to the higher emission cross section. The only way to keep $g_0D \leq 4$ at lower heat sink temperatures would be a lower doping concentration which at the end leads to lower output energies at the same crystal thickness.

10.3.3 Multi-slab design

Another promising approach in order to enhance the cooling of the crystal(s) is the multi-slab design where the big crystal is cut into several slabs which are cooled via a gas-flow. Within the *Mercury* project 50 J pulses at 10 Hz repetition were generated using the multi-slab architecture [15]. Recently the design was "revived" by the *Dipole* project showing 6 J pulses at 10 Hz repetition rate [24].

So, concerning our results with the thick-disk approach the multi-slab design seems to be the only architecture capable of delivering Joule-class pulses at 10 Hz repetition rate.

Unfortunately, this design comes along with tremendous financial and constructional efforts. A special high-pressure vessel to mount the crystal is needed which has to be designed and constructed precisely in order to get the adequate gas flow between the disks. Furthermore, an elaborate cooling system is needed to remove the heat at low temperature and high pressure.

Nevertheless, this design is investigated using our simulation tool. In analogous to *Dipole* 4 slabs each 0.5 cm thick will be pumped from both sides with 43.5 kW in our case. We assume room-temperature as "working point" which should simplify the cooling system. All other pump and amplification parameters are according to the single-disk, double-disk approach resp.. Figure 10.7 shows the output energies in dependence of the doping level of the individual slabs. For the simulation the doping level of both outer slabs and both inner slabs were the same.

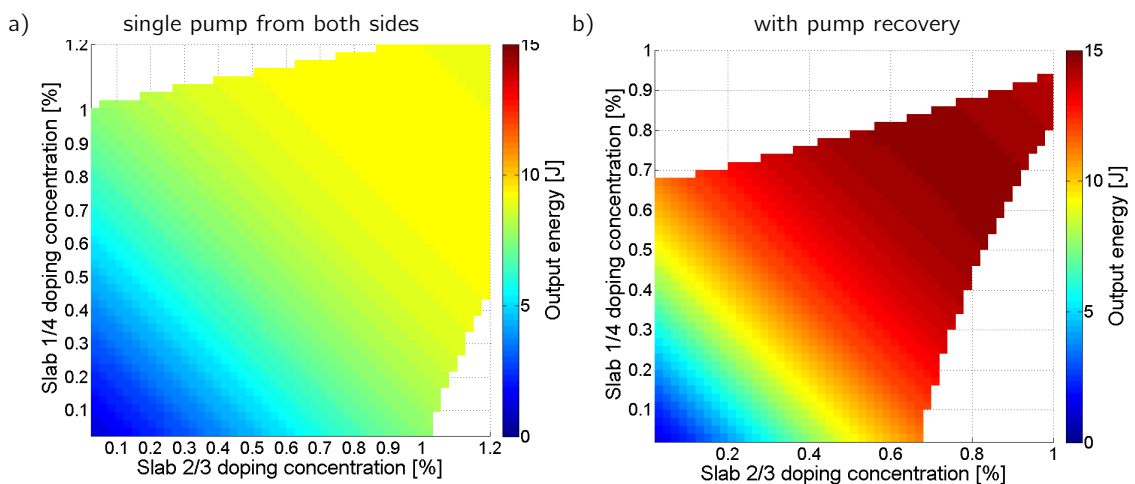


Figure 10.7: Simulation results for a 10 J+ multi-slab amplifier. The calculations were performed under consideration of pumping from both sides single-pass a) or with pump recovery b) (2-pass pump). Simulation results revealing a $g_0D > 4$ in any of the slabs are excluded. The output energy is calculated in dependence of the doping concentration of the slabs 1/4 & 2/3. Under single-pumping a maximum output energy in the range of 9 J can be extracted in 12 amplification passes. The output can be raised to 14 J when the pump light is recovered. However, the variation of the doping level between the slabs 1/4 & 2/3 does not lead to a major increase of the output energy compared to all slabs having the same doping concentration.

The simulation produces results comparable to the double-disk approach. Under single-pass pumping from both sides a maximum output energy in the range of 9 J is calculated which can be raised by pump light recovery to ≈ 14 J. The maximum energy in both cases is found for all slabs having the same doping concentration which is 1% in the single-pass and 0.8% if pump recovery is considered. However, there is a variation range for the doping concentrations which could be used to unify the generated heat in the individual slabs.

In conclusion, under the given pump and amplification parameters, output energies in excess of 10 J are possible either with a single disk, a double disk or a multi-slab design. In order to experimentally find the optimal solution 0.5%- and 1%-doped crystals with different thickness will be ordered and tested in the near future.

Part VII

SUMMARY AND OUTLOOK

SUMMARY & OUTLOOK

11.1 Summary

The work for this dissertation was done in the framework of the Petawatt Field Synthesizer at the Max-Planck-Institute for Quantum Optics with the aim of developing, investigating and implementing amplifiers based on Yb-doped materials for the PFS CPA pump laser. The main objective was to set up an amplifier chain generating stretched pulse energies in the 1 J-range while maintaining a spectral bandwidth allowing for a compressed pulse duration <1 ps.

The initial work was done on close collaboration with *S. Klingbiel* who's main task was to design and implement the stretcher-compressor setup for the PFS CPA pump chain and to investigate the timing jitter introduced by such a system [9, 61]. Together, a regenerative amplifier based on diode-pumped Yb:FP15-glass was set up amplifying the stretched 4 ns-pulses to a pulse energy of 150 μ J with an amplified bandwidth of 4.5 nm at 10 Hz repetition rate, see Section 6.3. With the subsequent diode-pumped Yb:YAG 8-pass amplifier the pulses were amplified to 300 mJ at 10 Hz repetition rate, see Section 6.4. By utilizing spectral amplitude shaping introduced with a *Dazzler*, a spectral bandwidth of 3.8 nm was amplified enabling the compression of the pulses to pulse durations ≤ 1 ps [10]. By that time, these were unique parameters for a Yb:YAG CPA system and shorter pulse durations have not been reported yet for comparable systems. However, it turned out that the output beam profile of the multi-pass amplifier had to be improved to serve as seed for the next amplification stages which lead to a reduced pulse energy of 220 mJ. Further optimization finally allowed to compress the pulses down to their *Fourier*-limit of 720 fs, see Section 6.5.

Despite these outstanding results, the architecture of this amplifier proved to be a one-off prototype due to the strong thermal lensing in the Yb:YAG crystal and thus this scheme could not serve as a model for upscaling. Thus, for the subsequent 1 J-amplifier a novel architecture - featuring an active-mirror Yb:YAG approach to minimize the thermal lensing and built in a 20-pass relay-imaging configuration to improve the beam profile and enhance the efficiency - was developed with the help of optical design software, see Section 7.3. The analysis of this amplifier architecture showed its excellent properties in terms of wavefront aberrations and its capability of compensating thermal lensing. An additional merit of the design is its rotational symmetry which enables to fit the whole setup into the vacuum tube necessary due to the high intensities in the intermediate foci.

Another issue if considering amplification to >1 J is the necessary large beam diameter determined by the laser induced damage threshold of the used optics in combination with the demanded high single-pass gain which can lead to strong amplified spontaneous emission and trigger parasitic oscillations decreasing the overall gain significantly, see Section 2.5. To investigate this, several Yb:YAG crystal differing in doping concentration, thickness and size were purchased. Furthermore, due to the lack of a commercial solution an own glueing technology was developed in order to realize the active-mirror approach with the purchased crystals, see Section 7.2.

After the implementation of the 20-pass relay-imaging amplifier in the laboratory it was used to map the performance envelope of the different crystal assemblies - the "low-energy" campaign presented in Chapter 8. The amplification performance was investigated in dependence of the pump pulse duration, the heat sink temperature and the repetition rate at low seed energies. The developed amplification code, see Chapter 5, was used to perform a regression analysis of the measured data. In the course of this campaign it turned out that parasitic effects/oscillations strongly decrease the overall gain if the doping concentration exceeds 2% at the set pump parameters of 11 kW on $10 \times 10 \text{ mm}^2$ and pump pulse durations $>1000 \mu\text{s}$. The enhancement of these effects when decreasing the heat sink temperature and/or increasing the pump pulse duration was confirmed. Furthermore, an influence of the the used glue and the heat sink coating of the crystal assemblies to the amplification was found. Using glue #1 lead to less gain losses when switching to a higher repetition rates which is an indication that even at this thin glue layers the thermal conductivity of the glue plays a major role for the heat removal. The gold-plated heat sinks enhance parasitic effects/oscillations which can be explained by higher reflectivity of gold compared the nickel at the lasing wavelength. Additionally, the benefit of a larger unpumped area which enhances the absorption of the amplified spontaneous emission was shown and thus the 2%-doped $6 \text{ mm} \times 40 \times 40 \text{ mm}^2$ crystal was chosen to be used for the "high-energy" campaign. Moreover, the repetition-rate depended measurement of the beam profile and wavefront proved the beneficial effects of the active-mirror approach. Even when pumped at 5 Hz the thermal lensing is reduced drastically and the deterioration of the wavefront is small.

In the beginning of the "high-energy" campaign, see Chapter 9, further preparatory measurements were performed to investigate the evolution of the beam profile during amplification and moreover to adjust the spectral shaping in order to amplify the broadest bandwidth possible. These measurements also revealed that long-term operation at $>5 \text{ Hz}$ repetition rate is not possible at the moment due to a not compensable thermally induced beam drift. Furthermore, stress-induced wavefront aberrations at low heat sink temperatures lead to severe changes of the beam profile also prohibiting long-term high-energy operation. However, the full amplification performance was measured for 1 Hz and 2 Hz repetition rate at a heat sink temperature of $20 \text{ }^\circ\text{C}$. For both repetition rates, the goal of 1 J pulse energy - low enough not to risk any damage of the optics and thus allow for multiple measurements - was realized. While a seed energy of 60 mJ is needed to generate 1 J output energy at 1 Hz repetition rate, the seed energy had to be increased to 70 mJ at 2 Hz. Furthermore, the measurements revealed a pulse-to-pulse stability of $\sigma \leq 1.5\%$ at 1 J output energy for both repetition rates. The regression analysis of the measured amplification slopes even predicts possible output pulse energies $>1.1 \text{ J}$ when using the maximum seed energy of 90 mJ. The measured near beam profiles at 1 J show no "hot-spots" and are more "flat-top"-like compared to the input beam profile which is beneficial for highest frequency-doubling and OPCPA efficiencies. By pre-compensating the thermal lens with the imaging setup, the output beam is nearly collimated and the wavefront aberrations were measured to be $<\lambda/2$. Due to the spectral shaping no spectral components are lost during amplification. The amplified spectra at 1 Hz and 2 Hz are nearly identical to the seed spectra. Finally, the *FROG* analysis of the compressed 1 J-pulses revealed a close-to *Fourier*-limit pulse duration of 740 fs. Under consideration of the measured compressor transmission (76%), the maximum compressed pulse energy is calculated to be 0.8 J and 0.78 J for 1 Hz and 2 Hz, respectively. Thus, the pulse power (transmitted energy/pulse duration (FWHM)) is calculated to 1.08 TW for 1 Hz and 1.05 TW for 2 Hz. Using a more refined analysis which takes the retrieved temporal pulse shape into account leads to a pulse peak power 0.96 TW for 1 Hz and 0.92 TW for 2 Hz operation.

To our knowledge, comparable pulse parameters are not reported in the literature so far and thus we generated for the first time 1 TW pulses in a diode-pumped Yb:YAG CPA-system [80]. This, in addition to the excellent beam parameters, make the system an excellent pump source for highly-efficient, ultra-broadband optical parametric chirped pulse amplification.

11.2 Outlook

To prove the feasibility of the PFS concept, a first study of 1-2 ps optical parametric chirped pulse amplification was carried out in 2011 using the compressed and frequency-doubled pulses out of the 8-pass Yb:YAG amplifier. *C.Skrobel et al.* showed the amplification of the optically synchronized seed pulses in the wavelength range between 830 - 1310 nm using a 7 mm thin DKDP crystal [57]. Furthermore, the amplified spectrum should allow for a compressed pulse duration of ≈ 6 fs. "These findings confirm the reliability of our theoretical modelling in particular with respect to the design for further amplification stages, scaling the output peak powers to the petawatt scale." [57]

However, the timing jitter between the seed and the pump pulses proved critical in their measurements. As mentioned before, *S. Klingebiel* investigated this timing jitter experimentally and theoretically [61]. His conclusion was that the stretcher and compressor has to be set up in air-tight or vacuum housings to improve the measured jitter of ≈ 100 fs in the actively-stabilized case. While the housing of the stretcher in an air-tight perspex box was a comparable easy task the construction of the vacuum chambers requires much more financial and design effort. At the moment, these vacuum chambers are set up in the laboratory and after the completion the compressor will be inserted. Furthermore, additional changes in the beam delivery system are currently being implemented in order to use the 1 J output of the CPA pump chain for pumping the OPCPA.

In parallel, the design of the 10 J amplification stage, see Chapter 10, is ongoing. Two 43.5 kW pump modules were already purchased and are ready-to-use in the laboratory as well as the mechanical parts and optics. The main bottle-neck are the Yb:YAG ceramics. At the moment we are surveying possible suppliers who can deliver the needed Yb:YAG ceramics with the mentioned Cr^{4+} co-doped cladding. The procurement is estimated to take at least 4 month. However, first test of the setup and the amplification will be carried out with a spare 2%-doped $6\text{mm} \times 40 \times 40\text{mm}^2$ crystal in the near future.

The results of this thesis work - 1 TW pulses generated in a diode-pumped Yb:YAG CPA system - does represent a milestone for the HEC-DPSSL community. Moreover, this system when used as pump source for OPCPA will boost the PFS-project to a new level. Though not yet fully operational, the PFS recieved great attention in the whole laser community due to its prospect for generating energy-scalable, few-cycle pulses with an inherently high contrast. This also led to the creation of a follow-up - named *PFS-pro* - which is built at the *Laboratory for Extreme Photonics (LEX)* [81]. In contrast to PFS, *PFS-pro* focuses on high average power in the 100's of Watt-range utilizing kHz Yb:YAG thin-disk lasers as pump source. Furthermore, PFS/*PFS-pro* technology will be deployed in the European *Extreme Light Infrastructure (ELI)* project - "for the investigation of light-matter interactions at highest intensities and shortest time scales" [82] - which will constitute of 3 major research facilities currently established in Hungary, Romania and the Czech Republic. However, since the mentioned projects aim on lower pulse energies, the original PFS - using the developed 1 TW CPA pump laser and its upgrades - might stay a unique system in terms of high-energy, high-contrast pulses.

Part VIII

APPENDIX

VERIFICATION OF THE CONSTANT M_{ASE} APPROACH

As described in Section 2.5, *Barnes and Walsh* [34] derived a correction term to calculate possible losses through parasitic effects while pumping the gain medium. The equation for the calculation of the time-dependent upper-level population then reads to:

$$\frac{dn}{dt} = W_P (N - n) - \frac{n}{\tau_f} \exp(\sigma_{ASE} n L_{char}) \quad (\text{A.1})$$

This equation has to be solved numerically which can lead to calculation-time issues in the later simulation. Alternatively, one can approximate $\exp(\sigma_{ASE} n L_{char})$ by a constant factor called M_{ASE} and so the equation can be solved analytically to:

$$n(t) = \frac{\tau_f W_P}{\tau_f W_P + M_{ASE}} N \left(1 - e^{-t \left(W_P + \frac{M_{ASE}}{\tau_f} \right)} \right) \quad (\text{A.2})$$

To verify the commutability of both equations, the calculated upper-state populations are compared, as shown in Figure A.1. For the calculations, a doping concentration of 2% Yb:YAG is assumed. According to [39] the $\sigma_{ASE} = 2.25e-20 \text{ cm}^2$ which is the emission cross section for Yb:YAG at 1030 nm at room-temperature. τ_f is set 1 ms [36]. At first the inversion is calculated via Equation A.1 assuming a certain L_{char} . Secondly, M_{ASE} in Equation A.2 is adapted in such a way that a good agreement with the long-term results of Equation A.1 is achieved. This procedure was chosen since pump pulse durations longer than τ_f are foreseen.

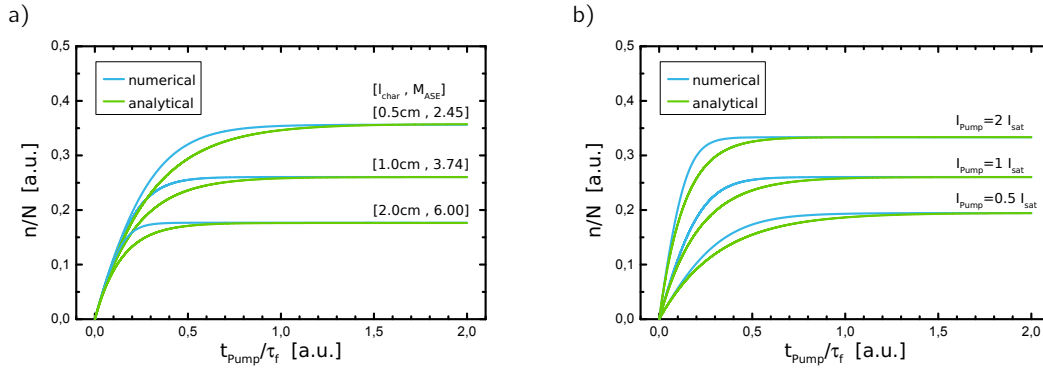


Figure A.1: Comparison of the numerical and analytical solution for the calculation of the upper-state population including ASE. Subfigure a) illustrates the difference of both solutions at $I_P = I_{sat}$ for different L_{char} . In subfigure b) the characteristic length was set to 1 cm and the pump intensity was varied. For all cases a M_{ASE} could be found so that Equation A.2 equals Equation A.1 for pumping times in the order of τ_f and above. However, for shorter pumping times a mean maximum deviation of between both models is 15%. For the calculations, a doping concentration of 2% Yb:YAG is assumed. According to [39] the $\sigma_{ASE} = 2.25e-20 \text{ cm}^2$ which is the emission cross section for Yb:YAG at 1030 nm at room-temperature. τ_f is set 1 ms [36].

According to Figure A.1, for all considered cases a M_{ASE} could be found so that Equation A.2 equals Equation A.1 for pumping times in the order of τ_f and above. However, for shorter pumping times a mean maximum deviation of between both models is 15%.

So, in conclusion, if the considered pump pulse durations are larger than τ_f - which is true in our case - the constant M_{ASE} equation can be used to calculate the inversion.

BIBLIOGRAPHY

- [1] G. Cerullo and S. De Silvestri, "Ultrafast optical parametric amplifiers," *Review of Scientific Instruments*, vol. 74, no. 1, p. 1, 2003. [Online]. Available: <http://link.aip.org/link/RSINAK/v74/i1/p1/s1&Agg=doi>
- [2] D. Strickland and G. Mourou, "Compression of amplified chirped optical pulses," *Optics Communications*, vol. 56, no. 3, pp. 219–221, 1985. [Online]. Available: <http://www.sciencedirect.com/science/article/pii/0030401885901208>
- [3] G. D. Tsakiris, K. Eidmann, J. Meyer-ter Vehn, and F. Krausz, "Route to intense single attosecond pulses," *New Journal of Physics*, vol. 8, pp. 19–19, Jan. 2006. [Online]. Available: <http://stacks.iop.org/1367-2630/8/i=1/a=019?key=crossref.65a890ec861c69659d7da6087740162d>
- [4] P. Heissler, R. Hörlein, J. M. Mikhailova, L. Waldecker, P. Tzallas, a. Buck, K. Schmid, C. M. S. Sears, F. Krausz, L. Veisz, M. Zepf, and G. D. Tsakiris, "Few-Cycle Driven Relativistically Oscillating Plasma Mirrors: A Source of Intense Isolated Attosecond Pulses," *Physical Review Letters*, vol. 108, no. 23, p. 235003, Jun. 2012. [Online]. Available: <http://link.aps.org/doi/10.1103/PhysRevLett.108.235003>
- [5] M. Geissler, J. Schreiber, and J. Meyer-ter Vehn, "Bubble acceleration of electrons with few-cycle laser pulses," *New Journal of Physics*, vol. 8, no. 9, pp. 186–186, Sep. 2006. [Online]. Available: <http://stacks.iop.org/1367-2630/8/i=9/a=186?key=crossref.872c88a1bafa2f3f692eeee0f6909f2ce>
- [6] A. Buck, M. Nicolai, K. Schmid, C. M. S. Sears, A. Sävert, J. M. Mikhailova, F. Krausz, M. C. Kaluza, and L. Veisz, "Real-time observation of laser-driven electron acceleration," *Nature Physics*, vol. 7, no. 7, pp. 543–548, Mar. 2011. [Online]. Available: <http://www.nature.com/doi/10.1038/nphys1942>
- [7] D. Herrmann, L. Veisz, R. Tautz, F. Tavella, K. Schmid, V. Pervak, and F. Krausz, "Generation of sub-three-cycle, 16 TW light pulses by using noncollinear optical parametric chirped-pulse amplification," *Optics Letters*, vol. 34, no. 16, p. 2459, Aug. 2009. [Online]. Available: <http://ol.osa.org/abstract.cfm?URI=ol-34-16-2459>
- [8] Zs. Major, S. A. Trushin, I. Ahmad, M. Siebold, C. Wandt, S. Klingebiel, T.-J. Wang, J. A. Fülöp, A. Henig, S. Kruber, R. Weingartner, A. Popp, J. Osterhoff, R. Hörlein, J. Hein, V. Pervak, A. Apolonski, F. Krausz and S. Karsch, "Basic concepts and current status of the Petawatt Field Synthesizer - a new approach to ultrahigh field generation," *Rev. Laser Eng.*, vol. 37, pp. 431–436, 2009.
- [9] S. Klingebiel, "Picosecond pump dispersion management and jitter stabilization in a petawatt-scale few-cycle OPCPA system," Dissertation, LMU München, 2013.
- [10] S. Klingebiel, C. Wandt, C. Skrobel, I. Ahmad, S. A. Trushin, Z. Major, F. Krausz, and S. Karsch, "High energy picosecond Yb:YAG CPA system at 10 Hz repetition rate for pumping optical parametric amplifiers," *Optics Express*, vol. 19, no. 6, p. 5357, Mar. 2011. [Online]. Available: <http://www.opticsexpress.org/abstract.cfm?URI=oe-19-6-5357>
- [11] B. Reagan, A. H. Curtis, K. Wernsing, F. J. Furch, B. M. Luther, and J. J. Rocca, "Development of High Energy Diode-Pumped Thick-Disk Yb:YAG Chirped-Pulse-Amplification Lasers," *IEEE Journal of Quantum Electronics*, vol. 48, no. 6, pp. 827–835, Jun. 2012. [Online]. Available: <http://ieeexplore.ieee.org/lpdocs/epic03/wrapper.htm?arnumber=6184266>

- [12] "Thales Alpha Datasheet." [Online]. Available: http://www.thalesgroup.com/Markets/Security/What_we_do/Industry_and_Finance/Manufacturing_industry/Lasers/Documents_-_Lasers/ALPHA_10-August_2012/
- [13] V. V. Lozhkarev, G. I. Freidman, V. N. Ginzburg, E. V. Katin, E. a. Khazanov, a. V. Kirsanov, G. a. Luchinin, a. N. Mal'shakov, M. a. Martyanov, O. V. Palashov, a. K. Poteomkin, a. M. Sergeev, a. a. Shaykin, and I. V. Yakovlev, "Compact 0.56 Petawatt laser system based on optical parametric chirped pulse amplification in KD*P crystals," *Laser Physics Letters*, vol. 4, no. 6, pp. 421–427, Jun. 2007. [Online]. Available: <http://stacks.iop.org/1612-202X/4/i=6/a=003?key=crossref.b360373a803c9dc5192641f4d4556273>
- [14] R. Paschotta, *Encyclopedia of Laser Physics and Technology*, ser. Encyclopedia of Laser Physics and Technology. Wiley, 2008, no. Bd. 1. [Online]. Available: <http://books.google.de/books?id=hdkJ5ASTFjcC>
- [15] A. Bayramian, P. Armstrong, E. Ault, R. Beach, C. Bibeau, J. Caird, R. Campbell, B. Chai, J. Dawson, C. Ebbers, A. Erlandson, Y. Fei, B. Freitas, R. Kent, Z. Liao, T. Ladran, J. Menapace, B. Molander, S. Payne, N. Peterson, M. Randles, K. Schaffers, S. Sutton, J. Tassano, S. Telford, and E. Utterback, "The mercury project: A high average power, gas-cooled laser for inertial fusion energy development," *Fusion Science and Technology*, vol. 52, no. 3, pp. 383–387, 2007.
- [16] J. Hein, M. Kaluza, and R. Bödefeld, "Polaris: An all diode-pumped ultrahigh peak power laser for high repetition rates," *Lasers and Nuclei*, vol. 694, pp. 47–66, 2006. [Online]. Available: http://link.springer.com/chapter/10.1007/3-540-30272-7_4
- [17] M. Hornung, S. Keppler, R. Bödefeld, A. Kessler, H. Liebetrau, J. Körner, M. Hellwing, F. Schorcht, O. Jäckel, A. Sävert, J. Polz, A. K. Arunachalam, J. Hein, and M. C. Kaluza, "High-intensity, high-contrast laser pulses generated from the fully diode-pumped Yb:glass laser system POLARIS." *Optics Letters*, vol. 38, no. 5, pp. 718–20, Mar. 2013. [Online]. Available: <http://www.ncbi.nlm.nih.gov/pubmed/23455276>
- [18] M. Siebold, F. Roeser, M. Loeser, D. Albach, and U. Schramm, "PEneLOPE: a high peak-power diode-pumped laser system for laser-plasma experiments," *Proceedings of SPIE*, vol. 8780, no. 878005, pp. 1–14, May 2013. [Online]. Available: <http://proceedings.spiedigitallibrary.org/proceeding.aspx?doi=10.1117/12.2017522>
- [19] J. Tümmler, R. Jung, H. Stiel, P. V. Nickles, and W. Sandner, "High-repetition-rate chirped-pulse-amplification thin-disk laser system with joule-level pulse energy," *Optics Letters*, vol. 34, no. 9, p. 1378, Apr. 2009. [Online]. Available: <http://ol.osa.org/abstract.cfm?URI=ol-34-9-1378>
- [20] J. Kawanaka, K. Yamakawa, K. Tsubakimoto, T. Kanabe, T. Kawashima, H. Nakano, M. Yoshida, T. Yanagitani, F. Yamamura, M. Fujita, Y. Suzuki, N. Miyanaga, and Y. Izawa, "Generation of ENergetic Beam Ultimate (GENBU) Laser - Main Laser -," *The Review of Laser Engineering*, vol. 36, no. APLS, pp. 1056–1058, 2008. [Online]. Available: <http://joi.jlc.jst.go.jp/JST.JSTAGE/lcj/36.1056?from=CrossRef>
- [21] H. Furuse, J. Kawanaka, N. Miyanaga, H. Chosrowjan, M. Fujita, S. Ishii, K. Imasaki, K. Takeshita, and Y. Izawa, "Conceptual design for sub-100 kW laser system based on total-reflection active-mirror geometry," in *Advances in Optical Materials*. Washington, D.C.: OSA, Feb. 2011, p. AWA06. [Online]. Available: <http://www.opticsinfobase.org/abstract.cfm?URI=ASSP-2011-AWA06>
- [22] T. Gonçalves-Novo, D. Albach, B. Vincent, M. Arzakantsyan, and J.-C. Chanteloup, "14 J/2 Hz Yb³⁺:YAG diode pumped solid state laser chain." *Optics Express*, vol. 21, no. 1, pp. 855–66, Jan. 2013. [Online]. Available: <http://www.ncbi.nlm.nih.gov/pubmed/23388979>

- [23] S. Banerjee, K. Ertel, P. D. Mason, P. J. Phillips, M. Siebold, M. Loeser, C. Hernandez-Gomez, and J. L. Collier, "High-efficiency 10 J diode pumped cryogenic gas cooled Yb:YAG multislabs amplifier." *Optics letters*, vol. 37, no. 12, pp. 2175–7, Jun. 2012. [Online]. Available: <http://www.ncbi.nlm.nih.gov/pubmed/22739846>
- [24] S. Banerjee, K. Ertel, P. Mason, J. Phillips, J. Greenhalgh, and J. Collier, "DiPOLE: A multi-slab cryogenic diode pumped Yb:YAG amplifier," *Proceedings of SPIE*, vol. 8780, no. 878006, pp. 1–7, May 2013. [Online]. Available: <http://proceedings.spiedigitallibrary.org/proceeding.aspx?doi=10.1117/12.2016611>
- [25] A. E. Siegman, *Lasers*. University Science Books, 1986. [Online]. Available: <http://books.google.de/books?id=1BZVwUZLTkAC>
- [26] O. Svelto, *Principles of Lasers*, 5th ed. Springer, 2010, vol. 22, no. 1. [Online]. Available: <http://www.springerlink.com/index/10.1007/978-1-4419-1302-9>
- [27] F. Träger, *Handbook of Lasers and Optics*, ser. Springer handbooks. Springer Science+Business Media, 2007. [Online]. Available: <http://books.google.ca/books?id=YOHJGz-9UNoC>
- [28] W. Koechner, *Solid-State Laser Engineering*, 6th ed. Springer, 2009, vol. 1. [Online]. Available: <http://books.google.com/books?id=RK3jK0XWjdMC>
- [29] R. Trebino, *Frequency-Resolved Optical Gating: The Measurement of Ultrashort Laser Pulses*. Kluwer Academic Publishers, 2000. [Online]. Available: <http://books.google.de/books?id=yfLlg6E69D8C>
- [30] H. J. Eichler and J. Eichler, *Laser: Bauformen, Strahlführung, Anwendungen*. Springer, 2006. [Online]. Available: <http://books.google.de/books?id=wFErEnp4x4AC>
- [31] A. Einstein, *Zur Quantentheorie der Strahlung*. Hirzel, 1917, vol. 18.
- [32] T. H. Maiman, "Stimulated Optical Radiation in Ruby," *Nature*, vol. 187, no. 4736, pp. 493–494, 1960. [Online]. Available: <http://www.nature.com/nature/journal/v187/n4736/abs/187493a0.html>
- [33] L. M. Frantz and J. S. Nodvik, "Theory of Pulse Propagation in a Laser Amplifier," *Journal of Applied Physics*, vol. 34, no. 8, p. 2346, 1963. [Online]. Available: <http://link.aip.org/link/JAPIAU/v34/i8/p2346/s1&Agg=doi>
- [34] N. P. Barnes and B. M. Walsh, "Amplified Spontaneous Emission-Application to Nd:YAG lasers," *IEEE Journal of Quantum Electronics*, vol. 35, no. 1, pp. 101–109, 1999. [Online]. Available: <http://ieeexplore.ieee.org/lpdocs/epic03/wrapper.htm?arnumber=737626>
- [35] J. B. Trenholme, "Fluorescence Amplification and Parasitic Oscillation Limitations in Disc Lasers," *Naval Research Laboratory Memorandum Rep. 2480*, 1972.
- [36] W. Krupke, "Ytterbium solid-state lasers - The first decade," *IEEE Journal on Selected Topics in Quantum Electronics*, vol. 6, no. 6, pp. 1287–1296, 2000. [Online]. Available: http://ieeexplore.ieee.org/xpls/abs_all.jsp?arnumber=902180
- [37] M. Siebold, J. Hein, M. Hornung, S. Podleska, M. Kaluza, S. Bock, and R. Sauerbrey, "Diode-pumped lasers for ultra-high peak power," *Applied Physics B*, vol. 90, no. 3–4, pp. 431–437, Jan. 2008. [Online]. Available: <http://link.springer.com/10.1007/s00340-007-2907-0>
- [38] J. Körner, J. Hein, M. Kahle, H. Liebetrau, M. Lenski, M. Kaluza, M. Loeser, and M. Siebold, "Temperature dependent measurement of absorption and emission cross sections for various Yb³⁺ doped laser materials," *Proc. SPIE 8080*, pp. 808 003–808 007, 2011. [Online]. Available: <http://dx.doi.org/10.1117/12.887410>

- [39] J. Koerner, C. Vorholt, H. Liebetrau, M. Kahle, D. Kloepfel, R. Seifert, J. Hein, and M. C. Kaluza, "Measurement of temperature-dependent absorption and emission spectra of Yb:YAG, Yb:LuAG, and Yb:CaF₂ between 20 °C and 200 °C and predictions on their influence on laser performance," *Journal of the Optical Society of America B*, vol. 29, no. 9, p. 2493, Aug. 2012. [Online]. Available: <http://josab.osa.org/abstract.cfm?URI=josab-29-9-2493>
- [40] J. Körner, V. Jambunathan, J. Hein, R. Seifert, M. Loeser, M. Siebold, U. Schramm, P. Sikocinski, A. Lucianetti, T. Mocek, and M. C. Kaluza, "Spectroscopic characterization of Yb³⁺-doped laser materials at cryogenic temperatures," *Applied Physics B*, Sep. 2013. [Online]. Available: <http://link.springer.com/10.1007/s00340-013-5650-8>
- [41] C. Danson, P. Brummitt, R. Clarke, J. Collier, B. Fell, A. Frackiewicz, S. Hancock, S. Hawkes, C. Hernandez-Gomez, P. Holligan, M. Hutchinson, A. Kidd, W. Lester, I. Musgrave, D. Neely, D. Neville, P. Norreys, D. Pepler, C. Reason, W. Shaikh, T. Winstone, R. Wyatt, and B. Wyborn, "Vulcan Petawatt - an ultra-high-intensity interaction facility," *Nuclear Fusion*, vol. 44, no. 12, pp. S239–S246, Dec. 2004. [Online]. Available: <http://stacks.iop.org/0029-5515/44/i=12/a=S15?key=crossref.ad7333baa871b101225abbd34d72c73>
- [42] E. W. Gaul, M. Martinez, J. Blakeney, A. Jochmann, M. Ringuette, D. Hammond, T. Borger, R. Escamilla, S. Douglas, W. Henderson, G. Dyer, A. Erlandson, R. Cross, J. Caird, C. Ebbers, and T. Ditmire, "Demonstration of a 1.1 petawatt laser based on a hybrid optical parametric chirped pulse amplification mixed Nd:glass amplifier." *Applied optics*, vol. 49, no. 9, pp. 1676–81, Mar. 2010. [Online]. Available: <http://www.ncbi.nlm.nih.gov/pubmed/20300167>
- [43] D. S. Sumida and T. Y. Fan, "Effect of radiation trapping on fluorescence lifetime and emission cross section measurements in solid-state laser media," *Optics Letters*, vol. 19, no. 17, p. 1343, Sep. 1994. [Online]. Available: <http://ol.osa.org/abstract.cfm?URI=ol-19-17-1343>
- [44] J. Dong, M. Bass, Y. Mao, P. Deng, and F. Gan, "Dependence of the Yb³⁺ emission cross section and lifetime on temperature and concentration in yttrium aluminum garnet," *Journal of the Optical Society of America B*, vol. 20, no. 9, p. 1975, Sep. 2003. [Online]. Available: <http://josab.osa.org/abstract.cfm?URI=josab-20-9-1975>
- [45] D. Albach, "Amplified Spontaneous Emission and Thermal Management on a High Average-Power Diode-Pumped Solid-State Laser The Lucia Laser System," Dissertation, École Polytechnique Paris Palaiseau, 2010.
- [46] U. Morgner, F. X. Kärtner, S. H. Cho, Y. Chen, H. A. Haus, J. G. Fujimoto, E. P. Ippen, V. Scheuer, G. Angelow, and T. Tschudi, "Sub-two-cycle pulses from a Kerr-lens mode-locked Ti:sapphire laser," *Optics Letters*, vol. 24, no. 6, p. 411, Mar. 1999. [Online]. Available: <http://ol.osa.org/abstract.cfm?URI=ol-24-6-411>
- [47] S. Karsch, *Lecture notes: "Generation of high-intensity laser pulses"*, 2010.
- [48] E. Treacy, "Optical Pulse Compression With Diffraction Gratings," *IEEE Journal of Quantum Electronics*, vol. 5, no. 9, pp. 454–458, 1969. [Online]. Available: <http://ieeexplore.ieee.org/lpdocs/epic03/wrapper.htm?arnumber=1076303>
- [49] O. E. Martinez, "3000 Times Grating Compressor with Positive Group Velocity Dispersion," *IEEE Journal of Quantum Electronics*, vol. 23, no. 1, pp. 59–64, 1987. [Online]. Available: <http://ieeexplore.ieee.org/stamp/stamp.jsp?tp=&arnumber=1073201&isnumber=23099>
- [50] P. Tournois, "Compensation of group delay time dispersion in laser systems," *Optics Communications*, vol. 140, no. 4–6, pp. 245–249, 1997.

- [51] D. Albach, J.-C. Chanteloup, and G. L. Touzé, "Influence of ASE on the gain distribution in large size, high gain Yb³⁺:YAG slabs." *Optics Express*, vol. 17, no. 5, pp. 3792–801, Mar. 2009. [Online]. Available: <http://www.ncbi.nlm.nih.gov/pubmed/19259221>
- [52] M. Siebold, M. Loeser, J. Koerner, M. Wolf, J. Hein, C. Wandt, S. Klingebiel, S. Karsch, and U. Schramm, "Efficiency, Energy, and Power Scaling of Diode-Pumped, Short-Pulse Laser Amplifiers Using Yb-Doped Gain Media," in *Lasers, Sources and Related Photonic Devices*. Washington, D.C.: OSA, Jan. 2010, p. AWB19. [Online]. Available: <http://www.opticsinfobase.org/abstract.cfm?URI=ASSP-2010-AWB19>
- [53] K. Ertel, S. Banerjee, P. D. Mason, P. J. Phillips, M. Siebold, J. C. Collier, and B. Landstr, "Optimising the efficiency of pulsed diode pumped Yb : YAG laser amplifiers for ns pulse generation." vol. 19, no. 27, pp. 26 610–26 626, 2011.
- [54] M. Sawicka, M. Divoky, J. Novak, A. Lucianetti, B. Rus, and T. Mocek, "Modeling of amplified spontaneous emission, heat deposition, and energy extraction in cryogenically cooled multislabs Yb³⁺:YAG laser amplifier for the HiLASE Project," *Journal of the Optical Society of America B*, vol. 29, no. 6, p. 1270, May 2012. [Online]. Available: <http://www.opticsinfobase.org/abstract.cfm?URI=josab-29-6-1270>
- [55] I. Ahmad, "Development of an optically synchronized seed source for a high-power few-cycle OPCPA system," Dissertation, LMU München, 2011. [Online]. Available: http://edoc.ub.uni-muenchen.de/13250/1/Ahmad_Izhar.pdf
- [56] I. Ahmad, S. A. Trushin, Z. Major, C. Wandt, S. Klingebiel, T.-J. Wang, V. Pervak, A. Popp, M. Siebold, F. Krausz, and S. Karsch, "Frontend light source for short-pulse pumped OPCPA system," *Applied Physics B*, vol. 97, no. 3, pp. 529–536, Jun. 2009. [Online]. Available: <http://link.springer.com/10.1007/s00340-009-3599-4>
- [57] C. Skrobol, I. Ahmad, S. Klingebiel, C. Wandt, S. A. Trushin, Z. Major, F. Krausz, and S. Karsch, "Broadband amplification by picosecond OPCPA in DKDP pumped at 515 nm," *Optics Express*, vol. 20, no. 4, pp. 4619–29, Feb. 2012. [Online]. Available: <http://www.ncbi.nlm.nih.gov/pubmed/22418219>
- [58] C. Y. Teisset, N. Ishii, T. Fujii, T. Metzger, S. Köhler, R. Holzwarth, A. Baltuska, A. M. Zheltikov, and F. Krausz, "Soliton-based pump-seed synchronization for few-cycle OPCPA," *Optics Express*, vol. 13, no. 17, p. 6550, Aug. 2005. [Online]. Available: <http://www.opticsexpress.org/abstract.cfm?URI=oe-13-17-6550>
- [59] I. Ahmad, "Development of an optically synchronized seed source for a high-power few-cycle OPCPA system," Dissertation, LMU München, 2011, ch. 2.2, pp. 14–28. [Online]. Available: http://edoc.ub.uni-muenchen.de/13250/1/Ahmad_Izhar.pdf
- [60] S. Klingebiel, "Picosecond pump dispersion management and jitter stabilization in a petawatt-scale few-cycle OPCPA system," Dissertation, LMU München, 2013, ch. 4.3, pp. 41–50.
- [61] S. Klingebiel, I. Ahmad, C. Wandt, C. Skrobol, S. A. Trushin, Z. Major, F. Krausz, and S. Karsch, "Experimental and theoretical investigation of timing jitter inside a stretcher-compressor setup," *Optics Express*, vol. 20, no. 4, p. 3443, Jan. 2012. [Online]. Available: <http://www.opticsexpress.org/abstract.cfm?URI=oe-20-4-3443>
- [62] C. Wandt, S. Klingebiel, M. Siebold, Z. Major, J. Hein, F. Krausz, and S. Karsch, "Generation of 220 mJ nanosecond pulses at a 10 Hz repetition rate with excellent beam quality in a diode-pumped Yb:YAG MOPA system," *Optics Letters*, vol. 33, no. 10, p. 1111, May 2008. [Online]. Available: <http://ol.osa.org/abstract.cfm?URI=ol-33-10-1111>
- [63] R. Trebino and K. DeLong, "Measuring ultrashort laser pulses in the time-frequency domain using frequency-resolved optical gating," *Review of Scientific Instruments*, vol. 68, no. 9, pp. 3277–3295, 1997. [Online]. Available: http://ieeexplore.ieee.org/xpls/abs_all.jsp?arnumber=4995341

- [64] M. Siebold, C. Wandt, S. Karsch, F. Krausz, J. Hein, D. Wolff, G. Bonati, and S.-S. Beyertt, "High brightness laser diode array at 940 nm for Yb:YAG pumping," in *CLEO/Europe and IQEC 2007 Conference Digest*. Optical Society of America, Jun. 2007, p. CB_24. [Online]. Available: http://www.opticsinfobase.org/abstract.cfm?URI=CLEO_Europe-2007-CB_24
- [65] M. Siebold, J. Hein, C. Wandt, S. Klingebiel, F. Krausz, and S. Karsch, "High-energy, diode-pumped, nanosecond Yb:YAG MOPA system," *Optics Express*, vol. 16, no. 6, p. 3674, Mar. 2008. [Online]. Available: <http://www.opticsexpress.org/abstract.cfm?URI=oe-16-6-3674>
- [66] R. Voelkel and K. J. Weible, "Laser Beam Homogenizing: Limitations and Constraints," *Proc. SPIE 7102, Optical Fabrication, Testing and Metrology III*, p. 71020J, 2008. [Online]. Available: <http://dx.doi.org/10.1117/12.799400>
- [67] A. Giesen and J. Speiser, "Fifteen Years of Work on Thin-Disk Lasers: Results and Scaling Laws," *IEEE Journal of Selected Topics in Quantum Electronics*, vol. 13, no. 3, pp. 598–609, 2007. [Online]. Available: <http://ieeexplore.ieee.org/lpdocs/epic03/wrapper.htm?arnumber=4244423>
- [68] H. Yagi, J. Bisson, K. Ueda, and T. Yanagitani, "Y3Al5O12 ceramic absorbers for the suppression of parasitic oscillation in high-power Nd:YAG lasers," *Journal of Luminescence*, vol. 121, no. 1, pp. 88–94, Nov. 2006. [Online]. Available: <http://linkinghub.elsevier.com/retrieve/pii/S0022231305002504>
- [69] LambdaSpect, "LambdaSpect." [Online]. Available: <http://www.lambdaspect.com/>
- [70] Autodesk Inventor, "Autodesk Inventor." [Online]. Available: <http://www.autodesk.com/products/autodesk-inventor-family/overview>
- [71] R. Wynne, J. L. Daneu, and T. Y. Fan, "Thermal coefficients of the expansion and refractive index in YAG." *Applied optics*, vol. 38, no. 15, pp. 3282–4, May 1999. [Online]. Available: <http://www.ncbi.nlm.nih.gov/pubmed/18319922>
- [72] H. Qiu, P. Yang, J. Dong, P. Deng, J. Xu, and W. Chen, "The influence of Yb concentration on laser crystal Yb:YAG," *Materials Letters*, vol. 55, no. 1-2, pp. 1–7, Jul. 2002. [Online]. Available: <http://www.sciencedirect.com/science/article/pii/S0167577X01006085>
- [73] X. Xu, Z. Zhao, J. Xu, and P. Deng, "Thermal diffusivity, conductivity and expansion of Yb3xY3(1-x)Al5O12 (x=0.05, 0.1 and 0.25) single crystals," *Solid State Communications*, vol. 130, no. 8, pp. 529–532, May 2004. [Online]. Available: <http://linkinghub.elsevier.com/retrieve/pii/S0038109804001784>
- [74] M. Bass, *Handbook of Optics - II*, ser. Handbook of Optics. McGraw-Hill Professional Publishing, 1994.
- [75] N. Pavel, K. Lünstedt, K. Petermann, and G. Huber, "Multipass pumped Nd-based thin-disk lasers: continuous-wave laser operation at 1.06 and 0.9 microm with intracavity frequency doubling." *Applied optics*, vol. 46, no. 34, pp. 8256–63, Dec. 2007. [Online]. Available: <http://www.ncbi.nlm.nih.gov/pubmed/18059665>
- [76] S. Forget, F. Balembois, P. Georges, and P.-J. Devilder, "A new 3D multipass amplifier based on Nd:YAG or Nd:YVO 4 crystals," *Applied Physics B: Lasers and Optics*, vol. 75, no. 4-5, pp. 481–485, Oct. 2002. [Online]. Available: <http://link.springer.com/10.1007/s00340-002-0997-2>
- [77] K. Contag, "Modellierung und numerische Auslegung des Yb: YAG-Scheibenlasers," Ph.D. dissertation, 2002.

- [78] K. Ertel, C. Hooker, S. J. Hawkes, B. T. Parry, and J. L. Collier, "ASE suppression in a high energy Titanium sapphire amplifier." *Optics express*, vol. 16, no. 11, pp. 8039–49, May 2008. [Online]. Available: <http://www.ncbi.nlm.nih.gov/pubmed/18545514>
- [79] G. J. Linfood, E. R. Peressini, W. R. Sooy, and M. L. Spaeth, "Very long lasers," *Applied Optics*, vol. 13, no. 2, pp. 379–90, Feb. 1974. [Online]. Available: <http://www.ncbi.nlm.nih.gov/pubmed/20125990>
- [80] C. Wandt, S. Klingebiel, S. Keppler, M. Hornung, C. Skrobol, A. Kessel, S. A. Trushin, Z. Major, J. Hein, M. C. Kaluza, F. Krausz, and S. Karsch, "Development of a Joule-class Yb:YAG amplifier and its implementation in a CPA system generating 1 TW pulses," *Laser & Photonics Reviews*, pp. n/a–n/a, Jun. 2014. [Online]. Available: <http://doi.wiley.com/10.1002/lpor.201400040>
- [81] "Laboratory for Extreme Photonics." [Online]. Available: <http://www.lex-photonics.de/>
- [82] "Extreme Light Infrastructure." [Online]. Available: <http://www.eli-laser.eu/>

Parts of this thesis have been published in:

1. **Chr. Wandt**, S. Klingebiel, S. Keppler, M. Hornung, C. Skrobol, A. Kessel, S. A. Trushin, Zs. Major, J. Hein, M. C. Kaluza, F. Krausz, and S. Karsch: “*Development of a Joule-class Yb:YAG amplifier and its implementation in a CPA system generating 1 TW pulses*”; Laser & Photonics Reviews, pp. n/a - n/a, Jun. 2014, Online: <http://doi.wiley.com/10.1002/lpor.201400040>

Further publications by the author:

1. **Chr. Wandt**, S. Klingebiel, M. Siebold, Zs. Major, J. Hein, F. Krausz, and S. Karsch: “*Generation of 220 mJ nanosecond pulses at a 10 Hz repetition rate with excellent beam quality in a diode-pumped Yb:YAG MOPA system*”; Optics Letters, Vol. 33, Issue 10, pp. 1111-1113, 2008; Online: <http://dx.doi.org/10.1364/OL.33.001111>
2. M. Siebold, J. Hein, **Chr. Wandt**, S. Klingebiel, F. Krausz, and S. Karsch: “*High-energy, diode-pumped, nanosecond Yb:YAG MOPA system*”; Optics Express, Vol. 16, Issue 6, pp. 3674-3679, 2008; Online: <http://dx.doi.org/10.1364/OE.16.003674>
3. M. Siebold, M. Hornung, R. Boedefeld, S. Podleska, S. Klingebiel, **Chr. Wandt**, F. Krausz, S. Karsch, R. Uecker, A. Jochmann, J. Hein, and M. C. Kaluza: “*Terawatt diode-pumped Yb:CaF₂ laser*”; Optics Letters, Vol. 33, Issue 23, pp. 2770-2772, 2008; Online: <http://dx.doi.org/10.1364/OL.33.002770>
4. Zs. Major, S.A. Trushin, I. Ahmad, M. Siebold, **Chr. Wandt**, S. Klingebiel, T.-J. Wang, J. A. Fülöp, A. Henig, S. Kruber, R. Weingartner, A. Popp, J. Osterhoff, R. Hörlein, J. Hein, V. Pervak, A. Apolonski, F. Krausz and S. Karsch: “*Basic concepts and current status of the Petawatt Field Synthesizer - a new approach to ultrahigh field generation*”; Rev. Laser Eng., Vol. 37, pp. 431-436, 2009
5. I. Ahmad, S.A. Trushin, Zs. Major, **Chr. Wandt**, S. Klingebiel, T.-J. Wang, V. Pervak, A. Popp, M. Siebold, F. Krausz, and S. Karsch: “*Frontend light source for short-pulse pumped OPCPA system*”; Applied Physics B, Vol. 97, Issue 3, pp. 529-536, 2009; Online: <http://dx.doi.org/10.1007/s00340-009-3599-4>
6. S. Klingebiel, **Chr. Wandt**, C. Skrobol, I. Ahmad, S.A. Trushin, Zs. Major, F. Krausz, and S. Karsch: “*High energy picosecond Yb:YAG CPA system at 10 Hz repetition rate for pumping optical parametric amplifiers*”; Optics Express, Vol. 19, Issue 6, pp. 5357-5363, 2011; Online: <http://dx.doi.org/10.1364/OE.19.005357>
7. S. Klingebiel, I. Ahmad, **Chr. Wandt**, C. Skrobol, S.A. Trushin, Zs. Major, F. Krausz, and S. Karsch: “*Experimental and theoretical investigation of timing jitter inside a stretcher-compressor setup*”; Optics Express, Vol. 20, Issue 4, pp. 3443-3455, 2012; Online: <http://dx.doi.org/10.1364/OE.20.003443>
8. C. Skrobol, I. Ahmad, S. Klingebiel, **Chr. Wandt**, S.A. Trushin, Zs. Major, F. Krausz, and S. Karsch: “*Broadband amplification by picosecond OPCPA in DKDP pumped at 515 nm*”; Optics Express, Vol. 20, Issue 4, pp. 4619-4629, 2012; Online: <http://dx.doi.org/10.1364/OE.20.004619>

ACKNOWLEDGMENTS

"An expert is a person who has made all the mistakes that can be made in a very narrow field."

Niels Bohr

... and i did quite a bunch of them during this thesis work. So, i would like to thank those who let me gain all these experiences and moreover who helped me to learn from my mistakes!

First of all, i would like to express my sincere gratitude to my supervisor Prof. Dr. Stefan Karsch - for the trust in me, the guidance and advice and the patience with me through all the years.

Likewise, i would like to thank Prof. Dr. Ferenc Krausz for giving me the possibility to work and study in the formidable scientific environment of the Laboratory for Attosecond Physics (LAP).

Special thanks to Prof. Dr. Ulrich Schramm for reviewing this thesis and providing the expertise.

Many, many thanks to all current and former members of the LAP who helped me in one way or the other. Especially, my colleagues of the Karsch-group: Sandro Klingebiel, Christoph Skrobol, Alexander Kessel, Sergei A. Trushin, Zsuzsanna Major - Matthias Heigoldt, Johannes Wenz, Konstantin Khrennikov. Thank you for your support, ideas, discussions and the fun times besides the usual work...

Special thanks also to all technicians of the LAP and the MPQ workshop for your assistance and contributions integral to get everything running in the lab.

Furthermore, i would like to thank the IMPRS-APS - all members, coordinators and Frau Wild - for their support and the remarkable meetings at Schloss Ringberg.

I also owe the members of the HEC-DPSSL community a big "Thank you!" for sharing expertise and knowledge. Especially, Joachim Hein, Marco Hornung and Sebastian Keppler and all other colleagues and friends of the POLARIS-group in Jena for always open ears and minds. Without your feedback and ideas the realization of "the tube" would have been a much harder task. Many thanks as well to Mathias Siebold, Daniel Albach and Marcus Löser of the HZDR and Thomas Töpfer and his team at Lastronics.

Last but not least - my deepest gratitude goes to my family and friends! Without your ceaseless and unreserved backing nothing of this would have been possible!

DATA ARCHIVING

All experimental raw data, the corresponding evaluation files and the resulting figures as well as the used simulation files can be found on the data-archive server of the Laboratory for Attosecond Physics at the Max-Planck-Institute of Quantum Optics. The file paths are arranged according to the structuring of the thesis: In folders for each chapter, the data is organized in sub-folders, named as the corresponding figure or table. Each of these folders contains the final figure file, the corresponding evaluation/simulation file and the experimental raw data. A *description.txt* is added explaining the data and all steps necessary to reproduce the figure.

Colophon

This document was typeset using `classicthesis` developed by André Miede.

Further adaptations were included by the author.

`classicthesis` is available for both \LaTeX and \LyX :

<http://code.google.com/p/classicthesis/>

Final Version as of July 24, 2014 (`classicthesis` version 4.0).